Dissertation

submitted to the

Combined Faculty of Natural Sciences and

Mathematics

of the Ruperto Carola University Heidelberg, Germany

for the degree of

Doctor of Natural Sciences

Presented by
Sergio Lembo, M.Sc. in Molecular biology of the cell

born in: Ragusa, Italy
Oral examination: 24th of February 2021.

Shedding light on Membrane-to-cortex attachment through the development of molecular tools

Referees: Dr. Peter Lenart

Prof. Dr. Frauke Gräter

This work has been carried out at the European Molecular Biology Laboratory under the supervision of Dr. Alba Diz-Muñoz from September 2016 to October 2020.

Zusammenfassung

Die mechanischen Eigenschaften der Zelloberfläche sind Hauptregulatoren verschiedener Zellprozesse, von Formbestimmung über Migration, bis zum Erwerb des Schicksals der Zelle. Die Oberfläche von Tierzellen besteht aus der Plasmamembran, dem Actomyosinzellkortex, und dem Membrane-to-Cortex Attachment (MCA), welches definiert ist als die Anbindung der Plasmamembran an den darunterliegenden Zellkortex durch Proteine. Es ist bekannt, dass MCA an der Zelloberflächenmechanik beteiligt ist und zur Regulierung verschiedener biologischer Prozesse an der Zelloberfläche beiträgt. MCA ist jedoch auch das am schwersten zu fassende Element der tierischen Zelloberfläche und die meisten seiner Eigenschaften und Funktionen sind noch unklar. Der Mangel an geeigneten Methoden um MCA in der Zelle zu perturbieren insbesondere ist der Hauptgrund für diese Wissenslücke.

In dieser Dissertation werde ich meine PhD-Arbeit an MCA beschreiben. Im ersten Teil meines PhDs entwickelte und testete ich ein molekulares Werkzeug namens iMC linker, welches es erlaubt, MCA in zellulären Modellsystemen spezifisch zu erhöhen. Mittels des iMC linker untersuchten wir MCA von sowohl einem biologischen als auch einem biophysischen

Gesichtspunkt aus. Zuerst konzentrierten wir uns auf die Zelldifferenzierung, von der wir bereits wissen dass sie über die mechanischen Eigenschaften der extrazellulären Matrix und der Zelloberfläche reguliert wird. Mithilfe von Stammzellen des Mausembryos als Modellsystem entdeckten wir dass Zellen MCA reduzieren müssen um sich differenzieren zu können. Wenn diese Reduktion durch iMC linker verhindert wird, so sind die Zellen in einem Zustand der Pluripotenz gefangen. Somit fanden wir eine neuartige Rolle für MCA in der Regulierung vom Erwerb des Zellschicksals.

Im letzten Teil meiner Dissertation beschreibe ich unsere Versuche, den biophysischen Beitrag von MCA zu den mechanischen Eigenschaften der Zelloberfläche zu entziffern. Interessanterweise fanden wir heraus, dass MCA die Mechaniken des Zellkortexes reguliert. Insbesondere ist ein iMC-linker-bedingter Anstieg in MCA an eine Reduktion der Steifheit des Zellkortex und der Spannung des Kortex gekoppelt. Die Implikationen dieser Ergebnisse können für Kortexmechaniken die durch verschiedene Zellprozesse reguliert werden, so wie Zytokinese und Zellschicksal, relevant sein.

Summary

The mechanical properties of the cell surface are master regulators of various cell processes, ranging from shape determination, to migration, to fate acquisition. The surface of animal cells consists of the plasma membrane, the actomyosin cell cortex, and Membrane-to-Cortex Attachment (MCA), defined as the protein-mediated tethering of the plasma membrane to the cell cortex beneath. MCA has been shown to contribute to cell surface mechanics and to be involved in the regulation of different biological processes at the cell surface. However, MCA remains the most elusive element of the animal cell surface and there is a clear gap in our understanding of its roles and regulation. This is mainly due to the lack of proper methods to specifically perturb MCA in cells.

In this thesis, I am going to describe my PhD work on MCA. In the first part of my PhD, I engineered and validated a molecular tool, named iMC linker, which allows to increase specifically MCA in cellular model systems. Next, With iMC linker at hand, we studied MCA from both a biological and a biophysical viewpoint. First, we focused on cell differentiation, a process already shown to be regulated by mechanical properties of the extracellular matrix and the cell surface. Using mouse embryonic stem cells as a model system, we found that

cells need to reduce their MCA in order to differentiate. Preventing this reduction by expressing iMC linker, locks the cells in a state of naïve pluripotency. Therefore, we uncovered a novel role for MCA in regulating cell differentiation.

Second, I will describe our current efforts in deciphering the biophysical contribution of MCA to the mechanical properties of the cell surface. Strikingly, we found that MCA regulates cell cortex mechanics. Specifically, an iMC linker-mediated increase in MCA is coupled with a reduction in cell cortex stiffness and cortical tension. The implication of these findings may be relevant for various cellular processes regulated by cortex mechanics, such as cytokinesis and cell fate acquisition.

List of Contents

List of figures

List of Tables

List of Abbreviations

Abbreviation	Meaning
ABD	Actin-binding domain
AFS	Atomic force spectroscopy
CAezrin	Constitutively active Ezrin
DNezrin	Dominant negative Ezrin
Dox	Doxycycline
E	Apparent Young's modulus
ERM	ERM protein family
MCA	Membrane-to-cortex attachment
mESC	Mouse embryonic stem cell
PIP2	Phosphatidylinositol 4,5-bisphosphate
PM	Plasma membrane
Utr	Utrophin

Acknowledgements

The past 4 years have been extremely challenging, and I would have not achieved this important life and career goal without the help and support of various persons. First of all, I want to thank Alba Diz-Muñoz, my Ph.D. advisor. She has been a great mentor and I have learned a lot from her. Being her first Ph.D. student, I have seen Alba growing professionally and scientifically: she has become an amazing group leader, manager and scientist; I am very proud of her. She has been very patient and has always supported me on a scientific and personal level. She has been on my side during hard times and at the same time she let me free to learn and grow at my own pace. I would have never managed to complete my Ph.D. without an advisor of her caliber.

I want to thank all the members of my lab, in particular Martin Bergert for all he taught me in the past four years, and Leanne Strauss for being a great collaborator. I am grateful also to my amazing students, Simon Wergert and Danica Milovanovic. They did a great job and I hope I have been a good mentor to them.

I want to thank my TAC members Prof. Dr. Frauke Gräter, Dr. Peter Lenart and Dr. Martin Beck. Their advice during the TAC meetings was extremely

valuable. In particular, I am very grateful to Dr. Lenart and Prof. Gräter for reviewing this thesis. Moreover, I will always be grateful to Dr. Lenart (and of course, Alba) for supporting my enrollment in the Physiology course, one the most amazing experiences of my scientific and personal life. I also want to thank Prof. Guillaume Charras, my “unofficial” TAC member. His scientific advice was very precise and let me avoid different dead ends for my project.

My Ph.D. has extremely interdisciplinary (again, thanks to Alba), and I need to thank all the collaborators who made my work much more exciting. In particular, I thank Martin Bergert, Mauricio Toro-Nahuelpan, Julia Mahamid, Joseph Vermil, Mattieu Piel, Chii Jou Chan, Deb Sankar Banerjee, Shiladitya Banerjee, Manuel Erugen and Jan Ellenberg.

From a personal viewpoint. I want to thank Luigi Russo, for being a very good friend and helping me out during different crisis I had. I want to thank my parents and my sister, even though I did not shared with them much about my Ph.D.; I know they love me and so do I. Most importantly, I want to thank my girlfriend Ksenia Kirillova. She found me in the darkest period of my Ph.D. and in the past 2 years she has been my beacon: I think I would be lost now if I had not met her. She is extremely smart and taught me a lot, also about myself. Besides, she has been (together with Alba) the proofreader of my thesis.

Finally, I need to thank another someone, somebody I never thank and for whom I rarely show appreciation. I never trusted this person, and I did not believe in him. Nevertheless, all my achievements depend on him and his perseverance. Thank you, Sergio.

1. Introduction

The characterization of the DNA structure started the era of molecular biology in which biochemistry and genetics have been recognized as the master regulators of the behavior of cells and supracellular structures. However, in the past three decades, it became clear that biophysical aspects cannot be underestimated: physical properties of cells and their environments are as crucial as biochemical cues in determining biological structures (Pelling & Horton, 2008). Furthermore, cells are able to exploit and regulate these properties to exert specific functions. In this context, cell mechanics have been shown to be pivotal in a wide plethora of biological phenomena, ranging from cellular motility, to fate determination, to organogenesis (reviewed in (Lecuit & Lenne, 2007) (Moeendarbary & Harris, 2014) (Diz-Muñoz et al., 2018)).

Mechanobiology has emerged as a leading field in cell biology, and the cell surface has become its main target of study, owing to its accessibility for physical measurements, and its role in cell homeostasis, activity and physiopathology (Ingber, 2018). The surface of animal cells, can be roughly subdivided in three layers: the Plasma Membrane (PM), the lipid bilayer with embedded proteins which surrounds the cell and separates the intracellular from the extracellular environment; the cell cortex, a thin meshwork of Actin and Actin

associated proteins found beneath the PM; and Membrane-to-Cortex Attachment (MCA), the physical connection between the former two. The mechanical properties of these layers determine the mechanics of the animal cell surface and are involved in the regulation of, among others, cell shape, cell motility, cell division and vesicular trafficking at the surface (reviewed in (Pontes et al., 2017) (Eggert et al., 2006)).

Our understanding of cell mechanics is growing quickly thanks to extensive investigations on the most critical mechanical properties of the PM and the cortex, namely viscoelasticity and tension. However, a full understanding is far to be achieved owing to methodological limitations and the physical complexity of biological materials. Noteworthy, MCA remains to be the most elusive component despite being postulated to affect different phenomena at the animal cell surface (M. P. Sheetz, 2001).

This thesis aims to portray my Ph.D. work on MCA, which can be roughly articulated in three main parts. The first one consisted in the development of an artificial molecular tool to perturb effectively and specifically MCA. The other two parts relied on the use of this molecular tool with two goals: (i) to foreground the biological importance of MCA in regulating key cellular functions, and (ii) to unravel the biophysics of MCA especially in the context of other structures and mechanical properties of cell surface. More specifically, the second part of my work unveiled a novel role for cell surface mechanics in gating stem cell differentiation. The main finding of the third part is an unforeseen striking role for MCA in regulating cortex mechanics.

1.1. The animal cell surface

The universally accepted theory of the cell states that cells are the fundamental unit of life (Baluška et al., 2004) (Ribatti, 2018). Within this framework, the cell surface can be defined as the minimal physicochemical boundary between living and non-living matter. Ergo, the cell surface is arguably of paramount importance to cell biology: it determines a large number of properties of the cell and contributes to the regulation of several biological functions, including the communication with the external environment.

The complexity of the cell surface can be unraveled using a reductionistic approach. In animal cells, the biological target of my work, the surface is conventionally subdivided into three layers: the plasma membrane, the cell cortex and Membrane-to-Cortex Attachment (MCA). The following sections aim to dissect our current understanding of these structures. Particular emphasis will be given to their mechanics, being the main concern of this thesis.

1.1.1. The plasma membrane

The Plasma Membrane (PM) constitutes the outermost layer of the animal cell surface. The most archetypal – and yet oversimplified – definition, describes the PM as a continuous lipid bilayer with embedded proteins and glycoproteins (Alberts et al., 2015).

Lipids are complex biological macromolecules broadly defined by water insolubility owing to their non-polar nature (Alberts et al., 2015). Phospholipids are the most abundant class of lipids in membranes. They are composed of an alcohol bound to 1-2 hydrophobic acyl chains (the tail) and of a polar modified phosphate group (head). According to the alcoholic core type, phospholipids are subdivided into phosphoglycerides, which contain a molecule of glycerol, and sphingolipids, which contain sphingosine. Phospholipids are also defined by the

type of modification of the phosphate group and by the length and saturation degree of the acyl tails. Sterols constitute the second most abundant class of membrane lipids. Despite being technically alcohols and despite the lack of acyl chains, sterols are classified as lipids owing to their amphipathic structure and biochemical behavior. Notably, cholesterol composes up to 30% of the animal membrane lipids and regulate several biophysical characteristics biological membranes.

The basic arrangement of lipids, and in particular phospholipids, into bilayers of stereotyped thickness (~10 nm) is determined by their amphipathic nature (Tristram-Nagle & Nagle, 2004). Owing to the hydrophobic effect, the tails cluster into micelle to refuge the aqueous intracellular and extracellular environments. The consequent increase in the entropy of the system is mitigated by the conversion of the micelle into continuous bilayers in which the lipid tails are hidden into its interior while being shielded by the hydrophilic heads, which conversely point outward.

Proteins and glycoproteins of biological membranes can be categorized using different criteria, namely their class (*e.g.* enzymes, structural proteins, transport proteins), their function (*e.g.* receptors, ion-channels, adhesion molecules) or their position in the lipid bilayer (*i.e.* peripheral proteins, integral proteins, transmembrane proteins) (Alberts et al., 2015). The PM is crowded with proteins, which in mammalian cells constitute around 50% of its mass corresponding to an area occupancy of roughly 25% (Dupuy & Engelman, 2008). This challenges the classic textbook view that illustrates the PM as “a sea of lipids with embedded sparse proteins”. On the contrary, the PM is a very crowded environment and proteins contribute to its physicochemical properties as much as lipids.

1.1.2. The cell cortex

The cell cortex is an actomyosin layer found beneath the PM of all the animal cells and most of the protozoans. From a functional perspective, numerous authors have described the cell cortex as an analog of the cell wall, especially since both regulate cell shape and resist intracellular pressure (Salbreux et al., 2012). However – as described in details below – the cell cortex is a much more dynamical structure in terms of molecular composition, architecture variability and biological functions (Morris & Homann, 2001).

1.1.2.1. Cortex composition

The principal components of the cortex are filamentous Actin, myosin motors and Actin-associated proteins. Actin filaments constitute the cytoskeletal scaffold of the cortex and Actin-associated proteins regulate its architecture, biophysical properties and biological activity. A comprehensive description of these proteins and their function is beyond the scope of this thesis (Biro et al., 2013) (reviewed in (Chugh & Paluch, 2018)). In broad terms, Actin-associated proteins relevant for the biophysics of the cortex can be classified into three groups: Actin remodeling factors, crosslinkers and motor proteins (reviewed in (Winder, 2005)). The first group includes Actin polymerization factors (*e.g.* Arp2/3 complex and Formins), Actin capping and severing proteins (*e.g.* Gelsolin and ADF/Cofilin), and monomer binders (*e.g.* Thymosin and Profilin). Crosslinkers (*e.g.* Fimbrin, Filamin, Spectrin) are responsible for the generation of higher-order Actin networks: they contain multiple Actin binding sites which allow them to crosslink or bundle filaments. These proteins are crucial elements of the cell cortex since they govern its architecture and elasticity. The last group of Actin associated proteins consists of Myosin-I(s) and non-muscle Myosin-II(s). By burning ATP, these motor proteins slide Actin filaments against each other and thus they turn the cortex into a prestressed contractile system. In addition,

Myosin-II molecules, which self-assemble into minifilaments, act as Actin crosslinkers (Laevsky, 2003).

In addition to the actomyosin cortex, immediately beneath the PM there is an extremely thin layer of Spectrin directly connected to the lipid bilayer and the cortical actin (reviewed in (Kapus & Janmey, 2013)). This structure, named 2D cortex, is often neglected since its mechanical properties seem to have a little impact on the cell surface. However, in erythrocytes and other cell types lacking of an actomyosin cortex, the 2D cortex becomes a major cytoskeletal component and determines most of the cell mechanics (Mikkelsen et al., 1984) (Han et al., 2017).

1.1.2.2. Cortex architecture

The thickness and the architecture of the cortex are crucial characteristics of this structure. They vary considerably according to cell type, subcellular domain, cell cycle phase, adhesion state of the cell, extracellular matrix characteristics, and specific biological responses carried out by the cell (reviewed in (Tatyana M. Svitkina, 2020)). Measurements of these parameters are hampered by the fact that the cortex is a diffraction-limited structure. Indeed, its thickness ranges from 50 nm – *e.g.* in the basal domain of mouse embryonic stem cells – to 400 nm – *e.g.* in HeLa cells in suspension (Ramanathan et al., 2015) (Chugh et al., 2017) (Clark et al., 2013) (Kumar et al., 2019) (Clausen et al., 2017) (Xia et al., 2019) (Laplaud et al., 2020) The spatial arrangement of the Actin filaments in the cortex is equally variable. According to the most simplistic but particularly useful depiction, cortical Actin organization can range between two extremes: isotropic and anisotropic architectures (Tatyana M. Svitkina, 2020). In an isotropic cortex, Actin filaments display quasi-random orientations and form an intricate meshwork. This type of cortex has been observed in different cell types, for example HeLa and mouse embryonic stem cells (Morone et al., 2006) (Guillaume T. Charras et al., 2006) (Chugh et al., 2017) (Xia et al., 2019) (Chikina

et al., 2019). On the anisotropic extreme, actin filaments are arranged in bundles parallel to each other and to the PM. Remarkable examples are the dorsal cortices of fibroblasts and keratinocytes (Svitkina, 1989) (Eghiaian et al., 2015).

Actin density is another important descriptor of the cortex biophysics. It can be broadly defined as Actin mass per unit volume (Fischer et al., 2009). To the best of my knowledge, a strict and quantitative definition of cortical Actin density in cell is missing, and in literature this term is loosely used to qualitatively describe the degree of entanglement of the cortical meshwork (see examples in (Joanny et al., 2013) (Clausen et al., 2017) (Xia et al., 2019)). This is a key structural aspect since it determines the diffusion coefficient through the cortex and the ability of proteins to interact with the Actin filaments. For instance, extremely high Actin density induces the exclusion of myosin-II minifilaments leading to a softer cortex (Chaigne et al., 2013). Paradoxically, too low density leads to similar results: the cortex softens up because myosin-II minifilaments are too short to crosslink and contract Actin (Xia et al., 2019).

1.1.2.3. Cortex regulation and dynamics

Cortex dynamics depends on multiple levels of regulation ranging from Actin dynamics, to cross-linking degree, to contractility of the system. (reviewed in (Chugh & Paluch, 2018)).

Actin forms polarized biopolymers whose extremities – namely *barbed end* and *pointed end* – display different biochemical features (reviewed in (Carlsson, 2010)). Elongation and shortening of the filaments depends on the differential kinetics of incorporation/removal of monomers at the extremities. Specifically, Actin polymerization is favored at the barbed end while depolymerization is predominant at the pointed end. At the steady state, the length of the filaments is kept constant since the rate of monomers incorporation at the barbed end (k_{on}) matches the dissociation rate at the pointed end (K_{off}). This phenomenon is called treadmilling.

The growth of single filaments and entire Actin networks is regulated by Actin-remodeling proteins and can be subdivided in three main steps: nucleation, polymerization, depolymerization (reviewed in (T. D. Pollard et al., 2001) (Carlsson, 2010)). In the cell cortex, the main Actin nucleators are the Arp2/3 complex and the Formin mDia1 (Bovellan et al., 2014). Arp2/3 complex creates Actin nucleation cores from the side of a pre-existing filament with a distinctive 70˚ angle of emergence (Rouiller et al., 2008). These characteristics, as well the low processivity of polymerization, make Arp2/3 complex responsible for the generation of branched Actin networks characterized by short filaments (B. A. Smith et al., 2013). On the contrary, Formins nucleate filaments *de novo* and elongate them from the barbed end by adding Actin monomers with high processivity and preventing capping (reviewed in (Kovar & Pollard, 2004) (Breitsprecher & Goode, 2013)). Therefore, mDia1 is responsible for the formation of anisotropic cortices characterized by parallel long filaments.

Actin nucleation, polymerization and depolymerization are regulated by dozens of Actin-remodeling factors. Monomeric Actin-binding proteins can either promote depolymerization by sequestering monomers (*e.g.* Thimosin β4) or favor filaments elongation (*e.g.* Profilin) (Goldschmidt-Clermont et al., 1992). Capping proteins block either Actin polymerization or depolymerization by binding the barbed end or the pointed end respectively (reviewed in (Edwards et al., 2014)). Lastly, Actin severing proteins are key players when a domain of the cortex needs to be reorganized or restructured, for instance to carry out a specific cellular function (reviewed in (Ono, 2007)).

The second layer of regulation of the cortex dynamics is determined by the crosslinking degree of the network. In the most simplistic definition, crosslinking is the process of linking together different Actin filaments through specialized proteins; this phenomenon leads to the formation of interconnected Actin networks such as the cortex (Blanchoin et al., 2014). All these specialized proteins, named Actin crosslinkers, display a conceptually similar structure: they possess two or more filamentous Actin binding domains separated by a more or

less rigid hinge (Thomas D Pollard, 2016). The number of Actin binding sites, their orientation, and the length of the hinge determine the geometry of the filaments network which can range from perpendicular arrays to bundles. Several crosslinkers have been shown to be active in the cell cortex, including α-Actinins, Filamins, Fascin, Fimbrin, and Spectrin (reviewed in (Chugh & Paluch, 2018)). Aside from being regulators of its architecture, these crosslinkers are crucial for other two aspects of the cortex: elasticity and turnover. The cortex turnover determines the timescale of its viscous behavior. This property is indeed dominated by crosslinkers turnover since in general is five- to tenfold faster than that of the actin filaments and myosin minifilaments (Salbreux et al., 2012) (Fritzsche et al., 2013). The viscoelastic behavior of the cortex will be discussed in details in section *1.2.2.1*.

Finally, the last layer of regulation of the cortex dynamics depends on non-muscle Myosin-II minifilaments. As already introduced above and as discussed in section *1.2.2.2.*, Myosin-II converts the cortex into a contractile prestressed structure. This state has two main repercussions in respect to the cortex dynamics: it generates cortical flows in the plane of the PM, and rapid oscillation of cortex thickness. Cortical flows are determined by anisotropies in the contractility of the cortex, or more specifically cortical tension gradients (Mayer et al., 2010). Actin filaments and myosin minifilaments flow from regions of high cortical tension to regions of low cortical tension, aiming to equilibrate this mechanical property. These asymmetries are actively regulated by the cell that takes advantage of the consequent flows to exert specific biological functions, such as cell migration and establishment of cell surface polarity (Munro et al., 2004) (Bergert et al., 2015).

In opposition to cortical flows – that have been observed for several decades (Bray & White, 1988) – rapid contractility-dependent oscillations of the cortical thickness have been noticed only very recently. This can be attributed to the lack of methods to image the cortex *in cellulo* at high spatial and temporal resolution. However, In a recent study, Piel and colleagues have implemented a

label-free technique that allows to measure the variation of cortex thickness over time in live cells (Laplaud et al., 2020). The so-called magnetic pincher is based on the use of two microbeads, one phagocyted by the cell and one in the extracellular environment. Through the application of a magnetic field, the two beads are moved next to the cell surface where they pinch it. By measuring the distance between the center of the beads over time, the authors observed fluctuations of the cortex thickness about 3-fold with oscillatory period of ~60 s; inhibition of Myosin-II activity completely suppresses them. This phenomenon is extremely interesting, nevertheless its biological significance and its regulation are unclear.

1.1.3. Membrane-to-Cortex Attachment

Membrane-to-Cortex Attachment (MCA) is the physical connection between the plasma membrane (PM) and the cell cortex (reviewed in (Kapus & Janmey, 2013) (Diz-Muñoz et al., 2018)). In cells, MCA is mainly mediated by the activity of specialized proteins named MCA linkers. Importantly, not all the linkers have been yet identified, owing to functional redundancy and the presence of less specific interactions between membrane protein complexes, adapter proteins and Actin-binding proteins in the cortex (Kapus & Janmey, 2013). Furthermore, many authors believe that fully unspecific interactions, that is electrostatic and Van der Waals attractions, contribute to MCA in cell (M. P. Sheetz, 2001) (Diz-Muñoz et al., 2018). Indeed, several *In vitro* studies showed that both monomeric and filamentous Actin *per se* can be adsorbed to positively charged artificial lipid bilayers; in some instances these interactions are strong enough to induce Actin filaments nucleation, polymerization and bundling (Laliberte & Gicquaud, 1988) (St-Onge & Gicquaud, 1989) (Renault et al., 1999) (A. P. Liu et al., 2008) (Schroer et al., 2020). However, both the inner leaflet of the PM and Actin filaments are negatively charged and thus should repulse each

other (G. Li et al., 2005) (T. Yeung et al., 2008). Therefore, it is not clear whether, and to what extent, these unspecific interactions occur in cell.

The understanding of MCA is limited not only by the incomplete characterization of PM-cortex interactions, but also by the partial insight on its contribution to the biophysics and the biological function of the cell surface. Indeed, MCA is the least studied layer of the animal cell surface, albeit its importance in cell biology was already postulated 20 years ago (M. P. Sheetz, 2001).

1.1.3.1. Linker-mediated MCA

The archetype of all MCA linkers consists of a PM-binding domain, a flexible hinge and a filamentous Actin-binding domain; thence it is able to tether the PM to the cortex directly. Furthermore, its functions are actively regulated by the cell, either transcriptionally/translationally or at the post-translational level. According to these general features, quite a high number of proteins can potentially display MCA activity (Kapus & Janmey, 2013). Nevertheless, so far only a small group of proteins has been shown to act consistently and systematically in various cellular contexts as MCA linkers (table 1.1).

Table 1.1. List of known MCA linkers.

MCA linker	Description	References
ERMs	Canonical MCA linkers. See the main text for further details.	(Bretscher et al., 2002)
Myosin-I(s)	Actin motor proteins which bind directly the PM through C-terminal THs domains.	(Nambiar et al., 2009)
Filamins	Dimeric Actin-crosslinkers. They bind different PM proteins, including integrins and Caveolin-1.	(Sharma et al., 1995) (Stahlhut & van Deurs, 2000)
Ankyrin	it links the PM to the 2D cortex by simultaneously binding to various TM proteins and to Spectrin.	(Bennett & Chen, 2001)

Septins	upon binding to PIP2 in the PM, they form filamentous array and interact with various Actin binding proteins.	(Gilden & Krummel, 2010)

The ERM family is the most well characterized group of MCA linkers. In vertebrates, this family counts 3 members (Ezrin, Radixin and Moesin) which display similar architecture and biochemical regulation (Sato et al., 1992) (reviewed in (Bretscher et al., 2002)). From a structural standpoint, each of these proteins can be subdivided in two parts: N-ERMAD and C-ERMAD which are the N-terminal and C-terminal halves respectively (Gary & Bretscher, 1995). N-ERMAD and corresponds to the FERM domain (~300 amino acids), a clover-shaped PM-binding domain present in various proteins (reviewed in (Chishti et al., 1998)). It contains three subdomains (F1, F2 and F3) that have different architectures and binding partners (Pearson et al., 2000). F2 domain binds directly to phosphatidylinositol 4,5-bisphosphate (PIP2) in the PM (Blin et al., 2008), while other subdomains bind different transmembrane (TM) proteins; for instance the FERM domain of Ezrin binds, among others, CD43, CD44 and ICAMs (Delon et al., 2001) (Legg & Isacke, 1998) (Barreiro et al., 2002). ERMs bind the PM also indirectly through the interaction with adapter proteins such as EB50 (Fouassier et al., 2000). C-ERMAD is connected to N-ERMAD via a flexible α-helical hinge and it contains a short Actin-binding domain (~ 34 amino acids) (Q. Li et al., 2007) (Turunen et al., 1994).

The primary level of regulation of ERMs is post-translational. All the three proteins are in equilibrium between open and closed conformational states. In the closed configuration, N-ERMED tightly binds C-ERMAD masking the Actin-binding site and reducing its avidity for the PM (Gautreau et al., 2000). This conformation is considered to be dormant since it is not able to crosslink the PM to the cortex. Furthermore, closed Moesin and Ezrin form homo- and hetero-oligomers which are hypothesized to favor further inactivation by masking other binding sites (L. Zhu et al., 2005). The initial step of the conformational switch to the active form is favored by the binding between the FERM domain to PIP2,

which leads to the exposure of a phosphorable threonine in C-ERMAD (T567, T558, T564 in Human Ezrin, Moesin and Radixin respectively) (Fievet et al., 2004). Subsequently, phosphorylation of that residue promotes monomerization and full opening of the ERMs. In this configuration, ERMADs interaction is disrupted and the consequent unmasking of the Actin-binding sites leads to activation of the MCA activity. Several protein kinases have been recognized to target ERMs, including Rho-associated protein kinase (ROCK) and protein kinase C-α (PKC- α) (reviewed in (Fehon et al., 2010)).

Myosin-I family constitutes another important group of MCA linkers (Nambiar et al., 2009). Their structure is quite heterogenous, nevertheless they display a few conserved features such as a N-terminal motor head and a C-terminal atypical Pleckstrin homology (PH) domains (named THs) (reviewed in (Coluccio, 2008)). The former binds filamentous Actin in an ATP- and Ca^{++}-dependent manner while the latter associates to the PM by binding PIP2.

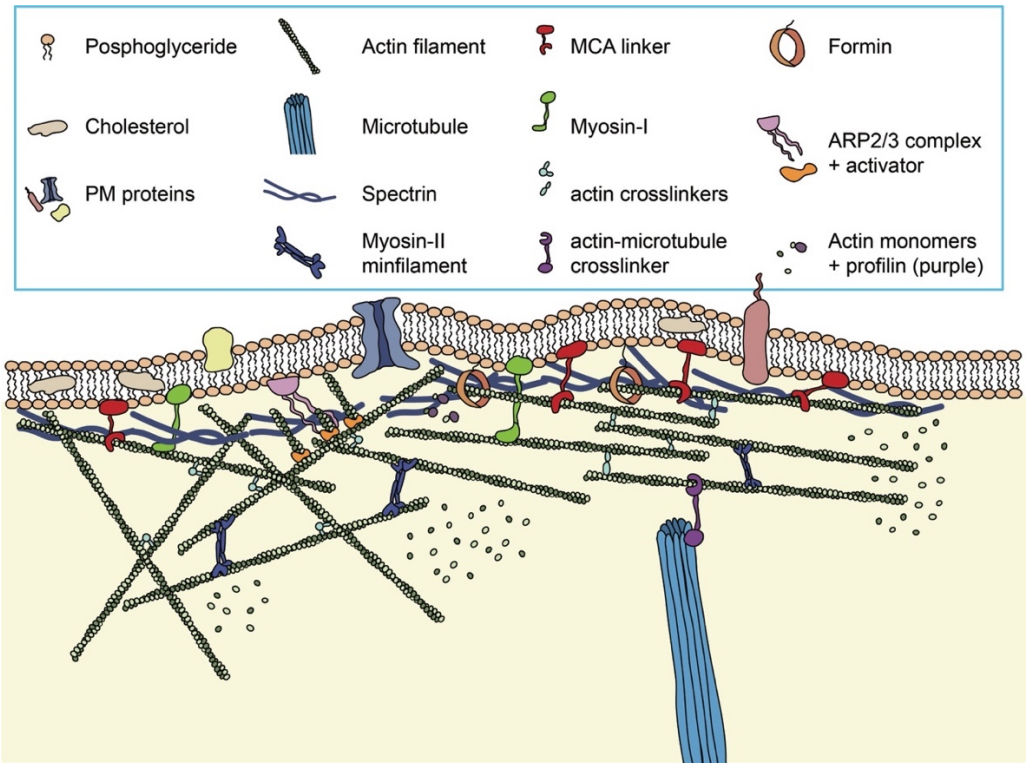

Figure 1.1. Animal cell surface at a glance.From the top to the bottom, it is possible to identify three different structures: the PM, the Spectrin-based 2D cortex, and the

actomyosin cortex. The PM is constituted of a lipid bilayer (mainly Phosphoglycerides) with embedded proteins. The PM is linked to the cortex via MCA linkers (including Myosin I). The actomyosin cortex is composed of actin filaments connected by crosslinkers and myosin-II minifilaments. On the left side the cortex is isotropic owing to the nucleation activity of the Arp2/3 complex. On the right side anisotropy is favored by the Formins-mediated polymerization of longer Actin filaments. The actomyosin cortex is connected to other cytoskeletal structures as show by the exemplary crosslink to a microtubules.

1.2. Mechanics of the cell surface

The study of the mechanical properties of the cell surface can be traced back to the end of the nineteenth century, when the German the zoologist Adam Otto Bütchilli noticed that the high surface tension of alkaline water droplets immerged in olive oil leads to streaming movements reminiscent of amoeba's ones (Butschli, 1892) (Armstrong & Hanczyc, 2013). This made him speculate that cells are characterized by a surface tension which in turn might drive cell functions such as migration.

The surface of an animal cell is a multilayered structure that emerges from a sophisticated organization of a large number of elements with different biochemical and biophysical features. This composite material exhibits complex mechanical behaviors which are actively regulated and exploited by the cell to carry out biological processes.

The aim of the following sections is to provide an exhaustive description of the mechanical properties of animal cell surface. Owing to the complexity of the system, each layer will be at first discussed independently, in a reductionistic fashion.

1.2.1. Biophysical description of biological membranes

The complex architecture and composition of biological membranes underlies their equally complex biophysical behavior. Indeed, as expected from a composite material, biological membranes are viscoelastic structures, that is, they display properties of both fluids and solids (Rand, 1964). Importantly, the type of behavior, *i.e.* solid- or liquid-like, depends on the method used to observe or perturb the membranes: the temporal and spatial scales under investigation, as well the nature and intensity of a perturbation stimulus, elicit different responses (Evan A. Evans & Hochmuth, 1976). As a consequence, a considerable

number of biophysical models of the PM have been developed (reviewed in (Lim et al., 2006)).

1.2.1.1. The fluid mosaic model and its updates

The fluid mosaic model describes the fluid behavior of the PM on the mesoscale (~2-1000 nm) and on time scales relevant for biochemical processes (~10-100 ms). According to this model, the lipid bilayer behaves as a quasi-2D fluid in which both lipids and proteins are able to move freely along the bilayer plane (*i.e.* in-plane diffusion) (Singer & Nicolson, 1972). The mosaicism is given by the differential interactivity among the membrane components: proteins cluster into complexes, lipids display preferential affinity to specific lipids and proteins, and fluidity is modulated by the local concentration of cholesterol. All these phenomena lead to the formation of nanodomains characterized by lower entropy and fluidity, which together are nowadays denoted as the liquid ordered phase of a membrane (Wu et al., 2016).

Over the course of the past 40 years, several observations have challenged the classic fluid mosaic model that has been implemented and re-thought accordingly (Nicolson, 2014). A considerable incongruity between the original model and the experimental data was in relation to the type of in-plane motion of molecules in the PM. Using high-speed single-particle tracking methods, it was indeed observed that lipids and TM proteins do not exhibit simple Brownian diffusion, as predicted by the model (M. P. Sheetz et al., 1989) (de Brabander et al., 1991) (P. R. Smith et al., 1999). Conversely, these molecules undergo hop diffusion: Brownian motion is restricted to small physical compartments (200-700 nm-diameter) whose boundaries are occasionally crossed in a stochastic fashion (reviewed in (Kusumi et al., 2005)). These findings have been reconciled with the theory by the anchored picket-fence model which states that PM compartmentalization originates from the Actin-Spectrin network in the 2D cortex (the fences) and the TM proteins anchored to it (the pickets) (figure 1.2) (Morone et al., 2006).

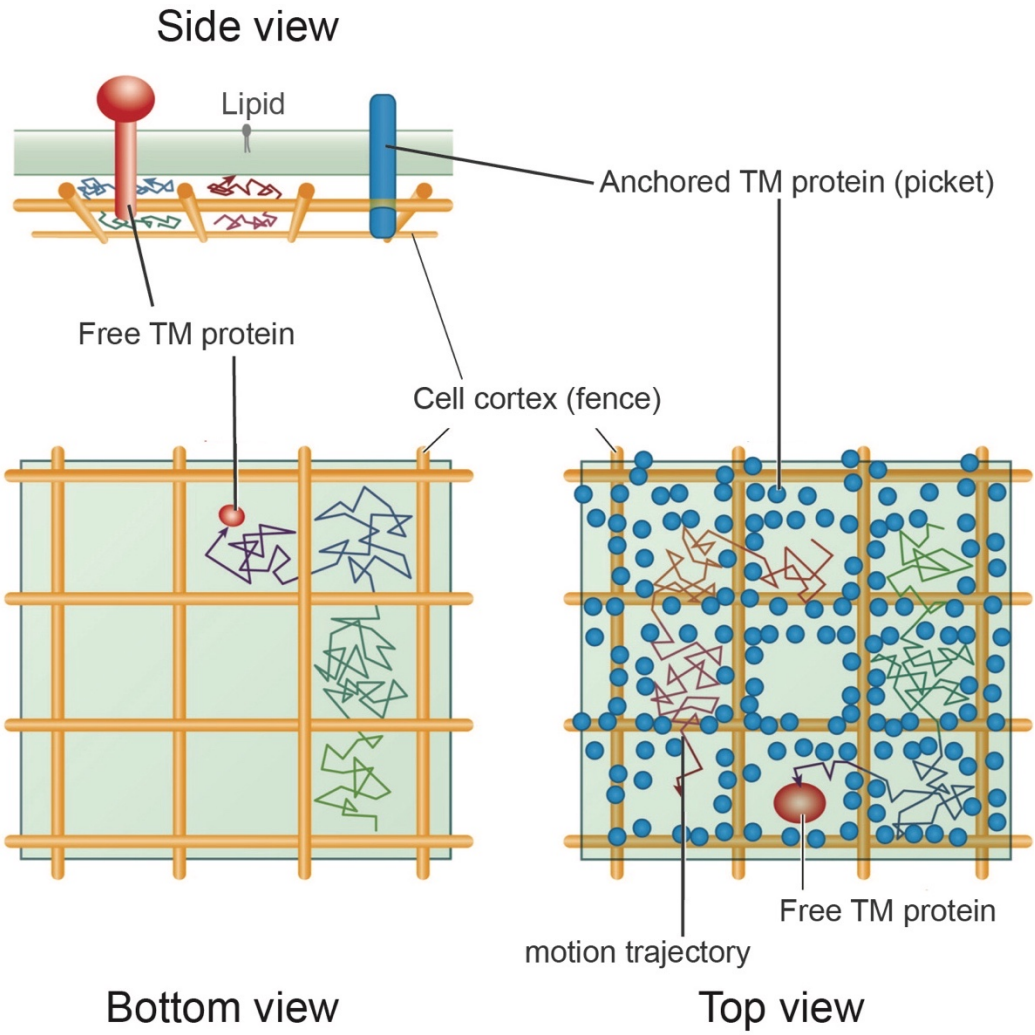

Figure 1.2. Picket-fence model and hop diffusion. The cortex forms an intricated network (fence) pinned to the PM by MCA linkers and TM proteins (pickets). Non-anchored PM proteins and lipids are free to diffuse within a compartment whereas boundaries are occasionally crossed (hop diffusion). Modified from (Kusumi et al., 2012).

According to the model, within a compartment both lipids and non-immobilized proteins diffuse freely and the coefficients of diffusion conform to the predictions of the mosaic fluid model (reviewed in (Kusumi et al., 2011)). The cytoskeletal filaments juxtaposed to the PM physically impede the transfer of proteins to other compartments while lipids are constrained by the steric hindrance and transient interaction with the immobile TM proteins (Morone et

al., 2006) (Fujiwara et al., 2016). Finally, the hop movement is facilitated by thermal fluctuations of the PM, discussed in *1.2.1.4*, which temporary loose the barriers and promote escape of molecules from the compartment.

1.2.1.2. Viscoelasticity of the plasma membrane

The motion and deformation of the PM upon application of forces has been extensively studied using continuum mechanics approaches (Cueto & González, 2018). This subfield of mechanics treats objects as continuous isotropic bodies, and classifies them into elastic, plastic, viscoelastic and viscous (Newtonian and non-Newtonian) materials (see table 1.2).

Table 1.2. Major descriptors of motion/deformation in continuum mechanics.

Property	Definition
Elasticity	Ability of a solid to store mechanical energy and regain its original shape after removing the deforming stress.
Plasticity	Ability of a solid to undergo non-reversible deformation upon the application of mechanical stress.
Viscosity	Measure of the resistance of a fluid deformation/flow owing to internal frictional energy. In Newtonian fluids, viscosity is independent of shear rate.
Viscoelasticity	Property of objects of exhibiting both elastic and viscous behavior upon application of mechanical stress.

The PM can be modeled as an incompressible 2D viscoelastic layer, capable of recoverable (*i.e.* elastic) deformations with internal viscous energy dissipation (Evan A. Evans & Hochmuth, 1976). A common tool used by biophysicists to describe such a complex behavior is rheological modeling (Rand, 1964) (Ehrenstein & Iwasa, 1996) (Craiem & Magin, 2010). The basic idea behind this method is to portray viscoelasticity as a circuit diagram in which the elastic components (springs) and the viscous components (dashpots) are combined in parallel and/or series (figure 1.3) (reviewed in (Marques & Creus, 2012)).

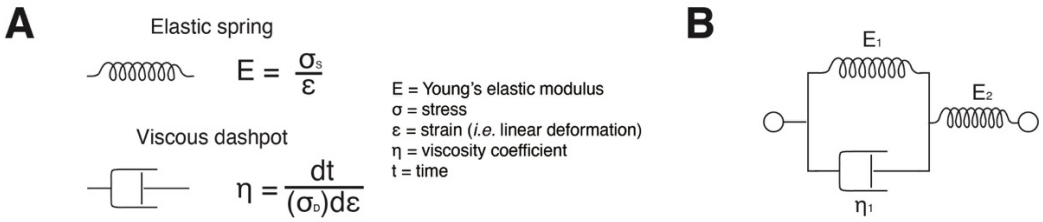

Figure 1.3. Basics of rheological modelling.
(A) Springs and dashpots represent elastic and viscous components respectively. On the right, the Hooke's law (top) describes mathematically the elastic behavior whereas the Newtonian law of viscosity (bottom) describes **viscous** one.
(B) Exemplary circuit diagram. How these components are mathematically combined is beyond the scopes of this thesis.

This approach has been very useful to predict the behavior of the PM under experimentally induced stress, nevertheless it has limitations that make it expendable in biologically relevant contexts (reviewed in (Vincent, 2012)).In particular, it is valid only for uniaxial stresses which lead to linear elastic and viscous responses, described by the Hooke's law and the Newton's viscosity law respectively (equations in figure 1.3A). Consequently, it fails at addressing deformations of the PM non-linearly correlated to the applied stresses.

The elastic properties of the PM are related to its resistance to deformation, while viscosity refers to its resistance to a rate of deformation, that is, the change of deformation over time (E.A. Evans & Hochmuth, 1976). As the PM is assumed to be an incompressible 2D structure, it can undergo three fundamental types of deformation: area expansion, shearing and bending. (figure 1.4).

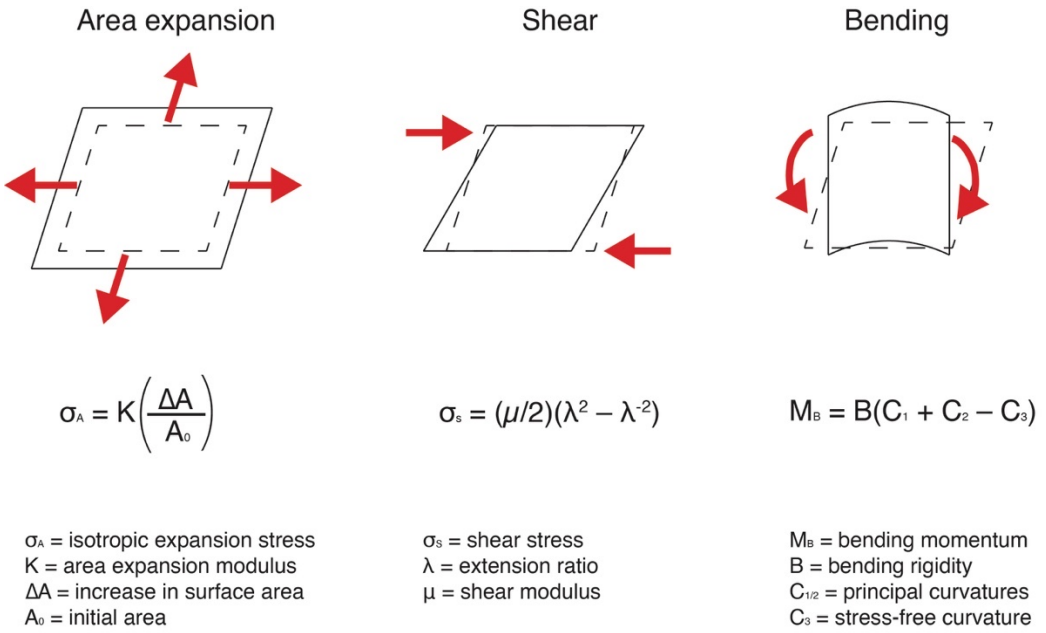

Figure 1.4. Fundamental types of deformation of the PM. (top) Schematic of the three types of deformation of a 2D membrane; dashed lines = original shape, solid lines = shape after deformation; red arrows = strain direction. (bottom) Stress-strain relationships.

Given its time-independence, elasticity can be quantified by determining the elastic moduli from the relation between the three stress types and the consequent strains (as defined in figure 1.4). Therefore, the PM is characterized by an area expansion modulus *K* (measured in N/m), a shear modulus μ (measured in N/m), and bending rigidity *B* (measured in Nm or K_BT) (reviewed in (E.A. Evans & Hochmuth, 1978)). These moduli have been measured extensively in both artificial vesicles and cells, and using a wide plethora of techniques (reviewed in (Diz-Muñoz et al., 2018)). Notwithstanding, the measured moduli cannot be reliably compared since strongly influenced by intensity/duration of the applied stress, biophysical method, temperature and cortex mechanics (Evan A. Evans & Hochmuth, 1976). In general, it can be stated the PM is basically inextensible/incompressible owing to a very high area compression modulus. Conversely, the extremely low shear modulus implies it behaves as a quasi-fluid in agreement with the fluid mosaic model. Finally, the bending modulus is highly

variable because extremely sensitive to lipid composition, peripheral integral PM proteins and MCA (reviewed in (Dimova, 2014)).

The most prevalent viscous response of the PM is induced by shear stress owing to the low shear modulus which allows a relatively large range of strains and consequent lipid flow (R. M. Hochmuth & Waugh, 1987). The coefficient of shear viscosity η is obtained by measuring the time the PM takes to recover its original shape after being released from an applied shear stress (*i.e.* relaxation time) (Engelhardt & Sackmann, 1988).

1.2.1.3. Membrane tension

By definition, biological membranes function as boundaries, and hence their biophysical behavior is influenced by the interactions with the neighboring compartments (Kozlov & Chernomordik, 2015). These interactions are best explained using statistical thermodynamic arguments: two phases try to minimize their Gibbs free energy by drawing as many molecules as possible in their respective bulks, and thus by reducing the area of the interphase (Safran, 2018). Therefore, the existence *per* se of an interphase has an energetic cost, which is quantifiable as surface tension, *i.e.* the energy per unit area of interphase (measured in J/m^2 or N/m).

In biological membranes, the surface tension is also known as in-plane tension (T_m), defined as a measure of the energetic cost of increasing membrane area (Sitarska & Diz-Muñoz, 2020). Several studies showed that flat lipid membranes have zero in-plane tension, and this is achieved by the arrangement of lipids into bilayers with optimized lipid packing (Brochard et al., 1976) (reviewed in (Jähnig, 1996)). Notwithstanding, in-plane tension is positive in both artificial vesicles and cells (~$1\text{-}3*10^{-2}$ mN/m) owing to unbalanced external forces applied to the membrane (Kwok & Evans, 1981) (Jianwu Dai & Sheetz, 1999). These forces, such as intracellular pressure, induce an expansion of the surface

area of the membrane and a consequent variation in the lipid packing degree, which in turn dictate an increment of the in-plane tension (Safran, 2018).

The fluid nature of a biological membrane determines its ability to equilibrate in-plane tension throughout its surface. The application of a force on a specific membrane subdomain induces a local increase in in-plane tension. Such increase is then compensated by the lateral flow of lipids and proteins toward that region, leading to a partial restoration of the optimal lipid packing degree. As a result, a sub-optimal lipid packing degree is generated throughout the whole membrane which redistributes the increased in-plane tension (Chizmadzhev et al., 1999). In artificial lipid vesicles, such re-equilibration occurs almost instantaneously (E. Evans & Rawicz, 1990) whereas in the PM of cells, lipid flow is hindered by the 2D cortex and MCA (Shi et al., 2018) in accordance with the picket-fence model.

1.2.1.4. Plasma membrane fluctuations and curvature

In the previous sections, I have mainly analyzed the biophysics along the plane of the lipid bilayer, modeled as a bi-dimensional structure. However, the PM is embedded in a three-dimensional space, where its behavior is governed by three phenomena: fluctuations, curvature and thickness variation (reviewed in (Monzel & Sengupta, 2016) (Jarsch et al., 2016)). For the sake of understandability, the latter subject will not be covered in this thesis, and the PM will be assumed to have fixed thickness.

In statistical mechanics of active systems, membrane fluctuations are defined as stochastic deviations of the surface area along the depth-axis from the value of minimal free energy (Helfrich, 1973). In simpler terms, they are undulations of biological membranes along their z-axis caused by temperature-dependent random movements (figure 1.5A).

Figure 1.5. Thermal fluctuations in biological membranes.
(A) Schematic of fluctuations.
(B) Increasing in-plane tension reduces the amplitude and frequency of the fluctuations.

The energetic cost of PM fluctuations is determined by three different parameters: bending rigidity (*i.e.* the energy required to curve the membrane); in-plane tension (*i.e.* the energy required to increase the surface area, figure 1.5B); and the adhesion energy derived from the interaction with the surrounding, in particular MCA (Mutz & Helfrich, 1990) (Monzel & Sengupta, 2016) (Alert et al., 2015).

Membrane fluctuations have been measured with various techniques and in different model systems (reviewed in (Monzel & Sengupta, 2016)). Their amplitudes vary from ~ 70 nm in artificial vesicles, to ~ 50 nm in red blood cells, to ~ 20 nm in macrophages. Interestingly, depletion of ATP has been shown to lead to a substantial reduction of membrane fluctuations, strongly suggesting that cells actively regulate this phenomenon (Gov & Safran, 2005) (Park et al., 2010).

Another type of membrane deformation in the depth-axis is curvature. This phenomenon has been shown to affect the in-plane diffusion of lipids and proteins, and it can be either spontaneous or induced. Spontaneous curvature arises from the asymmetric distribution of lipids between the two leaflets. Lipids hindrance varies according to the number of saturated acyl groups in their tails: double bonds generate rigid kinks that increase the physical space occupied by a lipid. Consequently, asymmetric distribution of lipids between the two leaflets generates an asymmetric tension due to different degrees of packing. The tension difference is then balanced by the generation of a curvature: the

membrane bulges out toward the denser leaflet reducing tension in it. Conversely, curvature leads to an increase in lipids packing degree (and thus tension) in the other leaflet. Importantly, asymmetric crowding of integral membrane proteins between the two leaflets also contributes to the generation of spontaneous curvature: curvature bulges out towards the most crowded leaflet, reducing its protein density and tension. Both lipid asymmetry and protein crowding are tightly regulated by the cell suggesting important biological roles for spontaneous curvature.

Formation of induced curvature is mediated by proteins and occurs in a wide plethora of processes, ranging from cell protrusion formation (discussed in section *1.3.2.*), to generation of PM reservoir, to vesicle trafficking at the PM (figure 1.6) (reviewed in (Jarsch et al., 2016)).

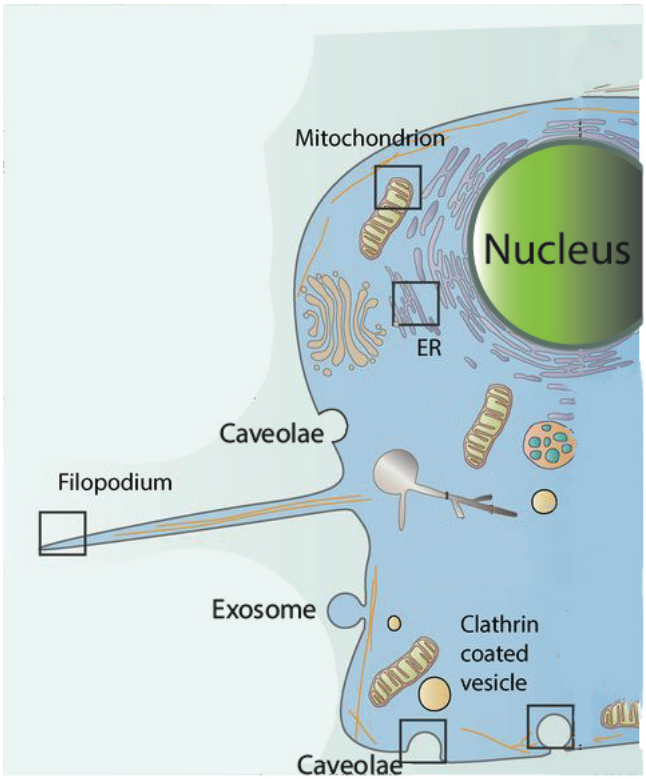

Figure 1.6. Plasma membrane curvature. Schematic of the cell whose some of the curvatures have been marked. Modified from (Jarsch et al., 2016).

1.2.2. Cell cortex mechanics

The actomyosin cortex biophysics are arguably even more complex than the PM ones. Various factors contribute to the mechanical properties of this cytoskeletal layer, including protein turnover, crosslinking degree, myosin motors activity, architecture and thickness of the network, macroscopic mechanics of the network, and interaction with the surrounding (reviewed in (Kelkar et al., 2020)). Notably, the emerging macroscopic properties of the cortex have a far greater impact on the mechanics of the cell than individual actin filaments mechanics (Salbreux et al., 2012). Consequently, actin filaments can be modeled as simple linear springs whose bending rigidity correlates to their persistence length, that is, the max length over which the orientation of the filaments is preserved (10-15 μm) (Bausch & Kroy, 2006) (Ott et al., 1993).

In the following sub-sections, the main cortex mechanics will be discussed. Importantly, some basic concepts (*e.g.* definition of viscoelasticity and surface tension) will be not be explained since already covered in the section *1.2.1*. Furthermore, refer to section *1.1.2.2.* for a detailed description of the structure and turnover of the cortex.

1.2.2.1. Cell cortex elasticity and viscoelasticity

At the essence, the cell cortex is a viscoelastic composite material, structured as a meshwork of crosslinked polymers, and capable of active contraction (Akkas, 1981). From a polymer physics standpoint, the best biophysical description of the cortex comes from the active gel theory which treats it as a polymeric polar hydrogel (reviewed in (Prost et al., 2015)). Albeit a consensus on the definition of polymer gels is missing (Rogovina et al., 2008), the cell cortex presents all their crucial characteristics ranging from its constitution (an elastic three dimensional crosslinked network that absorbs part of fluid in which it is immerged) to the rate-dependent viscoelasticity (Kruse et al., 2004).

The latter feature is dictated by the activity of the crosslinkers: if a stress is applied on timescales shorter than their turnover, the cortex behaves as an elastic solid in the short term, and as a viscoelastic material in the long term (Ananthakrishnan et al., 2006). On the contrary, if the load is applied slowly, the actomyosin flows toward the stressed region in almost a pure viscous fashion region (Fischer-Friedrich et al., 2016). The elasticity of the cortex is described by its Young's modulus (measured in Pa) and its bending rigidity while viscosity η depends on the crosslinking degree and the length of the actin filaments (Chugh et al., 2017).

1.2.2.2. Cortical tension and contractility

The internal stress of the cortex integrated by its thickness defines cortical tension, the major contributor of the total cell surface tension (A. Yeung & Evans, 1989). This mechanical property comprises a passive and an active terms (Carvalho et al., 2013). The passive term emerges from the viscoelastic nature of the cortex and is regulated by different factors, in particular the connectivity and the architecture of the network (figure 1.7A). According to the active gel theory and experimental observations, intermediate crosslinking degree and intermediate actin filaments length assure the maximum cortical tension (Ennomani et al., 2016) (Chugh et al., 2017). Indeed, if the network is too loose (short filaments and/or few crosslinkers) the cortex tends to fluidify and stress cannot propagate. At the other extreme, too long filaments and high level of crosslinking lead to a very rigid cortex that cannot be remodeled. In addition to connectivity, the passive term of cortical tension is determined also by the degree of anisotropy: the higher the amount of antiparallel filaments, the larger is the contractile force that can be generated by myosin-II minifilaments (Salbreux et al., 2009).

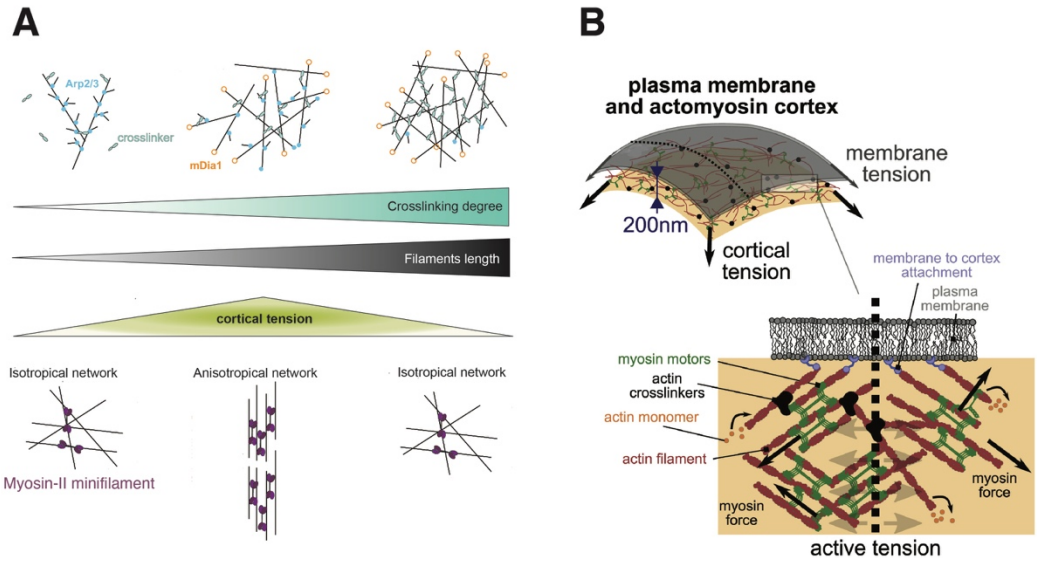

Figure 1.7. Passive and active components of cortical tension. Modified from (Kelkar et al., 2020).
(A) Main regulators of the passive component of cortical tension. Intermediate connectivity (*i.e.* crosslinking degree and filaments length) and level of anisotropy maximize cortical tension.
(B) The active component of cortical tension: Myosin-II mediated contractility.

The active component of cortical tension is governed by the cortex contractility mediated by myosin-II (Paluch et al., 2005), even though there has been shown a non-negligible contribution from myosin-I (figure 1.7B) (Jianwu Dai et al., 1999). Indeed, owing to the ATP- and Ca^{++}-dependent motor activity of myosin-II, minifilamens and actin filaments slide against each other generating a tensile stress which in turn converts the cortex into a pre-stressed structure. Importantly, cortex contractions generate a hydrostatic pressure in the cytoplasm which is a key component and regulator of the total intracellular pressure (Álvarez-González et al., 2015). Lastly, anisotropic contractions induce flow of the cortex toward the regions with higher tension which aim to re-equilibrate the total cortical tension (Mayer et al., 2010).

1.2.3. **Membrane-to-cortex attachment contribution to cell surface mechanics**.

PM tethering to the cell cortex has been postulated to be essential in various mechanically-regulated cellular processes, such us cell shape acquisition, protrusion formation, cell migration, vesicle trafficking, and lateral diffusion within the PM (M. P. Sheetz, 2001) (M. P. Sheetz et al., 2006). Nevertheless, MCA remains the most elusive element of the animal cell surface owing to the incomplete characterization of the MCA linkers and the lack of specific perturbation methods.

MCA contribution to cell surface mechanics was initially uncovered by pulling tethers, lipid nanotubes extracted from the membrane of vesicles or the PM of cells using either optical tweezers or atomic force spectroscopy (figure 1.8A).

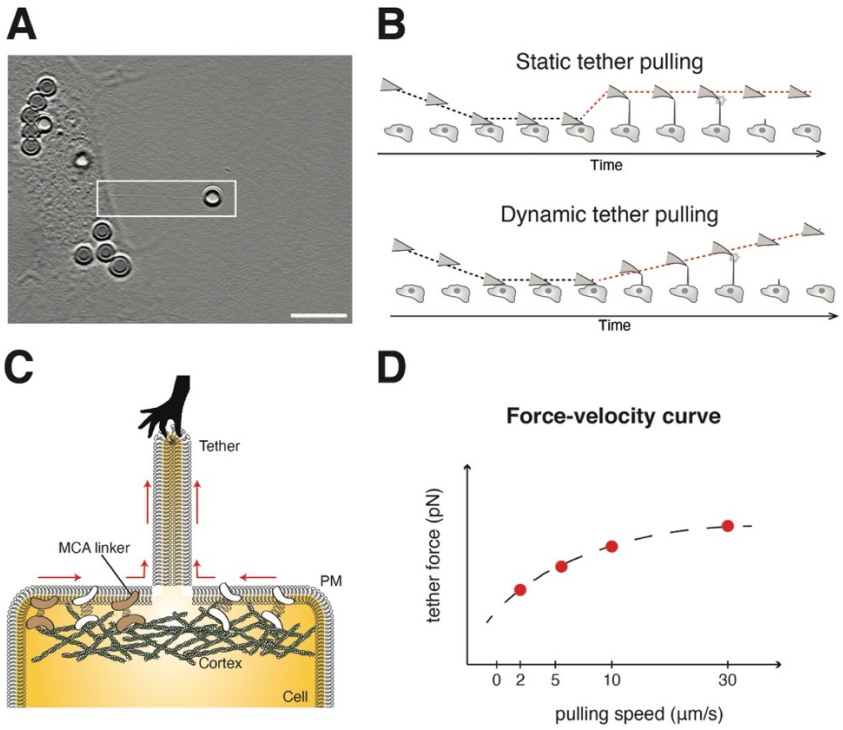

Figure 1.8. Tether pulling experiments.
(A) Micrograph of a tether pulled from a microglial cell with optical tweezers. SB = 10 µm. Modified from (Pontes et al., 2013).

(B) Schematic of static (top) and dynamic (bottom) tether pulling using atomic force spectroscopy.
(C) MCA linkers opposes to lipid flows toward the tether during its extraction.
(D) Exemplary force-speed curve in a dynamic tether pulling experiment. Dashed line = data fitting with the non-linear model from (Brochard-Wyart et al., 2006).

Two different experimental pipelines, namely static and dynamic tether pulling, can be employed to measure different mechanical properties. In static tether pulling, a tether is extracted and hold still (figure 1.8B, top). At the steady state, the force required to hold a tether depends on different variables, as described in:

$$f_0 = 2\pi\sqrt{2TB}$$

Where f_0 is tether force at 0 m/s velocity, T is apparent membrane tension, and B is the bending rigidity of the PM (Robert M. Hochmuth et al., 1996). Since f_0 and B is commonly assumed to be constant for a specific cell line/type (Pontes et al., 2013), tether pulling is used to measure apparent membrane tension, which in cells corresponds to:

$$T = T_m + \gamma$$

Where T_m is in-plane tension and γ is the adhesion energy (measured in J/m^2 or N/m) between the PM and the cortex originating from MCA (Robert M. Hochmuth et al., 1996). Consequently, MCA contributes to the tension in the PM by adding an adhesion energy term, which notably, in different cell lines has been to be several fold larger than in-plane tension (Jianwu Dai & Sheetz, 1999).

Another contribution of MCA to cell surface mechanics, can be uncovered and measured by running dynamic tether pulling experiments in which tether force is measured while pulling a tether (figure 1.8B, bottom). In this experimental setup, MCA influences cell surface viscosity: as the lipids flow into the tether they have to go around MCA interactions (figure 1.8C) and thus, the

higher MCA the harder it will be to pull tethers. To quantify MCA, tethers are extruded from the same cell at different speeds and the force-velocity curves are fitted with the Brochard-Wyart et al. mathematical model (figure 1.8D) (Brochard-Wyart et al., 2006):

$$f - f f_0 \cong aV$$

where *f* is the tether force at retraction speed (V), and a is a measure of the slope of the curve. The parameter a is formed of different components:

$$a \cong (2\pi)^3 2B^2 \upsilon \eta_e \ln\left(\frac{R}{r_t}\right)$$

where the bending rigidity (*B*), cell radius (*R*) and tether radius(r_t) are assumed to be constant at different retraction speeds. The surface viscosity (η_e) increases as retraction speed increases and the product ($\nu\eta_e$) (where ν is the density of MCA linkers) provides an estimate of MCA.

In summary, MCA has been shown to contribute to the PM tension and to the cell surface viscosity. However, these discoveries have been made mainly just to explain the outcome tether pulling experiments rather than investigate the precise role of MCA in cell surface mechanics. In fact a lot of questions have yet to be answered, in particular: *how MCA contribute to cell cortex mechanics?*, and *are current mechanical models at the cell surface complete or should MCA be included?*

1.3. Biological functions of cell mechanics

The scientific interest in the cell surface mechanics has been constantly growing in the past three decades, owing to the tremendous amount of findings that show their role in key biological processes. Indeed, cell mechanics are not only passive physical constrains, but are actively exploited and regulated by the cell to exert specific biological functions.

All the cell surface mechanics influence each other and, at different degrees, participate into the regulation of a biological process. Nevertheless, their complexity and methodological limitations have forced biologists to focus on individual mechanical properties. In this context, cortical tension and apparent PM tension have been by far the two most explored mechanics.

A comprehensive description all the mechanically-regulated cellular processes is beyond the scope of this thesis. In the following sections I will discuss only two of them, as exemplary case studies.

1.3.1. Case study (I): cortex mechanics in cell shape acquisition and cell division

Cortical tension has been shown to be the primary regulator of cell shape (reviewed in (Chalut & Paluch, 2016)). This is particularly clear during mitosis of adherent cells, which is characterized by massive and stereotyped changes in tension-driven shape (reviewed in (Ramkumar & Baum, 2016) (Taubenberger et al., 2020)). At the onset of mitosis (prophase), cells reduce the strength of adhesion to the substrate by disassembling focal adhesions and replacing them with much weaker contact points (Dix et al., 2018). Concomitant changes in cortex mechanics drive cell rounding: a global and large increase in cortical tension (~8-fold in HeLa cells) drives a similarly large increase in intracellular pressure (~10 fold in HeLa cells) (Fischer-Friedrich et al., 2016). Intracellular

pressure pushes against the cell surface in an isotropic fashion forcing cells to acquire a spherical shape (figure 1.9). Many works suggested that cell rounding is required to create sufficient space for the formation of the mitotic spindle (Dumont & Mitchison, 2009) (Lancaster et al., 2013).

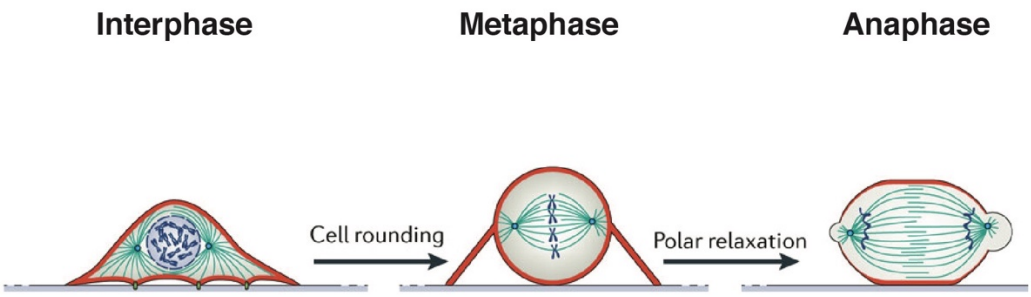

Figure 1.9. Schematic of cell shape changes during the cell cycle. Modified from (Ramkumar & Baum, 2016).

Upon completion of metaphase and consequent entry into anaphase, cells elongate in order to start building the two daughter cells (reviewed in (Ramkumar & Baum, 2016)). This shape change is once again governed by cortex mechanics: at the poles, the cortex relaxes whereas at the mitotic plane the cortex stiffens up and forms a contractile actomyosin ring; contraction of ring finally drive cytokinesis (Turlier et al., 2014).

The role of the cortex in cell division is not limited to the control of cell shape but it extends to the regulation of the orientation of the mitotic spindle, even though the molecular and biophysical mechanisms have not been fully elucidated (reviewed in (van Leen et al., 2020)). First of all, the cortex serves as a pivot for the generation of force that propagates along the spindle: Dynein, a microtubular motor, localizes at the poles of the cell where it crosslinks the cortical actin to the microtubules of the aster and generates the tensile force responsible for the orientation of the spindle (Nguyen-Ngoc et al., 2007). Second, and most importantly, localized experimentally-induced changes in cortical tension have been shown to re-orient the spindle, in accordance with the

hypothesis of a cortex contractility-regulated determination of the division plane position (Scarpa et al., 2018). The importance of this phenomenon *in vivo* has been already shown in mouse embryo. According to a series of groundbreaking studies, anisotropic cortical tension controls asymmetric divisions that are responsible for the first fate specification event during the mouse embryo development (Maître et al., 2015) (Maître et al., 2016) (Korotkevich et al., 2017).

1.3.2. Case study (II): cell surface mechanics in cell protrusion formation

Cell protrusions are dynamic deformations of the PM actively formed by cells to exert different functions, ranging from migration to spreading (reviewed in (Blanchoin et al., 2014)). Being a special case of cell shape remodeling, a massive involvement of cell surface mechanics is not surprising, and notably, different mechanical properties are engaged in the formation of different protrusions. In this respect, lamellipodia and blebs can be considered as two opposite sides of the same coin: the former are large and flat extensions of the PM driven by actin polymerization and antagonized by in-plane tension, whereas blebs are intracellular pressure-driven spherical protrusions promoted by high cortical tension and low MCA (reviewed in (Keren & Shemesh, 2017) (G. Charras & Paluch, 2008)). Many cell types (*e.g.* keratinocytes and neutrophils) use lamellipodia to crawl on substrates. Migratory stimuli induce localized activation of Arp2/3 complex and the consequent branching of filamentous Actin (figure 1.10).

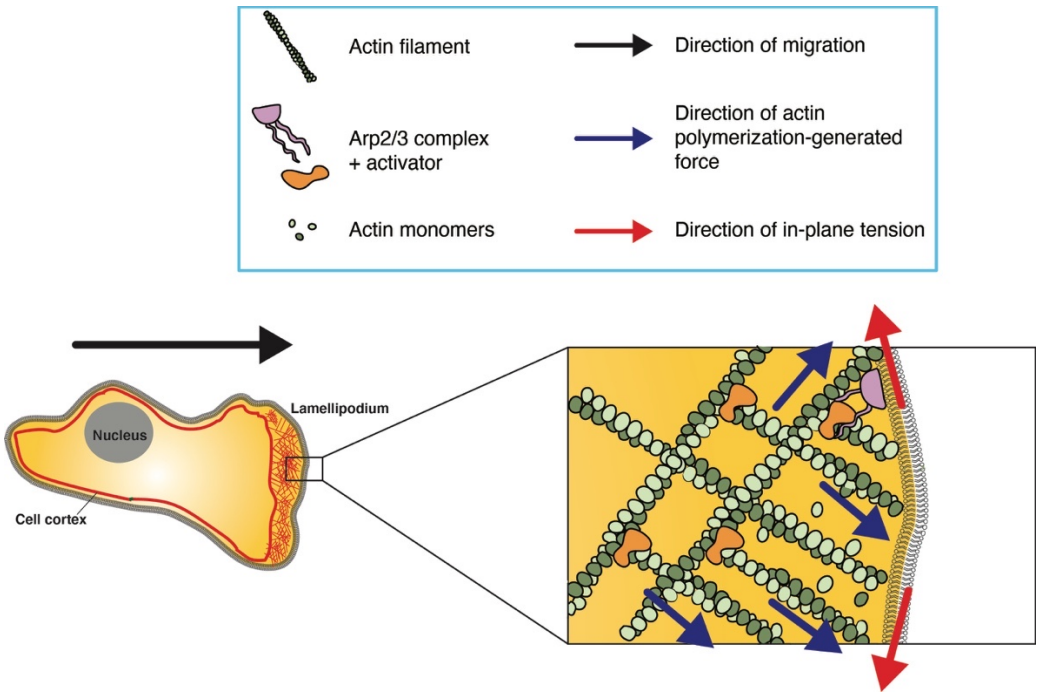

Figure 1.10. Schematic of lamellipodium formation. The inset on the right shows how Arp2/3-dependent actin polymerization pushes against the PM which resists expansion by increasing in-plane tension.

Actin polymerization, in turn, generates a tensile force against the PM which leads to the extrusion of a lamellipodium (figure 1.10, inset). Importantly, the initial expansion of the protrusion is facilitated by the unfolding ruffles of the PM. Upon maximization of the apparent surface area, further growth of the lamellipodium requires expansion of the PM which is opposed by an increasing in-plane tension (figure 1.10, inset) (Raucher & Sheetz, 1999). Aside from limiting the size of the lamellipodium, this tension increase favors the directionality of this mode of migration by inhibiting the formation of secondary lamellipodia in other domains of the cell surface (Houk et al., 2012). This is achieved by lipid flows that rapidly re-equilibrate in-plane tension. High values in this mechanical property, as well the exhaustion of membrane reservoirs, physically impede the initiation of other lamellipodia (Batchelder et al., 2011) (Houk et al., 2012).

Blebs are protrusions observed in different processes ranging from apoptosis, to cytokinesis, to ameboid migration (reviewed in (Charras, 2008)).

Their dynamics can be subdivided in four phases: initiation, expansion, cortex re-growth and reabsorption (figure 1.11) (reviewed in (G. Charras & Paluch, 2008)).

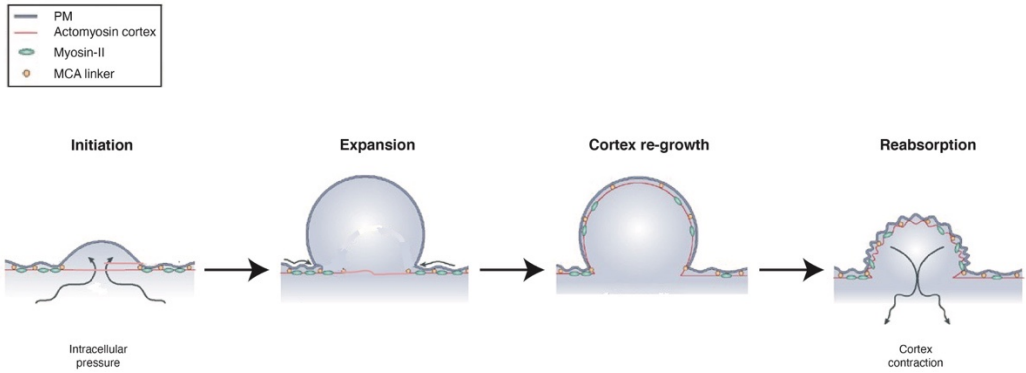

Figure 1.11. Schematic of bleb dynamics. Modified from (G. Charras & Paluch, 2008).

The first two steps are driven by intracellular pressure that pushes against the PM causing its local detachment from the cortex (figure 1.10B). Similarly to lamellipodia, the bleb keeps expanding until the intracellular pressure balanced by the increase in in-plane tension (Goudarzi et al., 2017). Subsequently, the cortex starts growing inside the spherical protrusion and, once fully formed and linked to the PM, cortical tension drives bleb reabsorption. Bleb extrusion is governed by two mechanical properties: cortex contractility and MCA. As discussed in section *1.2.2.2.*, myosin-II-mediated cortex contractions cause localized transient spikes of intracellular hydrostatic pressure, which in turn can directly induce bleb formation (Bergert et al., 2012). On the other side, localized weakening of MCA reduces the threshold pressure required to detach the PM from the cortex. Several studies have shown the importance of MCA in the formation of blebs and hence migration. Notably, Ezrin is one of the first proteins to be recruited to the bleb at the end of the expansion phase, and its ability to link the newly formed cortex to the PM is indispensable for bleb retraction (Guillaume T. Charras et al., 2006). Furthermore, the activity of the MCA linkers has been shown to determine the mode of motions of cells *in vivo*. During

Zebrafish gastrulation, mesendoderm progenitor cells migrate using lamellipodia to move straight and blebs to reorient and change direction (Kane & Adams, 2002). The degree of activity of MCA linkers dictates the migration mode and the ability of cells to establish a trajectory of migration: if MCA is too high, cells fail to bleb, on the other side, very low MCA leads to over-blebbing. In both scenarios cells fail to modulate their directionality and reach their targets (Diz-Muñoz et al., 2010) (Diz-Muñoz et al., 2016).

2. Aims of the thesis

The target of study of this thesis is Membrane-to-Cortex attachment (MCA). A great obstacle in studying MCA has so far been the lack of methods to specifically perturb MCA in cells. Indeed, all the methods that were available prior to my work affected also other mechanical properties and the signaling status of the cell. To overcome this limitation and to shed light on the biophysics and on the biological relevance of MCA, I developed a molecular tool to specifically and exclusively modulate MCA. After achieving this goal, we focused on showing the regulatory role of MCA in cellular processes influenced by cell surface mechanics. In parallel, we used the tool also to understand how MCA influences and contribute to other mechanical properties of the cell surface.

At a glance, my work can be subdivided in three parts which correspond to the three chapters of the results section of this thesis. In part A of the results (section *3.1.*), I describe how we engineered an artificial MCA linker, named iMC linker. To the best of our knowledge, iMC linker is the most precise tool to perturb exclusively MCA in cell model systems. In part B (section *3.2.*), I discuss our findings on a novel function of MCA in regulating mouse embryonic stem cells differentiation. Finally, as described in part C of the results (section *3.3.*), I

describe our breakthrough finding that iMC linker-mediated increase in MCA leads to softening of the cell cortex. Understanding how the mechanical properties of the cell cortex are regulated is of primary importance owing to the biological implications in cell homeostasis and activity. In this ongoing work we aim at characterizing the influence of MCA on cortex mechanics, in particular in regard to the molecular and biophysical mechanisms underlying this phenomenon.

3. Results and discussion

3.1. PART A: development of a signaling inert MCA linker

Membrane-to-Cortex attachment (MCA) is arguably the most elusive element of the animal cell surface. As discussed in section *1.1.3.*, not all the MCA linkers have been identified, nor the has role of non-specific interactions between the cortex and the Plasma Membrane (PM) been assessed *in cellulo*. Furthermore, the contribution of MCA to the cell surface mechanics is non-trivial and method-dependent (section *1.2.3.*).

The lack of proper perturbation procedures is a major obstacle to studying MCA. In various life science disciplines – including cell mechanics – a classic approach used to examine a biological process is to experimentally disturb it. The phenomenon of interest needs to be targeted with high specificity, aiming at minimizing confounding effects that may arise by unwanted perturbations of other biological processes. Regrettably, all the currently available perturbation

procedures for MCA fail at being specific. For instance, drug-mediated depolymerization of the cortex does abolish MCA, however, it also impairs other mechanics of the cell, owing to the loss of the actin cytoskeleton (figure 3.1A) (reviewed in (Braet et al., 2008)).

A reduction in the density of active MCA linkers at the cell surface does also lead to a reduction in MCA. This can be in principle achieved with a quick increase in the PM surface area via cell stretching or hypo-osmotic shock (figure 3.1B, C) (reviewed in (Gardel & Oakes, 2015) (Kamble et al., 2016)). Both methods provoke an almost instantaneous unfolding of membrane ruffles and other sources of membrane reservoir; in some cell types up to a three-fold increase in the effective surface area it can be obtained (Groulx et al., 2006). However, similarly to cortex depolymerization, these methods perturb various cell mechanics, including in-plane PM tension (Batchelder et al., 2011). Furthermore, cells compensate for the reduction of linker density by activating inactive linkers through the post-translational modifications (Tamma et al., 2007) (Rasmussen et al., 2008).

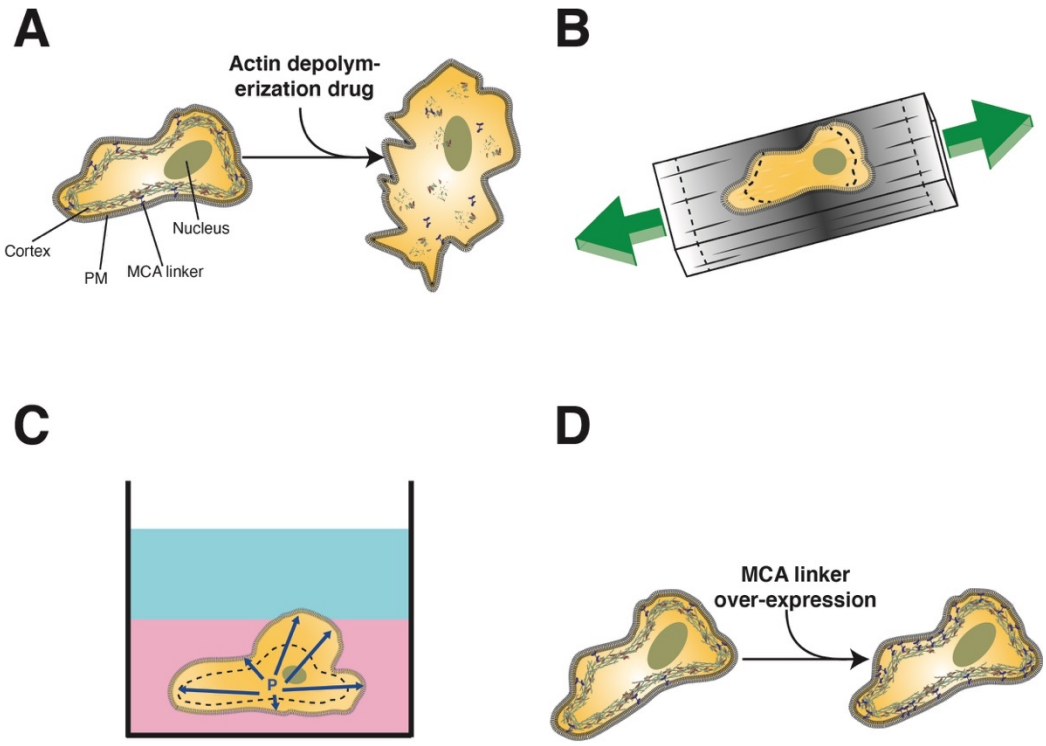

Figure 3.1. MCA perturbation methods currently available.
(A) Drug-mediated cortex depolymerization.
(B) Cell stretching device. Green arrows: deformation direction. Dashed lines: original cell shape and size.
(C) hypoosmotic shock. P: intracellular pressure. Dashed lines: cell size at isotonic conditions.
(D) Over-expression of endogenous linkers.

Genetic approaches are the current gold standard to modify MCA. Specifically, ectopic expression of dominant negative versions of ERM proteins or downregulation of endogenous linkers lead to a reduction in MCA degree (Fukata et al., 1999) (Zhang et al., 2020) (Kunda et al., 2008) (Nambiar et al., 2009) (Rouven Brückner et al., 2015); conversely, ectopic expression of constitutively active versions of ERM proteins leads to the opposite effect (figure 3.1D) (Yin Liu et al., 2012) (Stefani et al., 2017) (Zhang et al., 2020). Notwithstanding the wide use, these tools are far from being precise in tuning specifically MCA. Indeed, all the know endogenous linkers exert also other functions, ranging from the direct contribution of cortical tension of Myo-I(s) to the role as signaling intermediates of ERM proteins (Jianwu Dai et al., 1999)

(reviewed in (Fehon et al., 2010) (Ponuwei, 2016)). For example, Ezrin has been shown to inhibit Arp2/3 complex-mediated actin polymerization by sequestering its regulator N-WASP (Manchanda et al., 2005). Henceforth, overexpression of a constitutively active version of Ezrin would not only increase MCA, but would also indirectly perturb, among others, cortex mechanics.

All the conceptual and methodological limitations illustrated in the previous paragraphs are a big obstacle to studying MCA. Consequently – since overall goal of this thesis is to shed light on this component of cell surface mechanics – I devoted the first part of my PhD to the development of a clean tool to effectively and specifically perturb MCA. In general terms, this tool is an artificial MCA linker able to increase MCA without of affecting any other cellular processes, in particular signaling.

3.1.1. Artificial signaling-inert linker design and candidate domains selection

The artificial signaling-inert MCA linker (henceforth simply artificial linker) has been devised to conceptually resemble an archetypical endogenous MCA linker (figure 3.2 top). It consists of a single polypeptide chain which folds into a PM-binding and an actin-binding domains separated by a hinge region (figure 3.2 bottom). Upon expression, the linker simultaneously binds the PM and filamentous actin and thus tethers the former structure to the cell cortex, that is, it increases MCA.

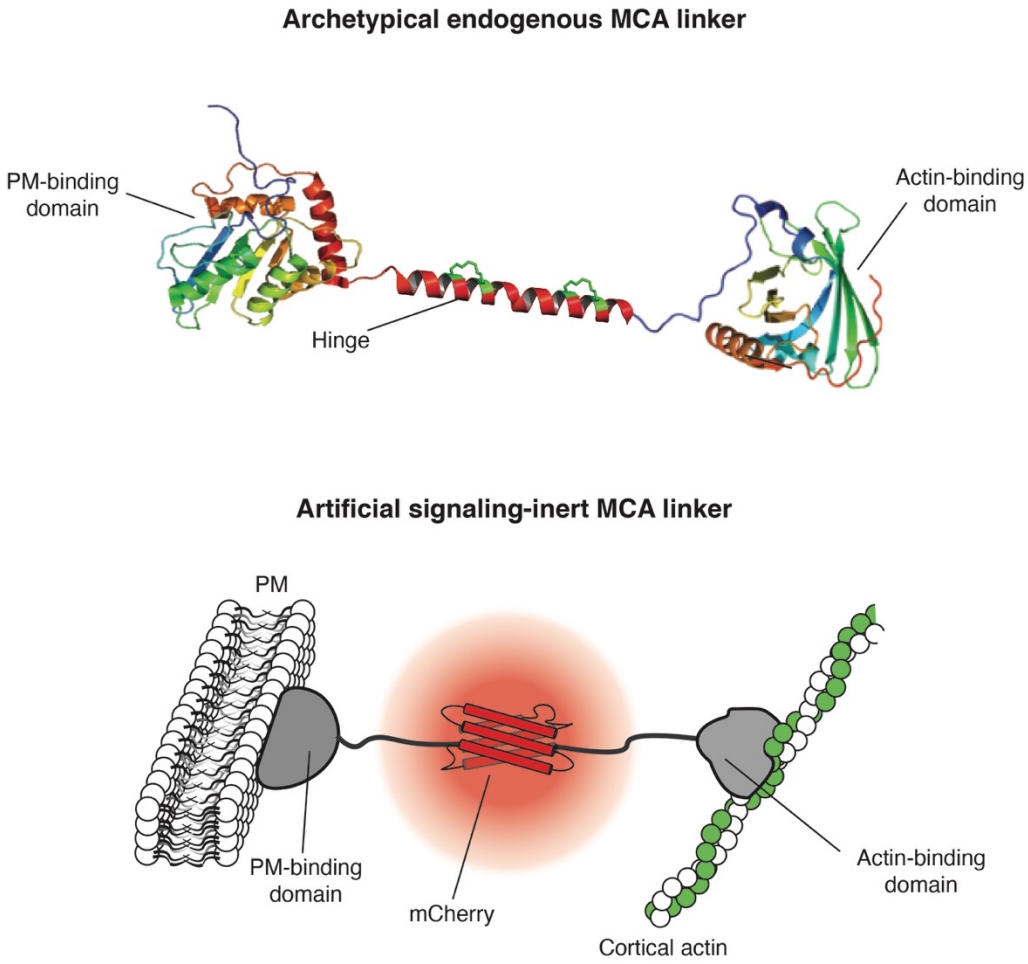

Figure 3.2. Outlines of an archetypical endogenous MCA linker (top) and the artificial signaling inert MCA linker (bottom).

The hinge contains a fluorophore for assessing expression and subcellular localization of the linker. mCherry has be chosen because in cell it exists only in a monomeric form (Shaner et al., 2004). Avoiding oligomerization of the artificial linker is indeed critical, since multimeric complexes would contain multiple actin-binding domains, and hence, would act also as actin crosslinkers.

The selection of an appropriate combination of PM-binding and actin-binding domains is the most critical element to be considered when engineering an effective artificial linker. Four requirements need to be satisfied:

1. The two domains must bind their respective targets with high specificity;

2. The dynamics of the PM and the cortex should be only minorly disturbed upon linker binding;
3. Signaling-inertia of the linker needs to be granted by choosing domains which do not interfere with the signaling status of the cell by interacting with signaling intermediates;
4. The combination of the binding kinetics of the two domains should suit the requisites needed to increase MCA upon the expression of the linker.

The identification of domains with these distinctive characteristics has been accomplished by following a candidate screening approach. Upon extensive literature search, numerous candidates have been chosen (tables 3.1, 3.2). Importantly, we have assured to include domains with different biochemical features, in particular a wide range of constants of dissociation (K_D) for the actin binding domains, and different binding specificities for the PM-binding ones.

Table 3.1. Candidate PM-binding domains chosen to engineer artificial linkers. Y: specific subcellular localization to the cell surface. N: incorrect subcellular localization.

Domain /motif	Protein	UniProtKB entry No.	Binding specificity	Reference	Subcell. localization
PH	hAKT1	P31749	PI(3,4,5)P3	(Carpten et al., 2007)	N
PH	hPLCΔ1	P51178	PI(4,5)P2	(Essen et al., 1997)	Y
PH	hAnillin	Q9NQW6	PI(4,5)P2	(Oegema et al., 2000)	N
PX	hTCGAP	O14559	PI(4,5)P2	(Chiang, 2003)	N
PX	hPI3K-C2γ	O75747	PI(4,5)P2	(Domin et al., 2000)	N
Atypical C1	MgcRacGAP	Q9H0H5	PI(3,4,5)P3, PI(4,5)P2	(Lekomtsev et al., 2012)	N
C1	hPKCα	P17252	DAG; PE	(Ling et al., 2007)	Y
C2	hPKCα	P17252	PI(4,5)P2	(Landgraf et al., 2008)	N
FERM	hEzrin	P15311	PI(4,5)P2	(Bretscher et al., 2002)	Y
FERM	hMoesin	P26038	PI(4,5)P2	(Pearson et al., 2000)	Y
TH1	hMyo1C	O00159	PI(4,5)P2	(Hokanson et al., 2006)	N
TUBBY	mTubby	P50586	PI(4,5)P2	(Carroll et al., 2004)	N
TMD	Stargazin	O88602	Transmembrane protein	(Wagner & Glotzer, 2016)	Y
TMD	hIL2Rα	P01589	Transmembrane protein	(Minami et al., 1993)	Y
Lyn motif	hLyn kinase	P07948	Myristoylation, Palmitoylation and insertion	(Kovářová et al., 2001)	Y

			into the lipid bilayer		
CAAX motif	hkRas	P01116	Prenylation and insertion into the lipid bilayer	(Gao et al., 2009)	Y

Table 3.2. Candidate actin-binding domains chosen to engineer artificial linkers. Y: specific decoration of actin filaments. N: incorrect subcellular localization.

Domain/motif	Protein	UniProtKB entry No.	Reference	Subcell. localization
CHCH	hFilamin A	P21333	(Ruskamo & Ylänne, 2009)	Y
CHCH	hα-Actinin	P12814	(Borrego-Diaz et al., 2006)	N
CHCH	hUtrophin	P46939	(Keep et al., 1999)	Y
Actin binding domain	hAnillin	Q9NQW6	(Field & Alberts, 1995)	N
Lifeact	Abp140	Q08641	(Riedl et al., 2008)	Y
Actin binding domain	hEzrin	P15311	(Turunen et al., 1994)	Y
Actin binding domain	hMoesin	P26038	(Pestonjamasp et al., 1995)	Y
Actin binding domain	hAbl1	P00519	(Van Etten, 1994)	N
VHP	hVillin	P09327	(Vardar et al., 2002)	N
HP	hDematin	Q08495	(Vardar et al., 2002)	N

An initial evaluation of the candidates listed in table 3.1 and 3.2. has been conducted by expressing fluorescently-tagged variants of each domain *in cellulo*. The subcellular localization of the constructs has been used as a proxy for assessing binding specificity (figures 3.3, 3.4): the domains that in our hands

correctly and exclusively localize at the cell surface have been shortlisted and used for the subsequent generation and screening of candidate artificial linkers.

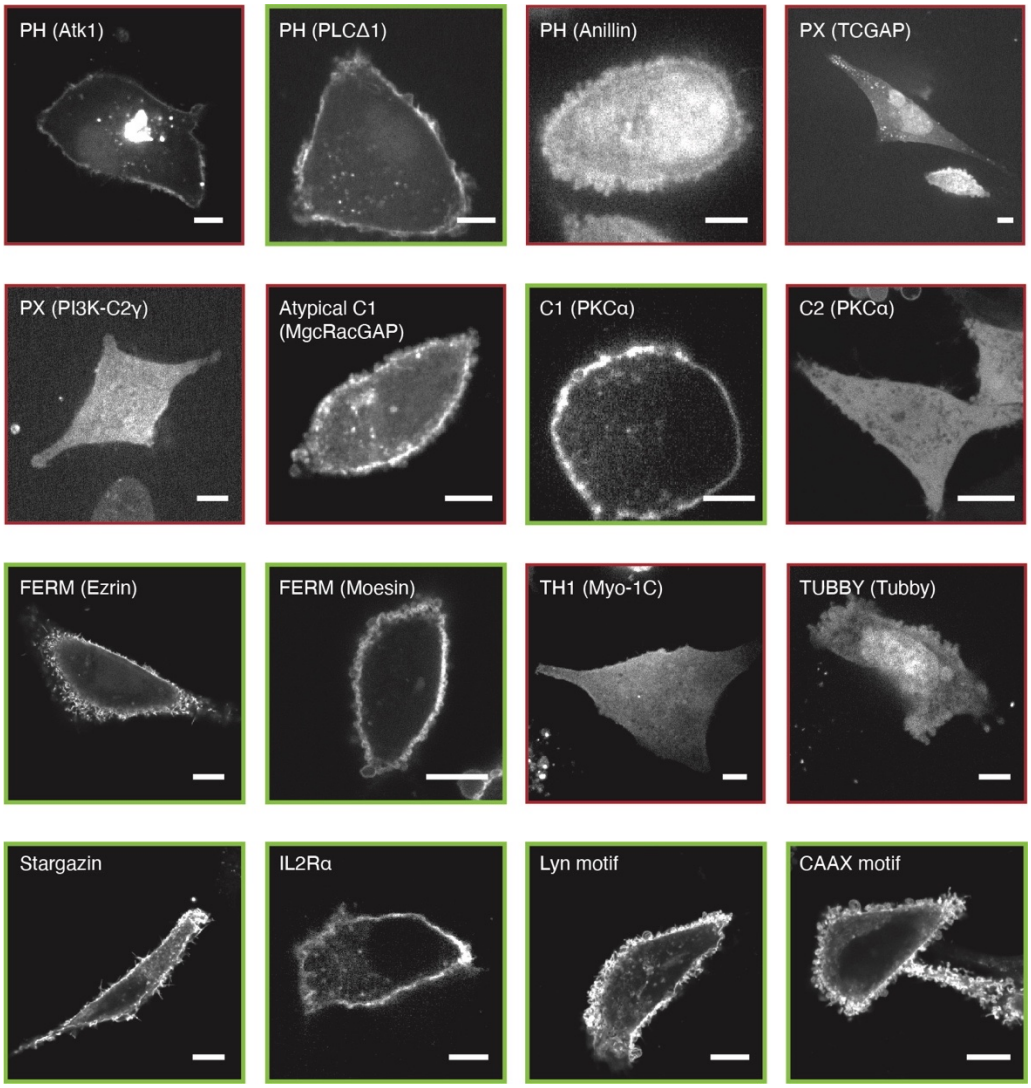

Figure 3.3. Subcellular localization of PM-binding listed in table 3.1. Representative images of A549 cells transiently expressing candidate PM-binding domains tagged with mCherry. Cells were fixed prior imaging with spinning disk confocal microscopy. Scale bar: 10 µm. Domains were shortlisted based on their exclusive localization at the cell surface. Green squares: shortlisted domains. Red squares: discarded domains. Scale bar: 10 µm.

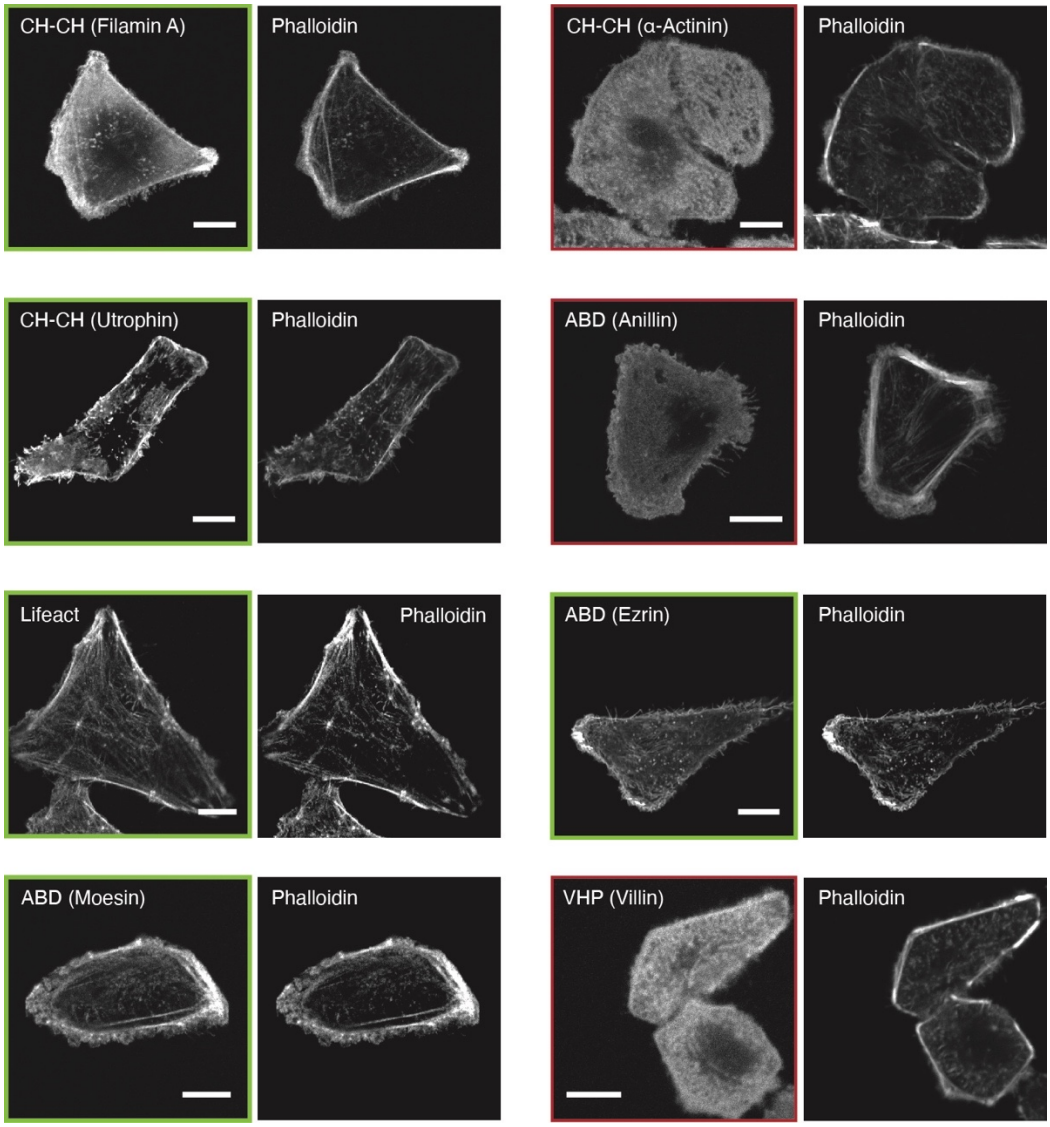

Figure 3.4. Subcellular localization of actin-binding domains listed in table 3.2. Representative images of A549 cells transiently expressing candidate actin-binding domains tagged with eGFP. Cells were fixed, stained with Phalloidin and imaged with spinning disk confocal microscopy. Domains were shortlisted based on their exclusive decoration of actin filaments (*i.e.* colocalization with Phalloidin). Green squares: shortlisted domains. Red squares: discarded domains. Scale bar: 10 µm.

3.1.2. Development of a platform to screen candidate artificial linkers

The cleanest way to assess the ability of candidate artificial linkers to increase MCA would be to biophysically measure their contribution to effective

PM tension or surface viscosity. The former can be measured by pulling static tethers with Atomic Force Spectroscopy (AFS) or optical tweezers, whereas the latter by pulling dynamic tethers with AFS (see section *1.2.3*). Regrettably, both techniques are rather low throughput and hence are not suitable for screening purposes. To overcome this limitation, we have developed an artificial linker screening platform. The method exploits bleb protrusion formation, a MCA-regulated biological process. As discussed in section *1.3.2.*, blebs are intracellular pressure-driven cell protrusions that arise from the detachment of the PM from the cortex. By increasing the adhesion energy between these two structures (*i.e.* MCA), a functional artificial linker should be able to inhibit bleb formation in constitutively blebbing cells (figure 3.5).

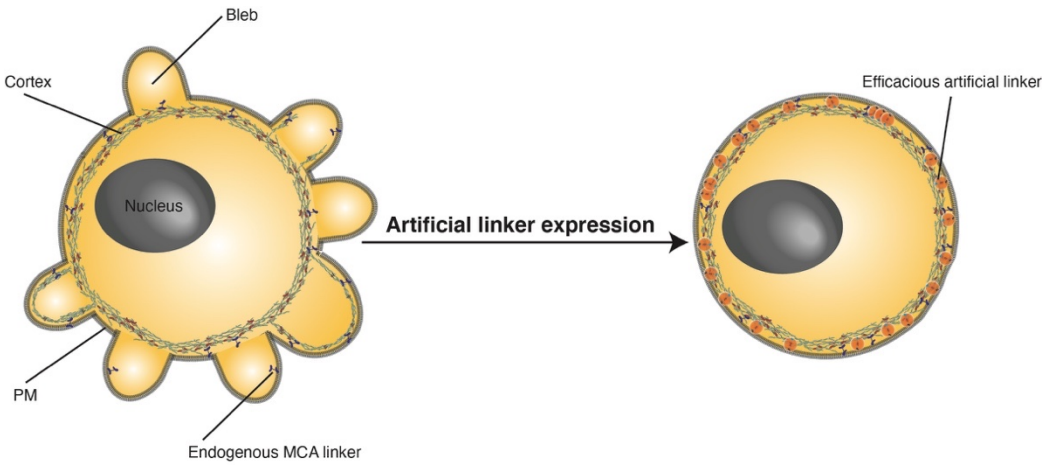

Figure 3.5. Schematic of blebbing inhibition achieved by expressing an effective artificial linker.

A549 human alveolar carcinoma cell line has been chosen as model system to screen the candidate artificial linkers (figure 3.6A) (Lieber et al., 1976). Cells display extensive blebbing upon detachment from the substrate and subsequent seeding on a culture plate (figure 3.6B); this behavior has been observed in different cell lines and has been hypothesized to assist and promote cell spreading (Erickson & Trinkaus, 1976) (Bereiter-Hahn et al., 1990). Aiming to regiment this cellular process, we confined A549 cells between a layer of agarose

and the non-adhesive surface of a glass-bottomed plate (figure 3.6C) (see procedures for further details). This setup introduced two major improvements: (i) it stereotyped and enhanced blebbing, since 100% of cells form large protrusions from 0 h to 24 h after confinement; (ii) blebs can be extruded only laterally, hence can be positioned in the same focal plane for better imaging (figure 3.6D).

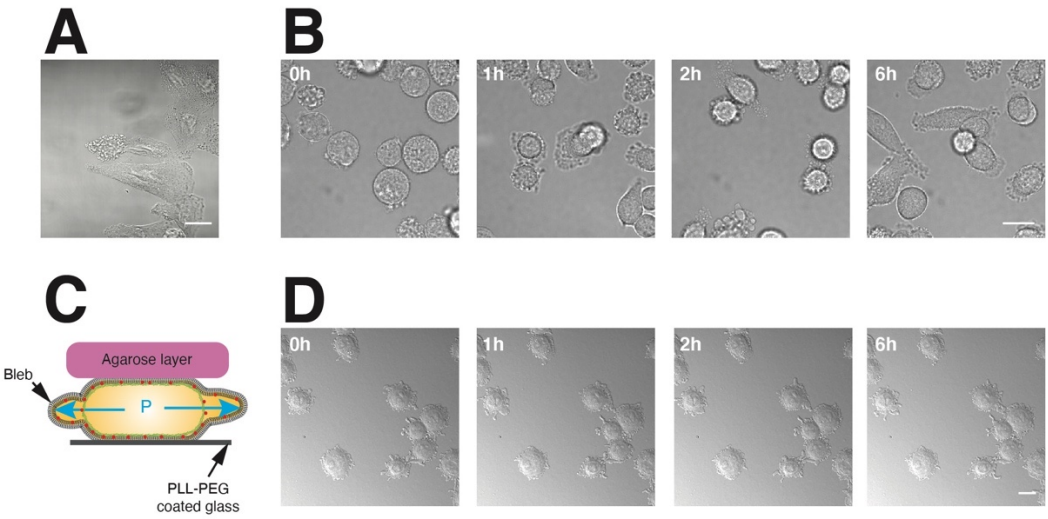

Figure 3.6. A549 cells blebbing behavior during adhesion and upon confinement.
(A) Representative bright field image of fully adherent A59 cells.
(B) Representative time-lapse bright field images of A549 cells during adhesion. Blebbing behavior is highly variable: some cells start blebbing at later time points, some cells fully spread at earlier time points, and some cells do not bleb at all.
(C) Schematic of a blebbing A549 cells confined between a layer of agarose and a PLL-g-PEG coated surface. P: intracellular pressure.
(D) Representative time-lapse DIC images of blebbing A549 cells confined as shown in C. All the cells display extensive and stereotyped blebbing. (A-B-D) Scale bar = 20 µm.

Aiming to test the artificial linker screening platform, we analyzed A549 cell constitutively expressing CAezrin-mCherry (a constitutively active version of an endogenous MCA linker, T567D (Gautreau et al., 2000)), or mCherry; they are a positive and a negative controls respectively (figure 3.7). We evaluated the blebbing behavior in a semi-quantitative fashion by classifying the cells in three

categories groups: extensively blebbing (the stereotyped behavior of confined A549 cell); reduced blebbing (cell that form smaller blebs and at lower frequency); and cells in which blebbing is fully inhibited (figure 3.7A). By using fluorescence intensity as a proxy for protein expression (see procedures for further details), we found that CAezrin suppresses bleb formation in an expression level-dependent manner (figure 3.7B,C). Blebbing inhibition is not caused by the over-expression *per se* of an exogenous protein (figure 3.7D,E). These results strongly support the employment of our screening platform to evaluate the ability of ectopically expressed candidate artificial linkers to increase MCA.

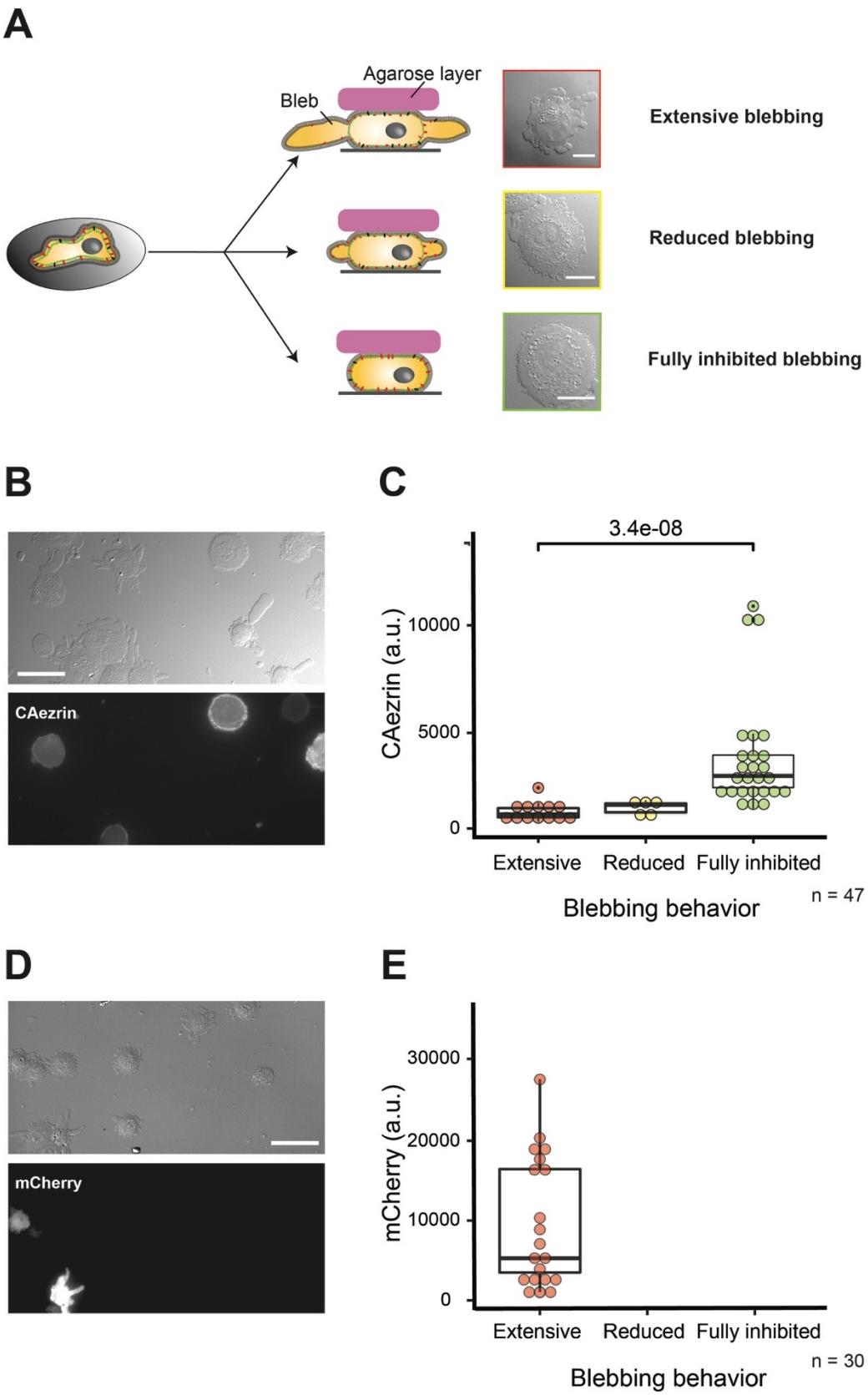

Figure 3.7. Validation of the MCA artificial linker screening platform.

(A) Description of the states chosen to classify A549 blebbing behavior upon confinement. Scale bar: 20 µm.
(B) Representative time point of time-lapse DIC images (top) and epifluorescence images (bottom) of confined A549 cells constitutively expressing CAezrin-mCherry. Scale bar: 50 µm.
(C) Semi-quantitative analysis of the blebbing behavior of confined A549 in relation to the expression level of CAezrin-mCherry. Cells have been classified into the categories described in A. Mean epifluorescence intensity used as a proxy to quantify expression level. Dots: single cells; a.u.: arbitrary units. n: number of cells analyzed in 3 independent experiments. p-value: Mann-Whitney U-test.
(D) Representative time point of time-lapse DIC images (top) and epifluorescence images (bottom) of confined A549 cells constitutively expressing mCherry. Scale bar: 50 µm. (E) Semi-quantitative analysis of the blebbing behavior of confined A549 in relation to the expression level of mCherry. Cells have been classified into the categories described in A. Mean epifluorescence intensity used as a proxy to quantify expression level. Gray dots: single cells.; a.u.: arbitrary units. n: number of cells analyzed in 2 independent experiments.

3.1.3. Identification of effective artificial linkers

Candidate artificial linkers (table 3.3) were engineered by combining each shortlisted PM-binding domain to each shortlisted actin-binding domain (see section *3.1.1.*). Importantly, the arrangement of the two domains was decided by taking into account their position in the source proteins. For instance, CAAX was always placed at the C-terminal of an artificial linker since otherwise it cannot be lapidated and inserted into the PM (reviewed in (Gao et al., 2009)).

Table 3.3. Candidate signaling-inert artificial linkers. *: N-terminal domain. E: efficient blebbing inhibition. N: non-effective candidate linker. F: screening failure (mainly caused by linker cytotoxicity). mCherry omitted from the description of the composition of the candidate artificial linkers for clarity.

PM-binding domain (donor protein)	Actin-binding domain (donor protein)	Screening outcome
PH domain (hPLCΔ1)*	CHCH (hFilamin A)	N
PH domain (hPLCΔ1)*	CHCH (hUtrophin A)	F
PH domain (hPLCΔ1)	Lifeact*	F

PH domain (hPLCΔ1)*	ABD (hEzrin)	N
PH domain (hPLCΔ1)*	ABD (hMoesin)	N
Atypical C1 (MgcRacGAP)*	CHCH (hFilamin A)	N
Atypical C1 (MgcRacGAP)*	CHCH (hUtrophin A)	N
Atypical C1 (MgcRacGAP)	Lifeact*	N
Atypical C1 (MgcRacGAP)*	ABD (hEzrin)	N
Atypical C1 (MgcRacGAP)*	ABD (hMoesin)	N
C1 (hPKCα)*	CHCH (hFilamin A)	N
C1 (hPKCα)*	CHCH (hUtrophin A)	N
C1 (hPKCα)	Lifeact*	N
C1 (hPKCα)*	ABD (hEzrin)	N
C1 (hPKCα)*	ABD (hMoesin)	N
FERM (hEzrin)*	CHCH (hFilamin A)	N
FERM (hEzrin)*	CHCH (hUtrophin A)	E
FERM (hEzrin)*	Lifeact	F
FERM (hMoesin)*	CHCH (hFilamin A)	N
FERM (hMoesin)*	CHCH (hUtrophin A)	F
FERM (hMoesin)*	Lifeact	N
Stargazin*	CHCH (hFilamin A)	N
Stargazin*	CHCH (hUtrophin A)	N
Stargazin	Lifeact*	N
Stargazin*	ABD (hEzrin)	N
Stargazin*	ABD (hMoesin)	N
IL2Rα*	CHCH (hFilamin A)	N
IL2Rα*	CHCH (hUtrophin A)	N
IL2Rα	Lifeact*	N
IL2Rα*	ABD (hEzrin)	N
IL2Rα*	ABD (hMoesin)	N
Lyn motif (hLyn kinase)*	CHCH (hFilamin A)	N

Lyn motif (hLyn kinase)*	CHCH (hUtrophin A)	E
Lyn motif (hLyn kinase)*	Lifeact	E
Lyn motif (hLyn kinase)*	ABD (hEzrin)	E
Lyn motif (hLyn kinase)*	ABD (hMoesin)	N
CAAX motif (hkRas)	CHCH (hFilamin A)*	N
CAAX motif (hkRas)	CHCH (hUtrophin A)*	F
CAAX motif (hkRas)	Lifeact*	F
CAAX motif (hkRas)	ABD (hEzrin)*	N
CAAX motif (hkRas)	ABD (hMoesin)*	N

A549 cells constitutively expressing the candidate artificial linkers were generated, amplified and each cell line was screened multiple times using the platform described in section *3.1.2*. A summary of the outcome of these multiple screening rounds is depicted in the right-most column of table 3.3. Four different candidate linkers were shown inhibit blebbing in an expression level-dependent manner (figure 3.8).

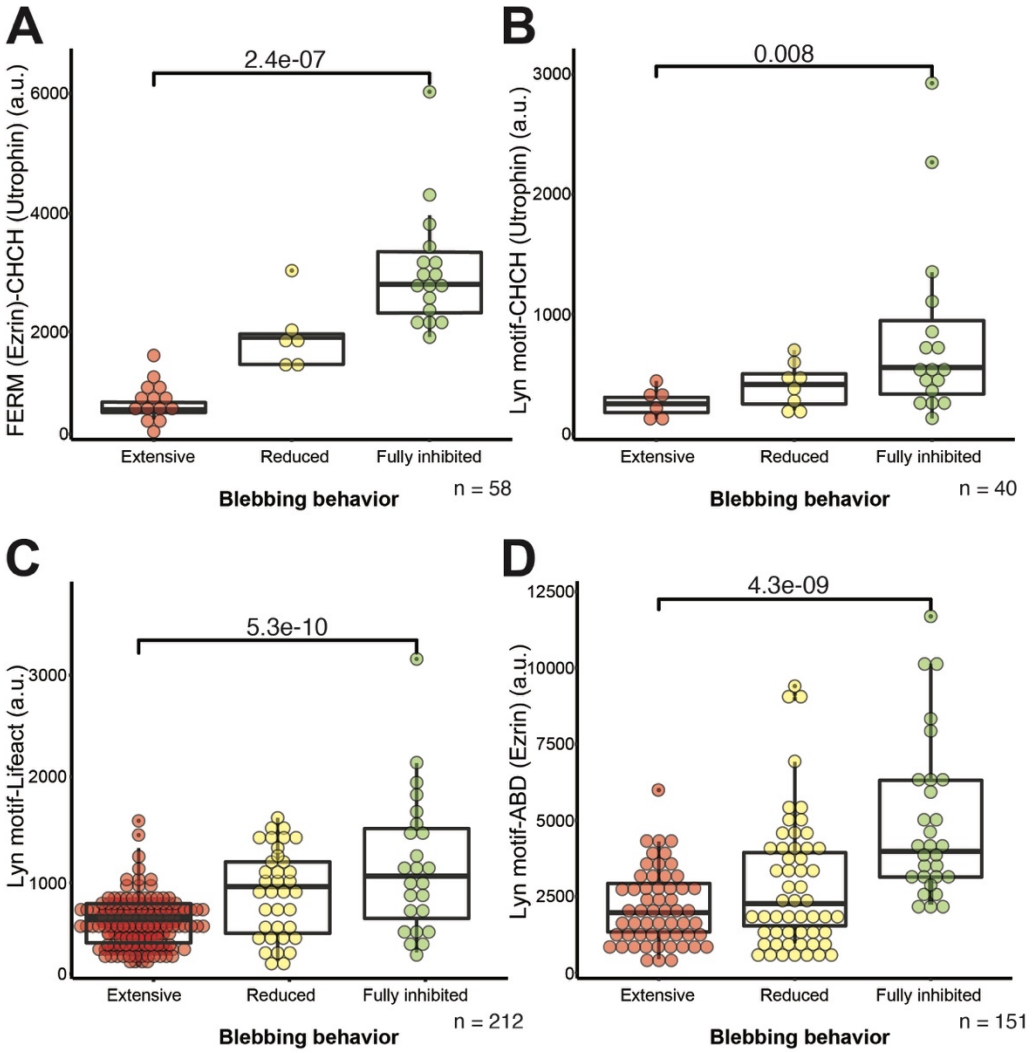

Figure 3.8. Identification of effective artificial linkers. Semi-quantitative analysis of the blebbing behavior of confined A549 in relation to the expression level of effective candidate artificial linkers. Cells have been classified into the categories described in figure 3.7A. mCherry omitted from the designation of the linkers for clarity. Mean epifluorescence intensity of mCherry used as a proxy to quantify expression level. Dots: single cells, a.u.: arbitrary units. n: number of cells analyzed in 3 independent experiments. p-value: Mann-Whitney U-test.

Signaling inertia is a fundamental property of an artificial linker (see section 3.1.1.). In this respect, the four linkers that effectively elicit blebbing inhibition (table 3.3 and figure 3.8) are not equivalent. The effective linkers that contain domains from Ezrin, namely FERM(Ezrin)-mCherry-CHCH(Utr) and namely Lyn motif-mCherry-ABD(Ezrin), are more prone to interact with signaling molecules (reviewed in (Fehon et al., 2010)). Conversely, Lyn motif-mCherry-

CHCH(Utrophin) and Lyn motif-mCherry-Lifeact are – to the best of our knowledge – signaling-inert. Nevertheless, lifeact has been shown to interfere with actin dynamics and to create artifacts when expressed at high levels (Flores et al., 2019). Consequently, we chose Lyn motif--mCherry-CHCH(Utr) as reliable tool to further investigate MCA throughout the rest of this thesis. We rebranded this effective artificial linker as **iMC linker**.

3.1.4. Biophysical validation of the screened signaling-inert artificial MCA linkers

The screening platform described above uses blebbing inhibition as readout to infer the ability of artificial linkers to increase MCA. Notwithstanding, causality between artificial linker expression and inhibition of bleb formation might be more convoluted than expected. The screened artificial linkers might indeed elicit blebbing inhibition through mechanisms different from MCA increase. For instance – albeit unlikely since not supported by literature – if the artificial linkers were able to reduce cortical tension, bleb protrusion formation would also be prevented, owing to the drop in intracellular pressure (see section *1.3.2*).

To evaluate directly whether the screened artificial linkers do increase MCA, we measured the mechanical properties of the cell surface influenced by MCA upon expression of iMC linker. As discussed in section *1.2.3.*, MCA contributes to apparent PM tension and cell surface viscosity, which can be measured with Atomic Force Spectroscopy (AFS) by pulling static and dynamic tethers respectively (figures 3.10A, 3.11A,B). In order to extract tethers, the force probe of the AFS (the cantilever) needs to be coated with reagents that make it sticky for the PM (reviewed in (Jianwu Dai & Sheetz, 1997)). The current gold standard is Concanavalin A (conA) (Diz-Muñoz et al., 2010) (Houk et al., 2012) (Rouven Brückner et al., 2015) (Hetmanski et al., 2019), a lectin isolated from legumes that binds the sugar moiety of glycoproteins and glycolipids of the PM

(Sumner, 1919) (Goldstein & So, 1965). Aside from this function, conA has been shown to cross-link PM molecules owing to its tetravalency and the ability to form homo-oligomers, a process called agglutination (Pasternak & Elson, 1985). If the density of the targets of conA in the PM is high, the extent of the cross-linking degree is such that it leads to a substantial increase in cell surface tension (Jianwu Dai et al., 1999).

In order to avoid unwanted changes in the mechanical properties of the cell surface during tether pulling experiments, we tested the resilience of different cell lines to conA. We used morphological changes as a proxy for large alteration of cell mechanics induced by an increase in cell surface tension (reviewed in (Paluch & Heisenberg, 2009)). A549 cells exhibited extensive cell rounding within 1 h from addition of conA (figure 3.9 top) which strongly suggests high sensitivity to the reagent. Conversely, other lines – such as NIH 3t3 mouse fibroblast (Jainchill et al., 1969) and mouse Embryonic Stem Cells (mESCs) (Martin, 1981) – appeared to be resilient to the treatment (figure 3.9 center, bottom). Prior to undergoing tether pulling, we tested sensitivity to conA of all the cell lines used in this thesis; a full list can be found in procedures.

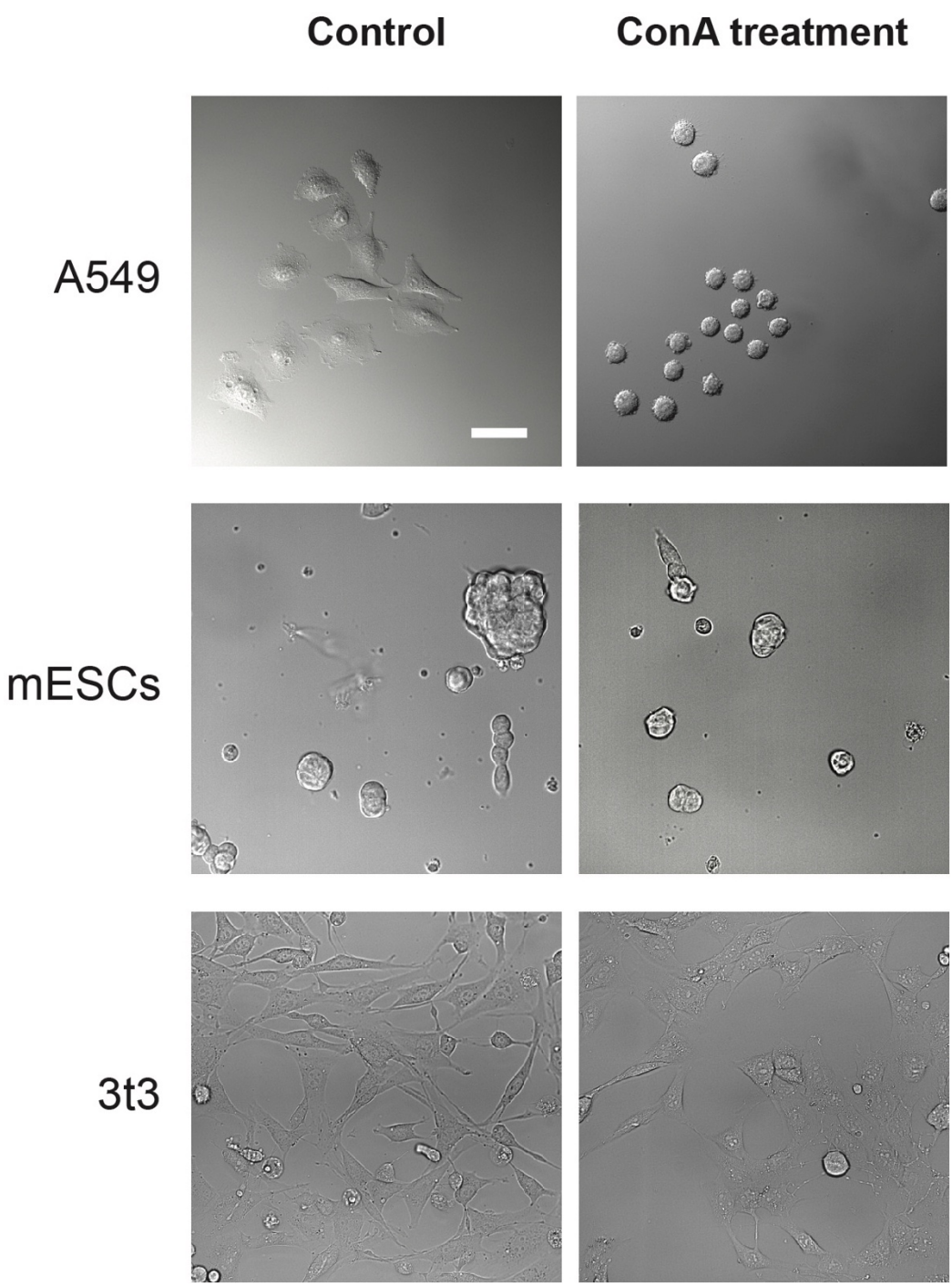

Figure 3.9. ConA stress test. Representative DIC (top) and bright field (center, bottom) images of control cells (left) and cells treated with conA for 1h (right). Scale bar: 50 µm.

We generated NIH 3t3 and mESC clonal lines that express iMC linker in an inducible manner and measured static tether force (figure 3.10). We found that both cell lines exhibit an increase in static tether force upon expression of iMC

linker (figure 3.10B,C). This translates into an over 50% increase in apparent PM tension (from 170 to 257 µN/m for NIH 3t3, and from 36.7 to 66.7 µN/m for mESCs, see procedures for details). This is in line with the increase induced by CAezrin we measured (figure 3.10D, from 48.6 to 75.4 µN/m) and previously reported in the literature (Yin Liu et al., 2012).

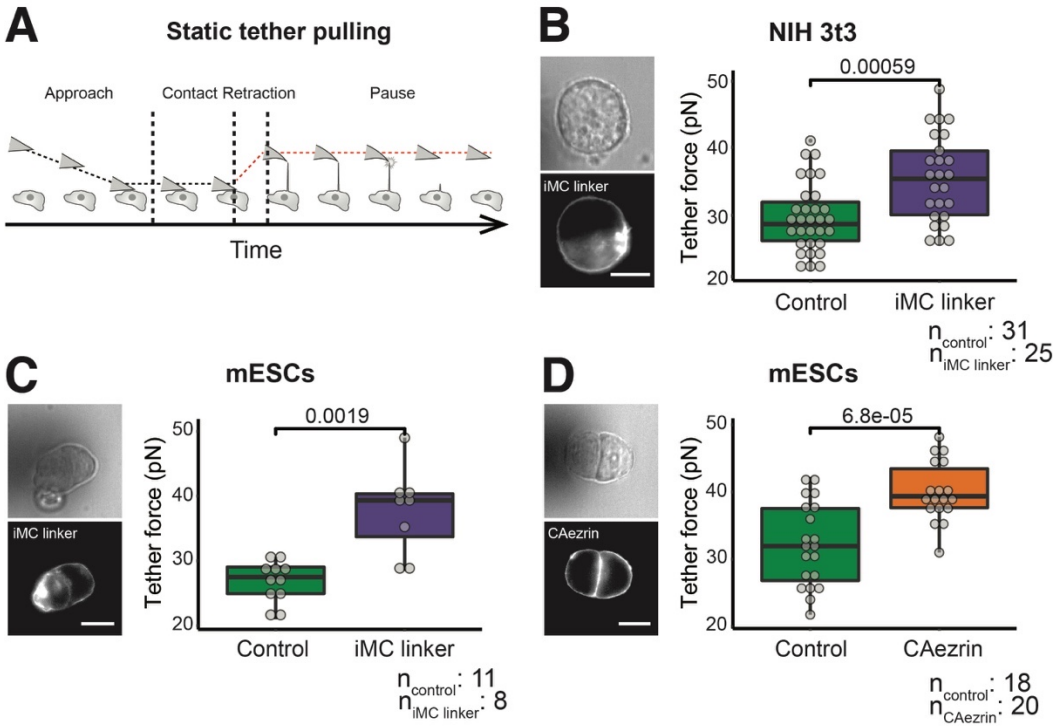

Figure 3.10.Evaluation of iMC linker and CAezrin ability to increase apparent PM tension by static tether pulling.

(A) Schematic of static tether pulling using AFS. Static tether force is measured after the retraction of the cantilever, during the pause step (*i.e.* cantilever velocity = 0 µm/s).

(B) [Left] Representative bright field (top) and epifluorescence (bottom) images of "spherical" inducible iMC linker-NIH 3t3 (clone gamma, see procedures for details). [Right] Mean static tether force of expressing (iMC linker) and uninduced (Control) cells. Gray dots: single cells. n: number of cells analyzed in 4 independent experiments. p-value: Welch's t-test.

(C) [Left] Representative bright field (top) and epifluorescence (bottom) images of inducible iMC linker-mESCs (clonal population). [Right] Mean static tether force of expressing (iMC linker) and uninduced (Control) cells. Gray dots: single cells. n: number of cells analyzed in 2 independent experiments. p-value: Welch's t-test.

(D). [Left] Representative bright field (top) and epifluorescence (bottom) images of inducible CAezrin-mESCs (clonal population). [Right] Mean static tether force of expressing (iMC linker) and uninduced (Control) cells. Gray dots: single cells. n: number of cells analyzed in 3 independent experiments. p-value: Welch's t-test.
Dark shade on the left of the BF images is the AFM cantilever.

Next, we performed dynamic tether pulling on the same clonal lines to evaluate the ability of iMC linker to increase cell surface viscosity (figure 3.11); this mechanical parameter can be used, to some extent, as readout for MCA ((Robert M. Hochmuth et al., 1996) (Brochard-Wyart et al., 2006), figure 3.11B). Surprisingly, iMC linker expressing cells showed only a minor and non-statistically significant increase in MCA MCA as analyzed by the Brochard-Wyart model (figure 3.11C,D).

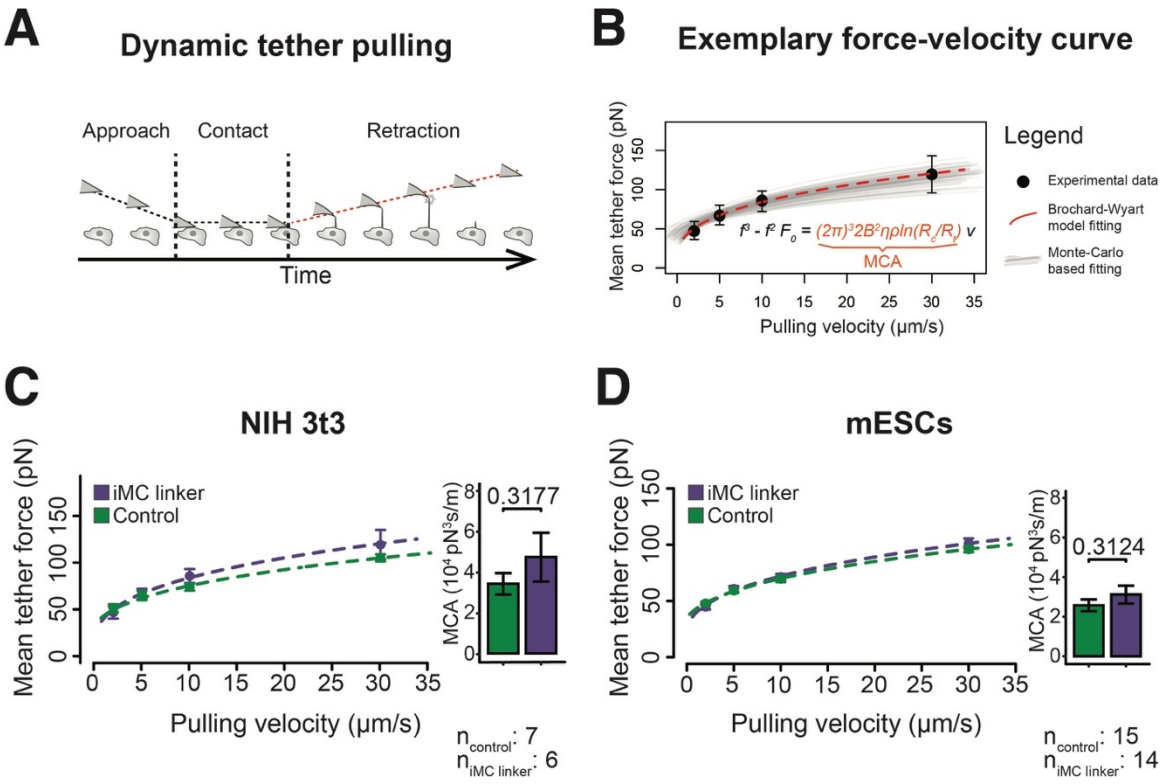

Figure 3.11. Evaluation of iMC linker ability to increase MCA (~cell surface viscosity) by dynamic tether pulling.
(A) Schematic of dynamic tether pulling using AFS. Dynamic tether force is measured during the retraction of the cantilever (*i.e.* cantilever velocity > 0 µm/s).

(B) Exemplary force-velocity curve. Points are mean dynamic tether force f ± standard error of mean at 2, 5, 10 and 30 µm/s retraction velocities. Dashed line indicates the best fit of Brochard-Wyart et al. model (Brochard-Wyart et al., 2006). Solid lines indicate Monte-Carlo fits of Brochard-Wyart et al. model (see procedures for details). Solid lines omitted in C, D and figure 3.12 for clarity.
(C) [Left] Force-velocity curve from dynamic tether pulling on "spherical" inducible iMC linker-NIH 3t3 (clone gamma). Data points are mean f ± standard error of mean at 2, 5, 10, and 30 µm/s pulling velocities. iMC linker: cells expressing iMC linker. Control: uninduced cells. n: number of cells analyzed in 2 independent experiments. [Right] Mean and standard deviation of MCA (~cell surface viscosity) obtained from Monte Carlo-based fitting. p-value: Z test.
(D) [Left] Force-velocity curve from dynamic tether pulling on clonal inducible iMC linker-mESCs. Data points are mean f ± standard error of mean at 2, 5, 10, and 30 µm/s retraction velocities. iMC linker: cells expressing iMC linker. Control: uninduced cells. n: number of cells analyzed in 3 independent experiments. [Right] Mean and standard deviation of MCA (~cell surface viscosity) obtained from Monte Carlo-based fitting. p-value: Z test.

To understand this conundrum, we reviewed all the literature on dynamic tether pulling. This method has been used to measure MCA in different conditions and cell lines. Remarkably, substantial reduction in MCA was observed by overexpressing DNEzrin [a dominant negative version of Ezrin, T567A (Yonemura et al., 1999)], by downregulating endogenous ERM proteins, and by treating cells with cyclodextrins [a family of compounds that extracts cholesterol from the PM (reviewed in (Zidovetzki & Levitan, 2007))] (figure 3.25B) (Krieg et al., 2008) (Diz-Muñoz et al., 2010) (Sun et al., 2007). Notwithstanding, to the best of our knowledge, there are no studies that measure an increase in MCA upon perturbation of cell surface mechanics using dynamic tether pulling. Aiming to estimate the magnitude of cell surface viscosity increase induced by established MCA perturbation methods, we performed dynamic tether pulling on cells expressing CAezrin (figure 3.12). We reasoned that any putative CAezrin-dependent increase in MCA might be dependent on the cell type or on experimental conditions. Therefore, we tested various cell lines, ranging from fully spread cells (HeLa Kyoto, HEK-293T and MCF10a (Yasuda et al., 2004) (Russell et al., 1977) (Tait et al., 1990)), to cells which present a quasi-spherical shape (mESCs, and "spherical" NIH 3t3, see procedures for details), to fast

migrating cells (HL60 (Gallagher et al., 1979)). We tested also different types of expression (constitutive and inducible) and different expression levels, since the high expressers of CAezrin-HL60 and CAezrin-NIH 3t3 lines have been isolated using Fluorescence-Activated cell sorting (FACS) and super-transfection of CAezrin. All the measurements in figure 3.12 showed that, similarly to iMC linker, CAezrin overexpression leads only to a minor increase in MCA. Based on static tether (figure 3.10) and dynamic tether pulling (figures 3.11, 3.12), we concluded that iMC linker induces an increase in the MCA component of cell surface viscosity comparable to the increase obtained with established methods such as CAezrin overexpression.

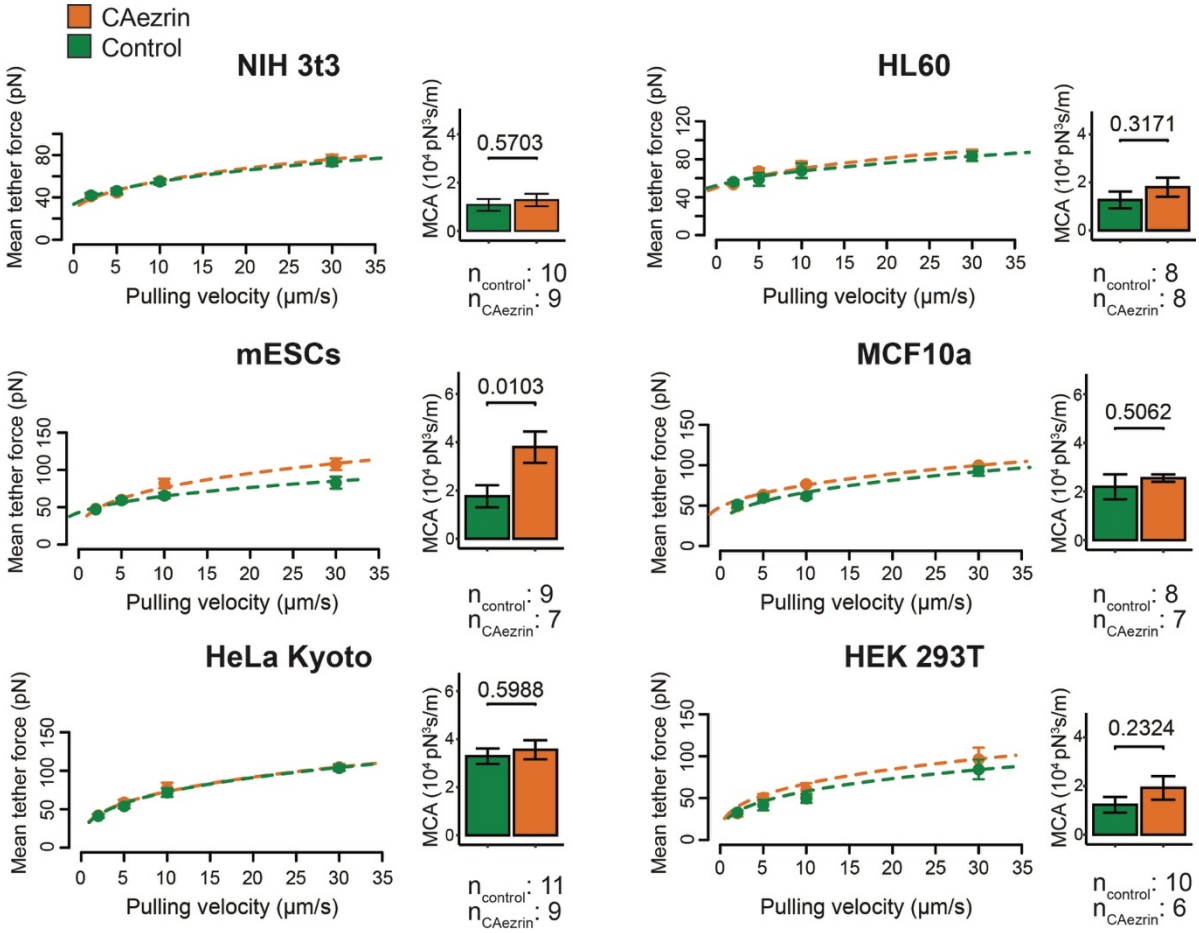

Figure 3.12. Evaluation of CAezrin ability to increase MCA (~cell surface viscosity) by dynamic tether pulling. For each cell line: [Left] Force-velocity curve from dynamic tether pulling on CAezrin expressing (orange) and control cells (green). Data points are mean f ± standard error of the mean at 2, 5, 10, and 30 µm/s retraction velocities. [Right] Mean and

standard deviation of MCA (~cell surface viscosity) obtained from Monte Carlo-based fitting. p-value: Z test.
CAezrin: cells expressing CAezrin. Control: uninduced cells (for inducible lines) or wt cells (for lines constitutively expressing CAezrin). n: number of cells analyzed in 3 independent experiments (NIH 3t3, mESCs and HeLa Kyoto) or in 2 independent experiments (MCF10a, HL60, and HEK 293T).
HEK 293T, HeLa Kyoto, HL60, MCF10a, “spherical” NIH 3t3, HL60: non-clonal lines, constitutively expressing CAezrin. mESCs: clonal line, CAezrin expression upon induction. “spherical” NIH 3t3, HL60: high expressers isolated using FACS and super-transfected to further increase CAezrin expression.

3.1.5. Final discussion of part A

In Part A of my thesis, I described the development of a platform for relatively high throughput screening of signaling-inert artificial MCA linkers. Four candidates were found to efficiently inhibit blebbing of confined A549 cells. Artificial linker-mediated blebbing inhibition appeared to be expression level-dependent. This implies that candidate linkers discarded during our screening might still be effective if expressed at higher levels. However, pushing their over-expression may easily lead to cytotoxic effects owing to the metabolic energy invested by cells in their synthesis. Therefore, upon optimization of the transfection method, we tested the candidates without enhancing expression.

Among the four screened artificial linkers, we chose Lyn motif-mCherry-CHCH(Utr) as final candidate and renamed it iMC linker. We validated the linker by measuring the mechanical properties influenced by MCA and found its expression leads to increases in apparent PM tension and cell surface viscosity of about the same magnitudes of CAezrin.

iMC linker is an elegant molecular tool that allows to increase MCA and to study the role of this element of the cell surface in biological process and cell surface mechanics. A key characteristic of iMC linker is signaling inertia, which is determined by the biochemical properties of the domains that constitute it. Remarkably, co-expression of the component of the linker, namely Lyn motif-mCherry and mCherry-CHCH(Utr), is a precise control to assess any effect of the domains of iMC linker on the cell process/biophysical property of interest.

3.1.5.1. Limitations and possible improvements of iMC linker

Despite the fact we believe that iMC linker is extremely valuable to study unambiguously MCA, it presents some limitations. In particular, its activity can be controlled only at the genetic level through inducible transcription, restricting its usage to investigating MCA-regulated cell processes with time-scales similar

to protein expression. Furthermore, iMC linker is active throughout the cell, hence MCA cannot be modulated with subcellular resolution. Improvements of the temporal and spatial resolution may be achieved by re-devising iMC linker as a two-component system. The first component would be the PM-binding domain (Lyn motif) fused to a protein which heterodimerizes with its partner only when a specific signal is provided. The second component will carry the filamentous actin-binding domain (CHCH(Utr)) linked to the partner of the heterodimerizing protein present in the first component. Cells will stably express the linker which – upon the administration of the signal – will heterodimerize and increase MCA (figure 3.13A). Among the vast plethora of heterodimerizing systems, the optogenetic ones may provide extremely fine experimental control on the activation of a two-component variant of iMC linker (reviewed in (Fenno et al., 2011)). Of particular interest is the PhyB-PIF optogenetic system, which display fast activation kinetics, inactivation can be controlled experimentally, and its activity can be spatially controlled up to diffraction-limited resolution ((Levskaya et al., 2009); figure 3.13B).

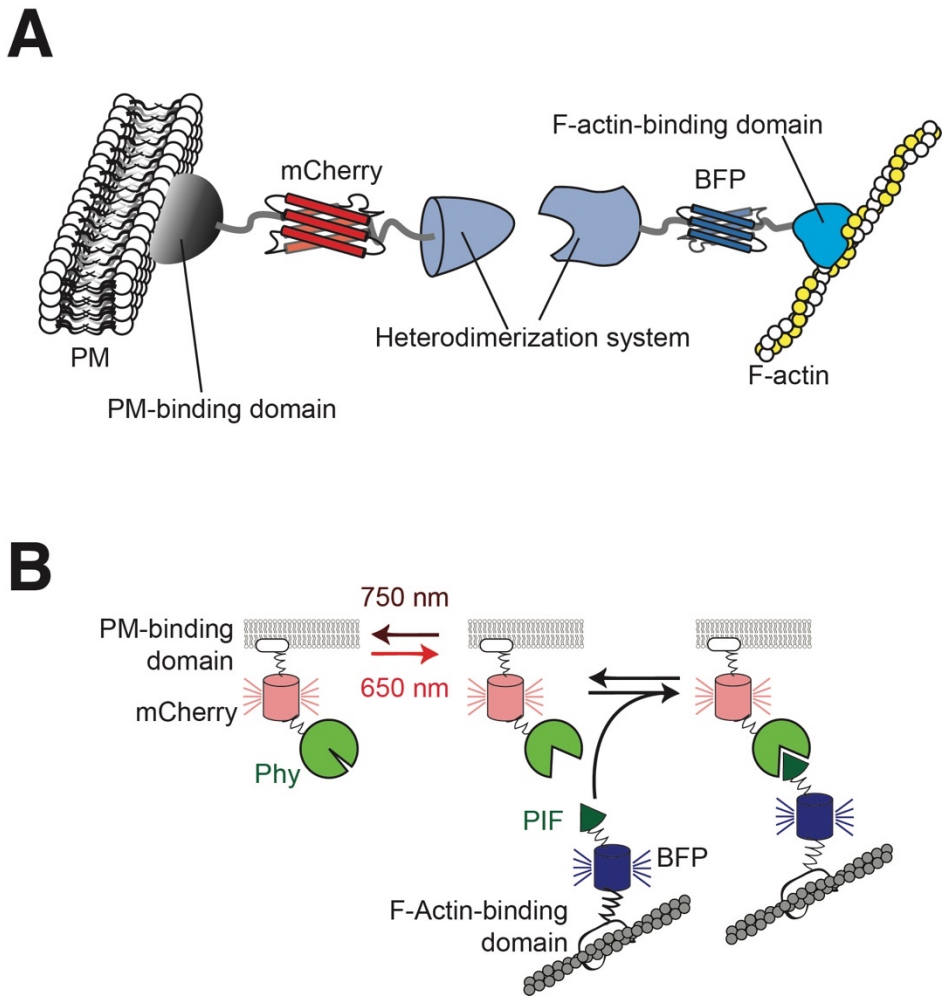

Figure 3.13. Two-component version of iMC linker.
(A) Schematic of general design of a two-component artificial linker.
(B) Schematic of an optogenetic version of an artificial linker based on PhyB-PIF optogenetic system. Red light (650nm) delivered to the system, is absorbed by PhyB cofactor PCB, whose consequent photoisomerization is coupled to an allosteric conversion of PhyB into its active configuration. The active form of PhyB binds its partner Phytochrome Interaction Factor 3 (PIF3). PhyB inactivation is induced with far-red light (750nm) which triggers the restoration of PCB initial isomeric state.

3.1.5.2. Dynamic tether pulling: is it a reliable method?

As discussed in section *3.1.4*. and shown in figure 3.10, the expression of CAEzrin or the iMC linker does change mechanical properties and cell behavior, suggesting that the currently used Brochard-Wyart model might not be sufficient to capture changes in MCA. This could be due to the fact that this model assumes

the cell cortex to be a wall. As I will show in sections *3.3.* from this thesis our latest results challenge that assumption and bring a new level of complexity to the dynamic tether pulling experiments that will require new theoretical models to be developed to fully understand surface mechanical properties from tether pulling experiments.

3.2. Part B: Membrane-to-cortex attachment gates stem cell differentiation.

"*Cell and tissue, shell and bone, leaf and flower, are so many portions of matter, and it is in obedience to the laws of physics that their particles have been moved, molded and conformed*" (Thompson, 1917). This quotation from D'Arcy Thompson's masterpiece *On Growth and Form* encapsulates one of the key concepts in the modern field of cell mechanics: cell specialization requires the acquisition of precise shapes, which in turn is governed by mechanical forces, properties and constrains. Stem cell differentiation is arguably the most clear example of this phenomenon since – during the development of multicellular organisms – relatively round totipotent cells give rise to differentiated cells with all the dramatically different morphologies present in the adult body. Mechanical cues from the extracellular environment and cell surface mechanics are master regulators of cell shape (reviewed in (Janson & Putnam, 2015) (Haupt & Minc, 2018)). In fact, several studies have appointed cell-matrix interactions to be essential drivers of cell differentiation (Engler et al., 2006) (Chowdhury, Li, et al., 2010) (Murray et al., 2013) (reviewed in (Muncie & Weaver, 2018)). On the contrary, whether and how the cell intrinsic surface mechanics regulate fate remains elusive.

In this part of the thesis, I am describing our efforts in deciphering the role of cell surface mechanics, and in particular MCA, in a cell differentiation event characterized by considerable morphological changes. Specifically, we focused on the transition from the naïve to the primed pluripotent state during early differentiation of mESCs. We found that naïve stem cells have to release their PM from the underlying actin cortex to transition to the primed state. The findings described in this chapter of the thesis will be published in the February 2021 issue of Cell Stem Cell with me as a first co-author. The study can already be found online (Bergert, Lembo et al., 2020).

3.2.1. Mouse embryonic stem cells as a model system to unravel cell surface mechanics during differentiation.

1980s, embryonic stem cell lines have been the gold standard to study stemness and differentiation in the early stages of mammalian development. At a glance, the key difference between the naïve and the primed state of mESCs lies in their pluripotency potential. This feature can be tested through various pluripotency assays, such as evaluation of their contribution to the formation of chimeric embryos in rodents; cells in the naïve state excel in this assay whereas primed cells perform quite poorly (reviewed in (Mascetti & Pedersen, 2016)). Naïve cells express a larger roster of pluripotency transcription factors than primed cells, which includes also the reprogramming factors Nanog, Klf2, and Klf4 (reviewed in (Hackett & Surani, 2014)). These differences in gene expression feedback with the epigenetic ones, with naïve cells being hypomethylated and having both the X chromosomes active (in cells isolated from female embryos), and primed cells being hypermethylated and undergoing X-inactivation (reviewed in (Takahashi et al., 2018)). Finally, the morphologies of naïve and primed cells are rather divergent: the former are relatively round and grow in compact dome-shaped colonies, whereas the latter spread out, and form a flat monolayer (figure 3.14).

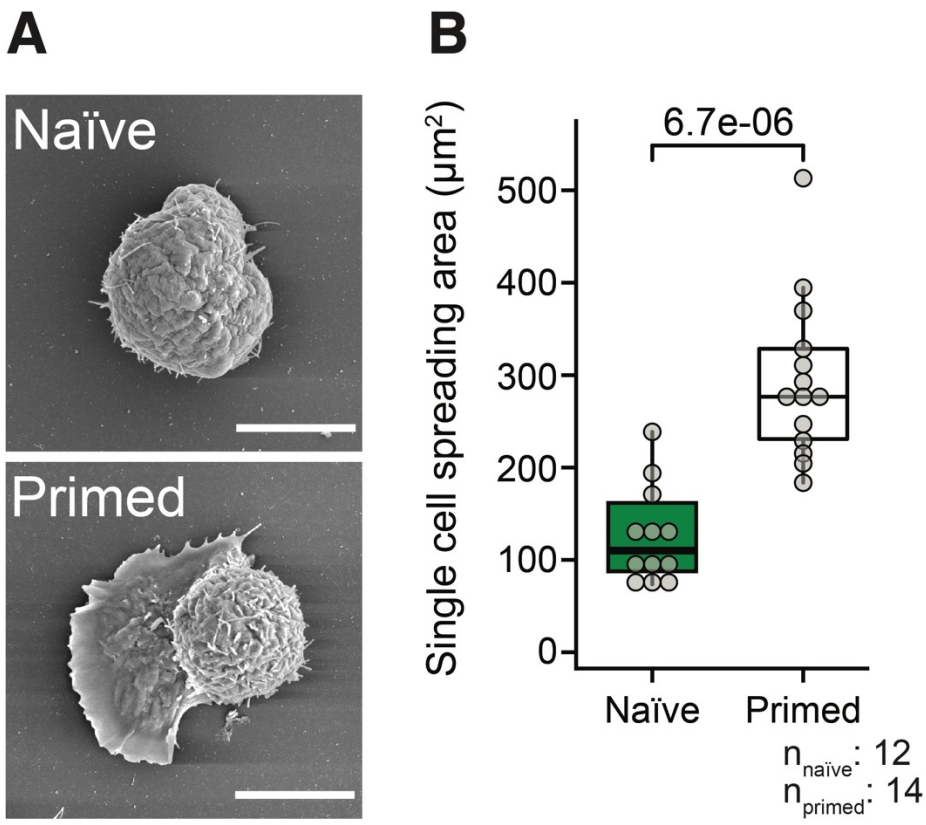

Figure 3.14. Mouse embryonic stem cells (mESCs) morphology in the naïve and primed state.
(A) Representative scanning electron microscopy images of naïve (2i/LIF) and primed (FGF2/ActA) mESC Rex1-GFPd2 cells. Scale bar: 10 µm.
(B) Single cell spreading area quantified from scanning electron microscopy images. Gray dots: single cells. n: number of cells analyzed. p-value: Welch's t-test.
Modified from (Bergert, Lembo et al., 2020).

Using different culture media, mESCs can be either locked in one of the two states or naïve-to-primed transition can be elicited (figure 3.15A, see procedures for details). Naïve cells can be propagated unlimitedly by growing them in presence of 2i/LIF (2 small molecule inhibitors [PD0325901 and CHIR99021] and leukemia inhibitory factor [LIF]) (Mulas et al., 2019). 2i/LIF removal releases the differentiation blockade, and naïve colonies rapidly (within 24-48 h) flatten into a monolayer of primed cells that grow lamellipodia-like protrusions. Finally, differentiation can be halted by adding to the medium FGF2/ActA (fibroblast growth factor 2 and Activin A) which lock the cells in the primed state. The pluripotency state of mESCs is mirrored by the expression of the naïve pluripotency marker Rex1-

GFPd2, and thus it can be monitored in live cells by employing a mESC line engineered with a GFP reporter gene expressed under the control of the Rex1 promoter. (figure 3.15B) (Toyooka et al., 2008) (Wray et al., 2011).

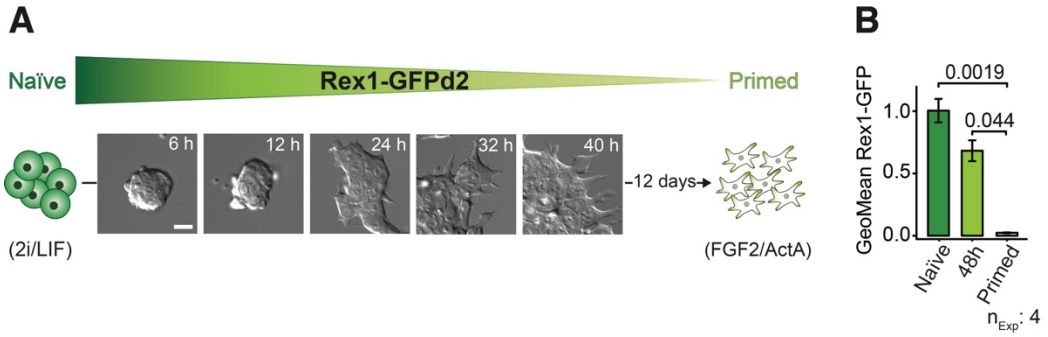

Figure 3.15. Exit from naïve pluripotency.
(A) Schematic and representative DIC images of mESC Rex1-GFPd2 cells during exit from naïve pluripotency in N2B27 medium. Scale bar: 10 µm.
(B) Normalized GFP geometric mean intensities for mESC Rex1-GFPd2 cells in 2i/LIF medium, during exit from naïve pluripotency in N2B27 medium at 48 h and primed in FGF2/ActA medium. nExp: number of independent experiments. Error bars: SEM. p-values: Welch's t-test.
Modified from (Bergert, Lembo et al., 2020).

3.2.2. Naïve-to-primed transition is characterized by a cell intrinsic – but cell shape-independent – reduction in MCA.

To evaluate changes in the mechanical properties of the cell surface between the two states of mESCs, we measured apparent PM tension in the naïve and primed cells by static tether pulling via AFS. We found that static tether force was significantly reduced in primed cells (Figure 3.16A) leading to an almost 50% reduction in apparent PM tension (from 80 to 42 µN/m see procedure for details). Several studies have linked the formation of lamellipodia – which here accompanies the transition to the primed state (figures 3.14A, 3.15) – to an increase in in-plane PM tension (see section 1.3.2). Consequently, we hypothesized that the reduction of apparent PM tension between naïve and primed mESCs was likely to be caused by a reduction in MCA. To confirm this hypothesis, we performed dynamic tether pulling and found a 3-fold reduction

in cell surface viscosity (~MCA) in cells locked in the primed state (figure 3.16B Naïve *vs.* Primed). Importantly, the reduction in MCA occurs within 48h of the 2i/LIF removal (figure 3.16B naïve *vs.* 48h), in agreement with the known time frame for exiting from naïve pluripotency (Mulas et al., 2019).

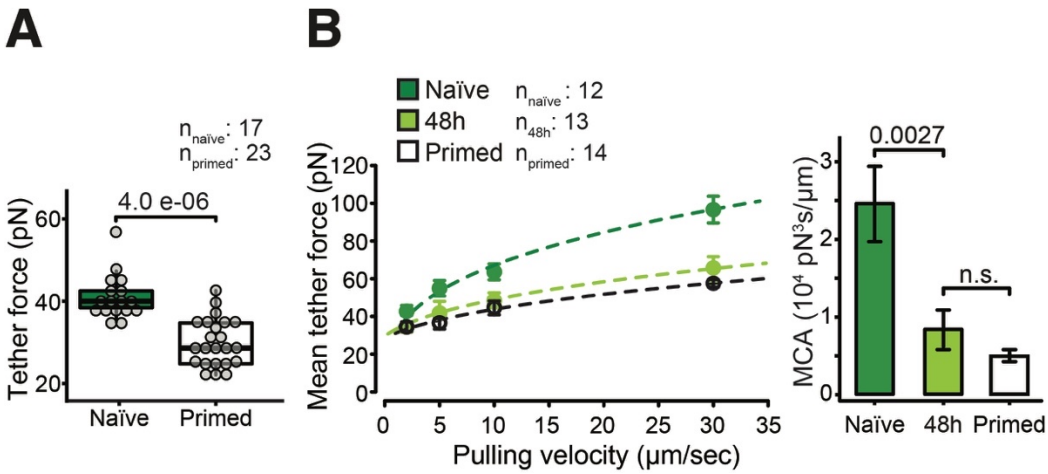

Figure3.16. Naïve-to-primed transition is accompanied by a reduction in MCA.
(A) Mean static tether force of naïve (2i/LIF) and primed (FGF2/ActA) mESC Rex1-GFPd2 cells. Gray dots: single cells. n: number of cells analyzed in 2 independent experiments. p-value: Mann-Whitney-U-Test.
(B) [Left] Force-velocity curve from dynamic tether pulling on mESC Rex1-GFPd2 cells in 2i/LIF medium, during exit from pluripotency in N2B27 medium at 48 h and primed in FGF2/ActA medium. Data points are mean tether force *f* ± SEM at 2, 5, 10 and 30 µm/s pulling velocity. n: number of cells analyzed in 3 independent experiments. [Right] Mean and standard deviation of MCA (~cell surface viscosity) obtained from Monte-Carlo-based fitting p-value: Z test.
Modified from (Bergert, Lembo et al., 2020).

As MCA reduction and cell spreading occur simultaneously, we next investigated the relationship between MCA and cell shape. To-that-end, we forced naïve cells to spread by plating them on Laminin 511 (L511) in the presence of 2i/LIF (Figures 3.17A,B). Cell spreading *per se* does not elicit naïve-to-primed transition, as indicated by the expression of the naïve markers Rex1-GFPd2 and Nanog (figure 3.17C). Furthermore, we found that spread naïve cells retain high values of MCA (figure 3.17D), showing that (i) an increase in cell area alone is not sufficient to reduce MCA and, (ii) MCA is independent of the chemical composition of the extracellular environment.

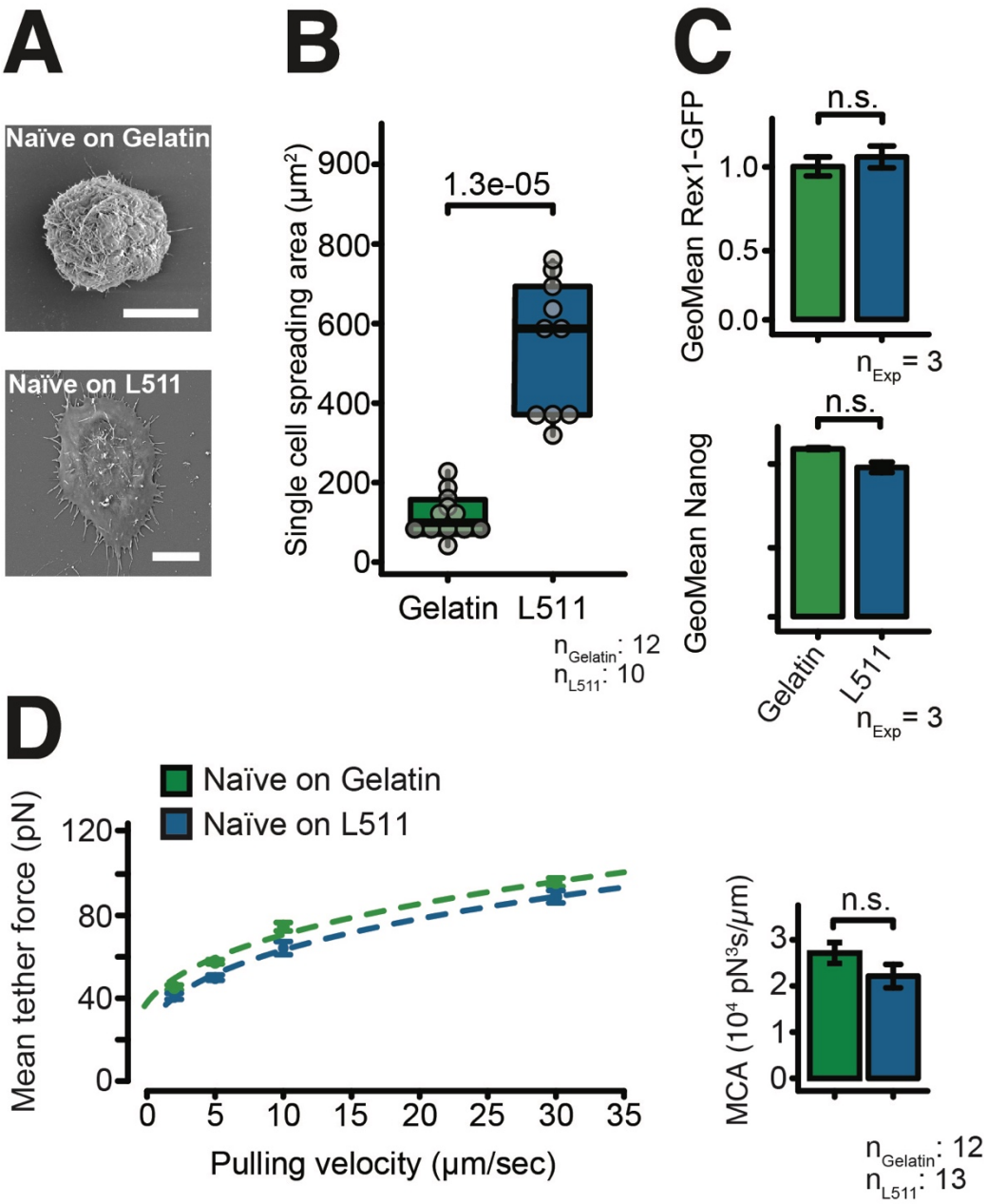

Figure 3.17. Cell spreading is not sufficient to elicit naïve-to-primed transition and does not affect MCA in naïve cells.

(A) Representative scanning electron microscopy images of naïve (2i/LIF) mESC Rex1-GFPd2 cells on Gelatin or on L511. Scale bar: 10 µm.

(B) Single cell spreading area quantified from scanning electron microscopy images. Gray dots: single cells. n: number of cells analyzed. p-value: Welch's t-test.

(C) [Top] Normalized GFP geometric mean intensities for mESCs Rex1-GFPd2 in 2i/LIF medium plated for 48h on Gelatin or on L511. [Bottom] Normalized geometric mean intensities of Nanog immunofluorecence levels for mESCs Rex1-

GFPd2 in 2i/LIF medium plated for 48h on Gelatin or on Laminin 511. nExp: number of independent experiments. Error bars: SEM. p-values: Welch's t-test.
(D) [Left] Force-velocity curve from dynamic tether pulling on naïve (2i/LIF) mESC Rex1-GFPd2 cells plated on Gelatin or L511. Data points are mean tether force *f* ± SEM at 2, 5, 10 and 30 µm/s pulling velocity. n: number of cells analyzed in 3 independent experiments. [Right] Mean and standard deviation of MCA (~cell surface viscosity) obtained from Monte-Carlo-based fitting p-value: Z test.
Modified from (Bergert, Lembo et al., 2020).

Finally, we asked whether naïve pluripotency and MCA are influenced by the mechanical properties of the extracellular environment. We seeded naïve cells on substrates with different stiffness (0.5 or 25 kPa hydrogels), mimicking a range of tissue stiffnesses, from brain-like to cartilage-like (Guimarães et al., 2020). Consistent with the results obtained with mESCs plated on L511, neither naïve pluripotency (figure 3.18A) nor MCA (figure 3.18B) are affected by cell extrinsic physical factors such as substrate stiffness.

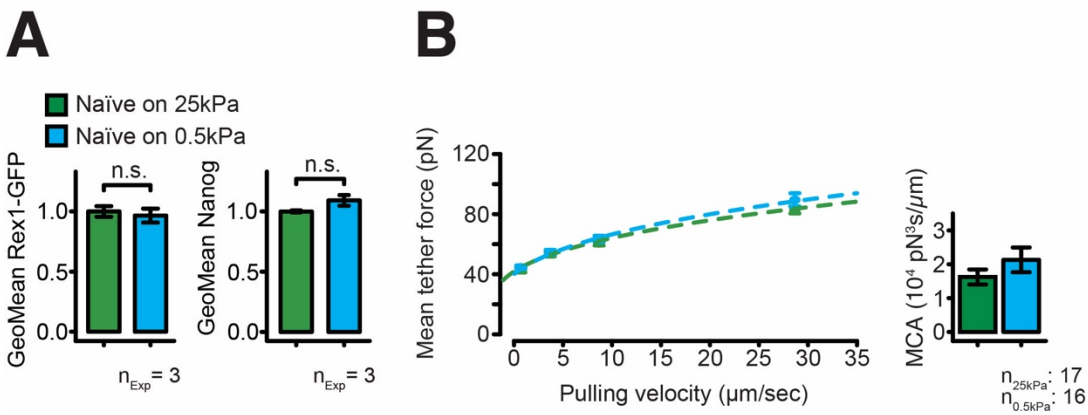

Figure 3.18. Naïve pluripotency state and MCA are independent of the stiffness of the extracellular substrate.
(A) [Left] Normalized GFP geometric mean intensities for mESC Rex1-GFPd2 cells in 2i/LIF medium after plating for 48 h on L511-coated hydrogels of 25 kPa or 0.5 kPa. [Right] Normalized geometric mean intensities of Nanog immunofluorescence levels for mESC Rex1-GFPd2 cells in 2i/LIF medium after plating for 48 h on L511-coated hydrogels of 25 kPa or 0.5 kPa. nExp: number of independent experiments. Error bars: SEM. p-values: Welch's t-test.
(B) [Left] Force-velocity curve from dynamic tether pulling on mESC Rex1-GFPd2 cells in 2i/LIF medium after plating for 48 h on Laminin 511-coated hydrogels of 25 kPa or 0.5 kPa stiffness. Data points are mean tether force *f* ± SEM at 2, 5, 10 and 30 µm/s pulling velocity. n: number of cells analyzed in 3 independent

experiments. [Right] Mean and standard deviation of MCA (~cell surface viscosity) obtained from Monte-Carlo-based fitting p-value: Z test.
Modified from (Bergert, Lembo et al., 2020).

We therefore concluded that naïve-to-primed transition is accompanied by a cell intrinsic reduction in MCA and that this change in cell surface mechanics is not a consequence of cell spreading.

3.2.3. MCA is a novel regulator of the exit from naïve pluripotency

The co-occurrence of the exit from naïve pluripotency and reduction of MCA suggests a causal relationship between the two phenomena. To investigate whether the reduction in MCA is upstream, i.e. a regulator, or downstream, i.e. a consequence, of the exit from naïve pluripotency, we decided to use iMC linker (section *3.1*.). First, we assessed the ability of the artificial MCA linker to prevent the observed MCA reduction by simultaneously inducing its expression and eliciting the exit from naïve pluripotency. As expected, iMC linker-expressing mESCs maintained a high MCA after 48 h after 2i/LIF removal, with values similar to naïve mESCs and in stark contrast to the strongly decreased MCA of uninduced controls (figure 3.19A,B). Similarly, inducing CAezrin expression also forced stem cells to retain a high MCA 48 h after eliciting differentiation by 2i/LIF removal. (figure 3.19C,D).

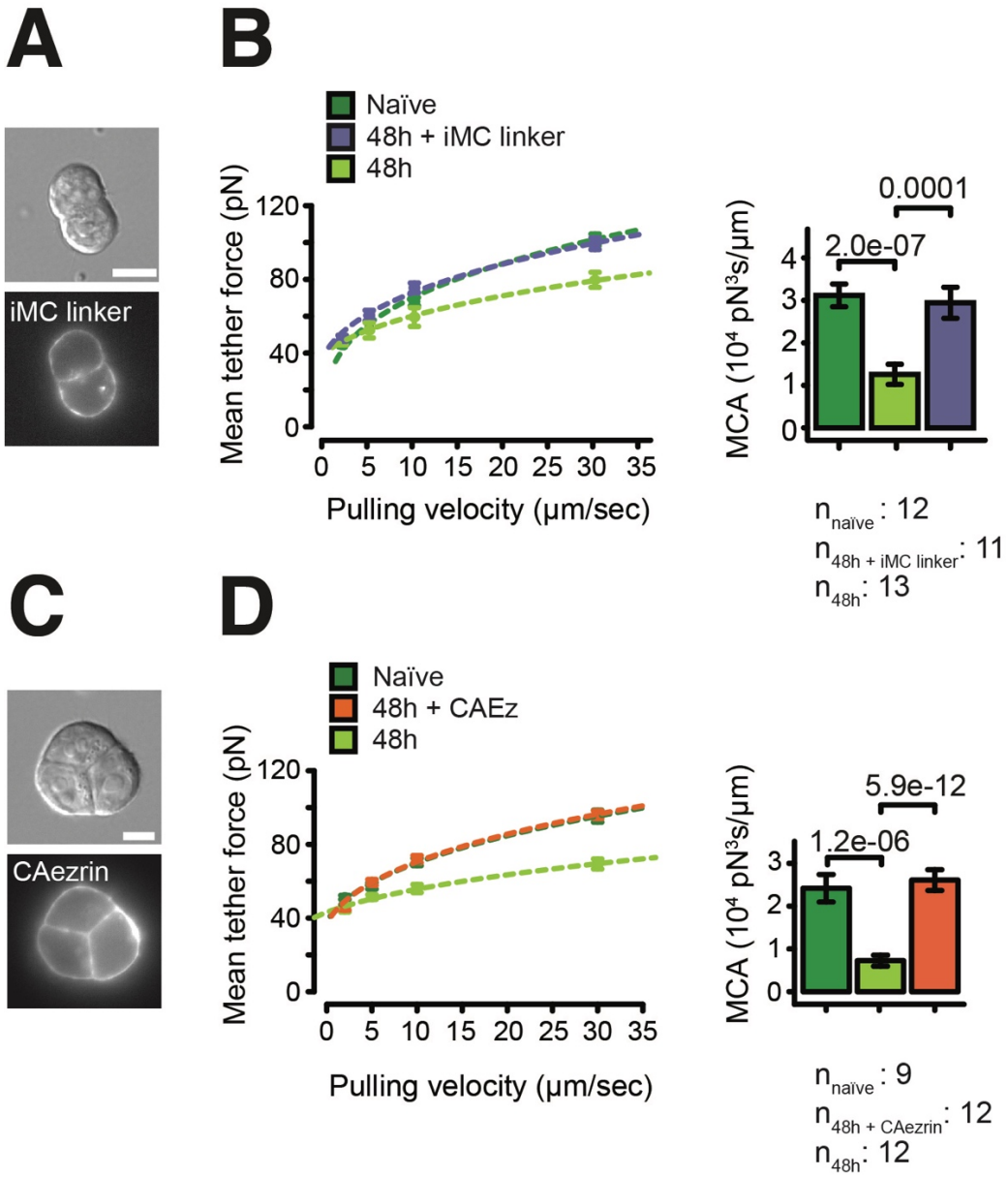

Figure 3.19. Ectopic expression of iMC linker or CAezrin prevents MCA reduction upon exit from naïve pluripotency.

(A) Representative brightfield (DIC) and fluorescent images of naïve mESC Rex1-GFPd2 ind-iMC linker cells expressing the iMC linker in 2i/LIF+Dox medium. Scale bar: 10 µm.

(B) [Left] Force-velocity curve from dynamic tether pulling on mESC Rex1-GFPd2 ind-iMC linker cells in 2i/LIF medium and during exit from pluripotency in N2B27±Dox medium at 48 h. Data points are mean tether force *f* ± SEM at 2, 5, 10 and 30 µm/s pulling velocity. n: number of cells analyzed in 3 independent experiments. [Right] Mean and standard deviation of MCA (~cell surface viscosity) obtained from Monte-Carlo-based fitting. p-value: Z test.

(C) Representative brightfield (DIC) and fluorescent images of naïve mESC Rex1-GFPd2 ind-CAezrin cells expressing CAezrin-mCherry in 2i/LIF+Dox medium. Scale bar: 10 µm.
(D) [Left] Force-velocity curve from dynamic tether pulling on mESC Rex1-GFPd2 ind-CAezrin cells in 2i/LIF medium and during exit from pluripotency in N2B27±Dox medium at 48 h. Data points are mean tether force *f* ± SEM at 2, 5, 10 and 30 µm/s pulling velocity. n: number of cells analyzed in 3 independent experiments. [Right] Mean and standard deviation of MCA (~cell surface viscosity) obtained from Monte-Carlo-based fitting. p-value: Z test.
Modified from (Bergert, Lembo et al., 2020).

We next investigated whether forcing cells to keep high MCA by expression of iMC linker or CAEzrin affects their ability to exit from naïve pluripotency. First, we dynamically evaluated the exit from naïve pluripotency in living cells by monitoring the expression of the reporter gene Rex1-GFPd2 upon expression of the exogenous MCA linkers. 48 h after 2i/LIF removal, iMC linker- or CAezrin-expressing cells retained high levels of the naïve pluripotency marker Rex1, very similar to naïve stem cells and in contrast to uninduced cells (Figure 3.20A). In addition, we assessed the change in expression of Nanog, another naïve pluripotency marker, in fixed cells. We found that cells with high MCA display elevated Nanog levels compared to the uninduced controls (figure 3.20B). Importantly, the expression of only mCherry or individual iMC linker components (Lyn motif-mCherry and mCherry-CHCH(Utr)) failed at preventing Rex1 downregulation (figure 3.20C) even at higher expression levels than iMC linker and CAezrin (figure 3.20D). This strongly suggests that that iMC linker ability to increase MCA is responsible for the retention of expression of the naïve markers.

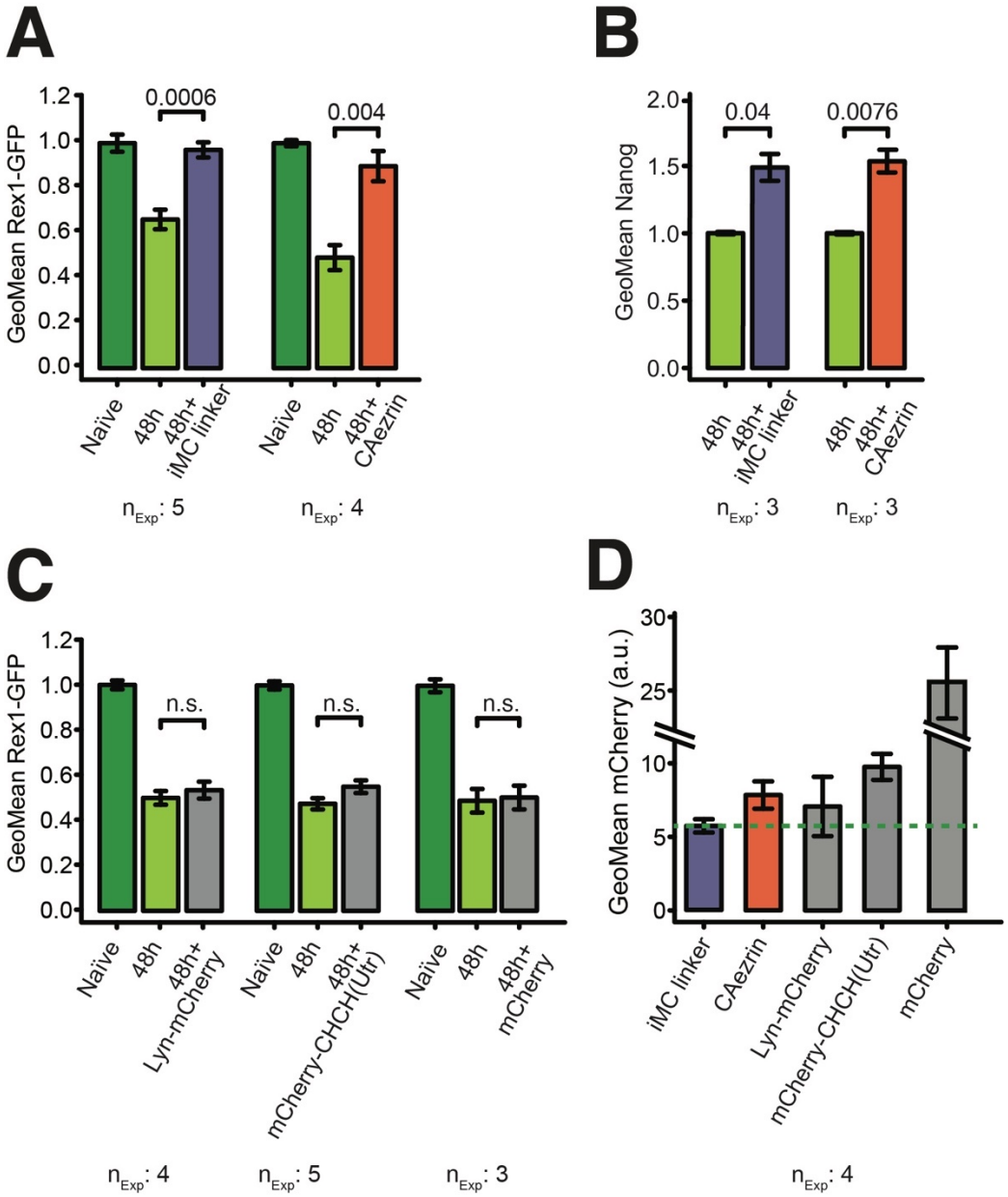

Figure 3.20. Prevention of MCA reduction during exit from pluripotency is coupled to retention of naïve pluripotency markers.

(A) Normalized GFP geometric mean intensities for mESC Rex1-GFPd2 ind-iMC linker or ind-CAezrin cells in 2i/LIF medium and during exit from pluripotency in N2B27±Dox medium at 48 h. nExp: number of independent experiments. Error bars: SEM. p-value: Welch's t-test

(B) Normalized geometric mean intensities of Nanog immunofluorescence levels for mESC Rex1-GFPd2 ind-iMC linker and ind-CAezrin cells plated for 48h in N2B27 media or in N2B27+Dox media. nExp: number of independent experiments. Error bars: SEM. p-values: Welch's t-test.

(C) Normalized GFP geometric mean intensities for mESC Rex1-GFPd2 ind-Lyn motif-mCherry, ind-mCherry-CHCH(Utr) and ind-mCherry cells in 2i/LIF medium

during exit from pluripotency in N2B27±Dox medium at 48 h. nExp: number of independent experiments. Error bars: SEM. p-value: Welch's t-test.
(D) mCherry geometric mean intensities for mESC Rex1-GFPd2 ind-iMC linker, ind-CAezrin, ind-Lyn motif-mCherry, ind- mCherry-CHCH(Utr), and ind-mCherry cells during exit from pluripotency in N2B27±Dox medium at 48 h. nExp: number of independent experiments. Error bars: SEM.
Modified from (Bergert, Lembo et al., 2020).

In order to obtain a more global picture of the status of the cellular transcriptome with high MCA, we then performed RNA-seq during a time course upon 2i/LIF removal of induced and uninduced iMC linker and CAezrin cells. We observed that the self-organizing network of transcription factors that governs naïve pluripotency (Niwa, 2007) is upregulated in iMC linker and CAezrin expressing cells (top KEGG database enriched pathway maps: “Signaling pathways regulating pluripotency of stem cells” (Figure 3.21A,B)). Moreover, consistent with the observations on Rex1-GFPd2 and Nanog, we found that the expression of various naïve pluripotency genes (Kalkan et al., 2017) is elevated in cells with high MCA (Figure 3.21C).

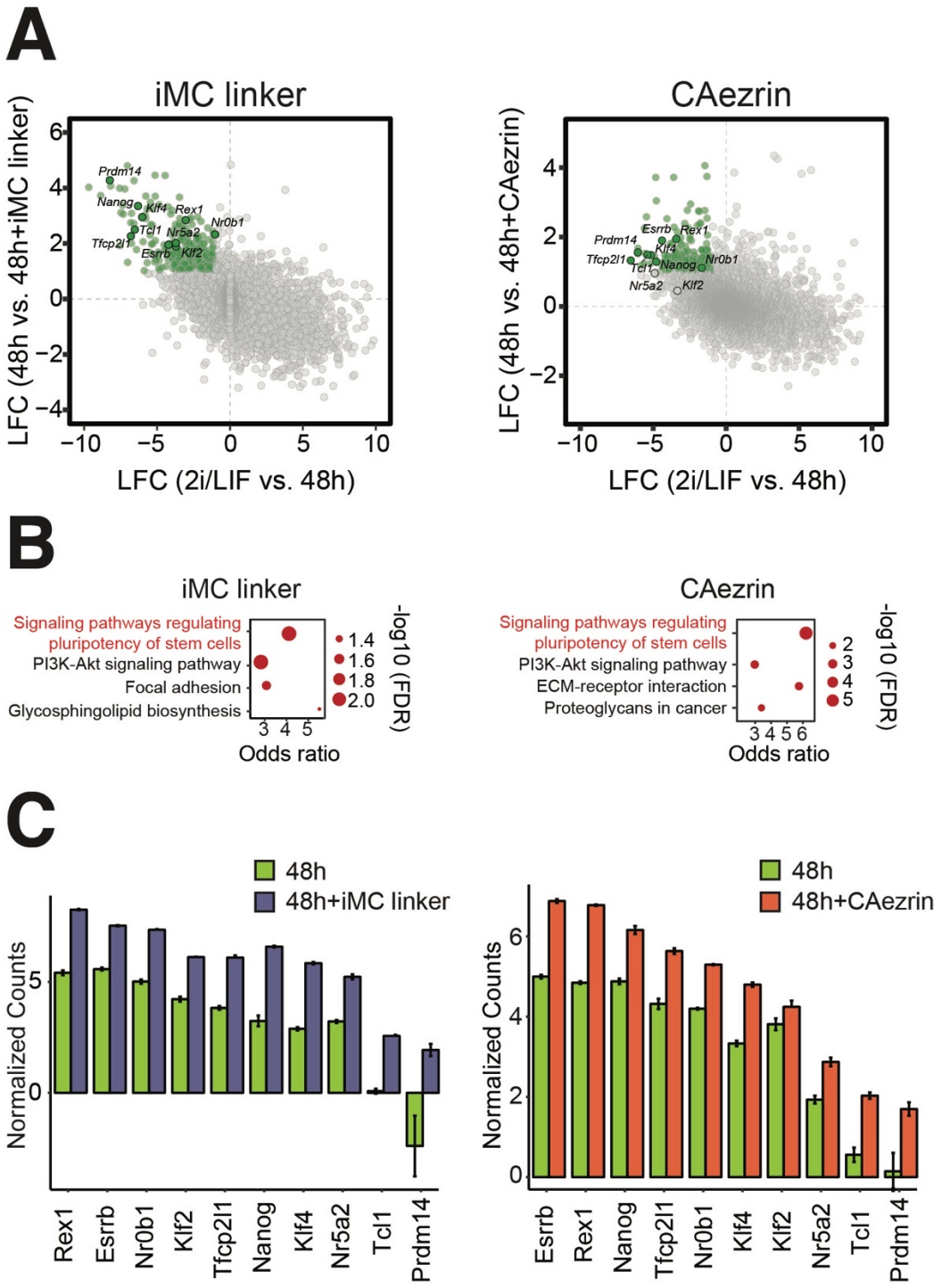

Figure 3.21. preventing MCA reduction during exit from pluripotency leads to the upregulation of the naïve pluripotency network of transcription factors.
(A) Comparison of mRNA fold-changes for mESC Rex1-GFPd2 ind-iMC linker and ind-CAezrin cells grown in 2i/LIF and N2B27+Dox media (48 h) with plain N2B27 media (48 h). Naïve pluripotency genes (Kalkan et al., 2017) were upregulated both in cells grown in 2i/LIF medium and N2B27+Dox medium (upper left

quadrant, green: significantly enriched genes (log-fold-change (LFC) >1 and false discovery rate (FDR) <0.05)). Data from 3 independent RNAseq experiments.
(B) RNAseq-derived enriched pathway maps in mESC Rex1-GFPd2 ind-iMC linker and ind-CAzrin cells in N2B27+Dox medium compared to plain N2B27 medium at 48 h. Significantly enriched genes (log-fold-change (LFC) >1 and false discovery rate (FDR) <0.05) from differential RNA-seq expression analysis were used to identify the enriched pathway maps from the KEGG database (see procedures for details).
(C) Bar plots of naïve pluripotency markers (Kalkan et al., 2017) upregulated upon iMC-linker or CAezrin expression (RNAseq-derived, data from 3 independent experiments). All pairs (48 h vs. 48 h+Dox) are significant ($p<0.01$).
Modified from (Bergert, Lembo et al., 2020).

We finally tested the effect of iMC linker and CAezrin expression on naïve pluripotency by assessing global DNA methylation (DNAme). DNAme is a key marker of exit from pluripotency and cells typically undergo a transition from DNA hypomethylation (20-40 %) to hypermethylation (60-80 %) upon 2i/LIF withdrawal (Hackett et al., 2013) (Leitch et al., 2013). We found that the induction of iMC-linker or CAezrin expression significantly impaired acquisition of global DNA hypermethylation (Figure 3.22).

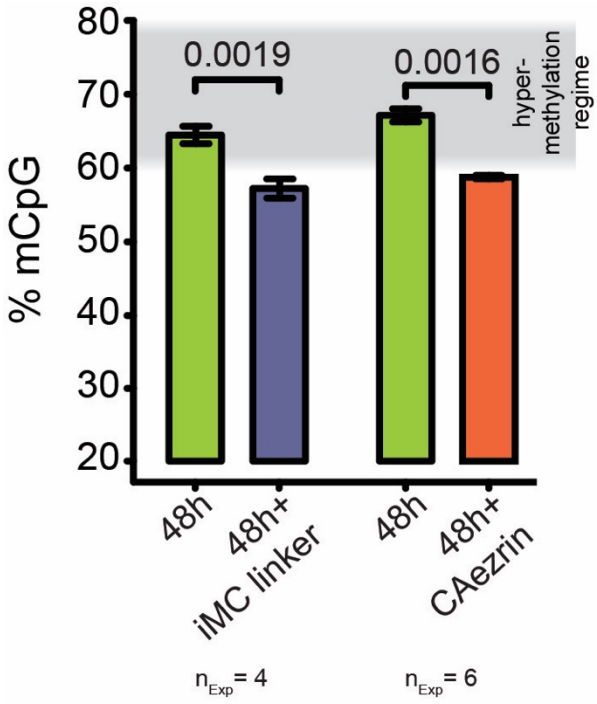

Figure 3.22. Preventing the reduction of MCA during exit from naïve pluripotency reduces the acquisition of global DNA methylation. Global DNA methylation levels of mESC Rex1-GFPd2 ind-iMC linker and ind-CAezrin cells plated for 48 h in N2B27 media or in N2B27+Dox media. Gray region depicts typical hypermethylation regime (60-80 %mCpG) acquired upon 2i/LIF withdrawal (Hackett et al., 2018). nExp: number of independent experiments. Error bars: SEM. p-values: Welch's t-test.
Modified from (Bergert, Lembo et al., 2020).

In conclusion, we found that forcing mESCs to keep high MCA values after removing 2i/LIF forces the cells to maintain naïve pluripotency features within their transcriptional and epigenetic landscapes. These results strongly indicate that MCA is an upstream regulator of the naïve-to-primed transition.

3.2.4. Differentiating mESCs expressing iMC linker or CAezrin retain naïve functional features of naïve cells

To further evaluate whether iMC linker- and CAezrin-expressing mESCs retain naïve pluripotency features despite the removal of 2i/LIF, we challenged the cells in functional pluripotency assays. First, we performed a re-plating assay,

which assesses the dissolution of the core pluripotency gene regulatory network by testing the ability of differentiating cells to survive under stringent 2i/LIF conditions (figure 3.23A) (Betschinger et al., 2013) (Cirera-Salinas & Ciaudo, 2017). In brief, mESCs are cultured in plain N2B27 medium to elicit exit from naïve pluripotency while simultaneously inducing the expression of the exogenous MCA linkers. After 48 h, N2B27 is replaced with 2i/LIF medium and the cells are incubated for 4-5 days. Since most of the primed cells cannot survive in 2i/LIF medium (Mulas et al., 2019), the lower the number of surviving colonies, the higher is the efficiency of the exit from naïve pluripotency. Notably, iMC linker- and CAezrin-expressing cells were able to generate 3-fold more colonies than their control counterparts expressing individual iMC linker components or only mCherry (figure 3.23B,C).

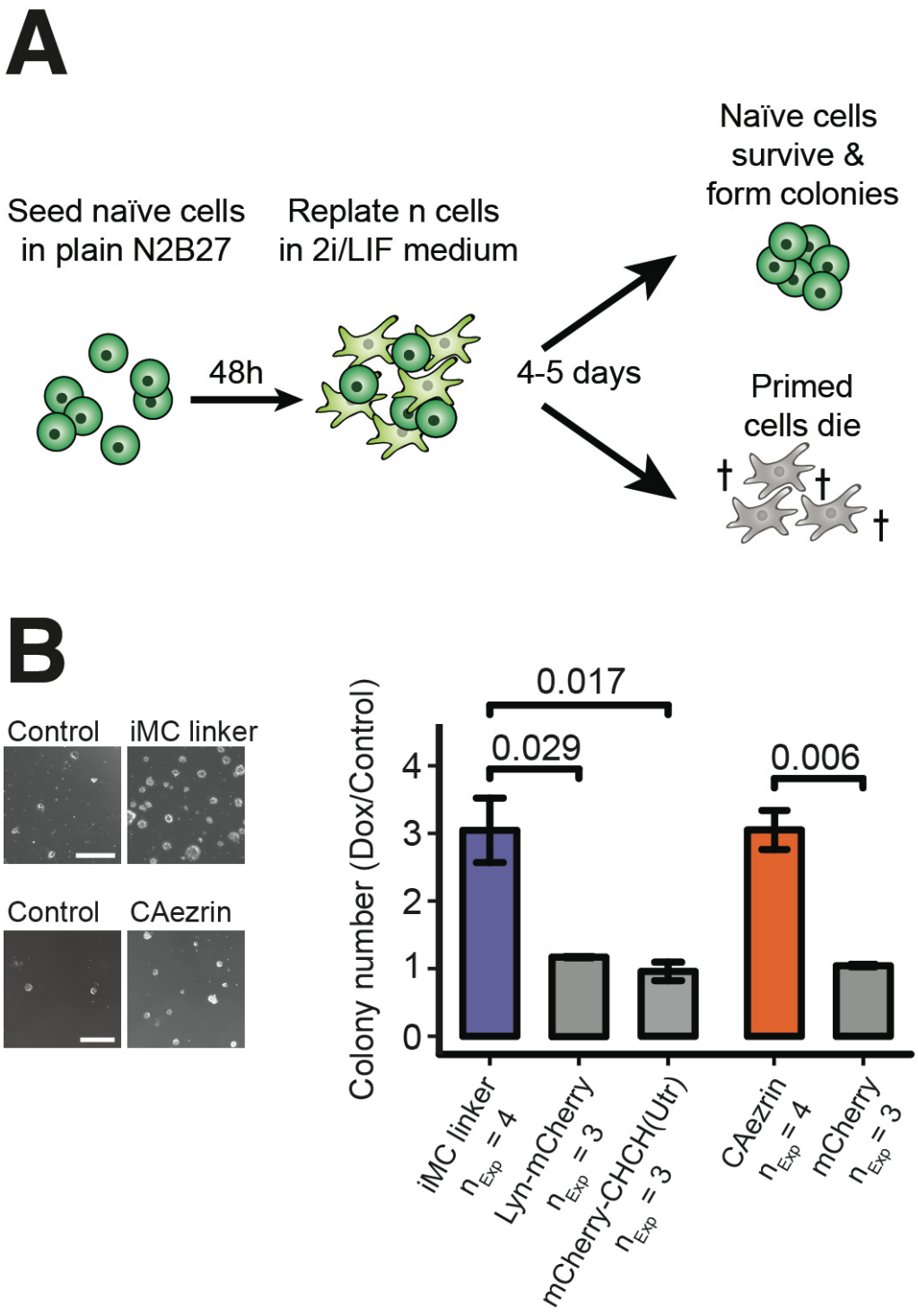

Figure 3.23. The ability of mESCs to survive in a re-plating assay is greatly enhanced by the expression of iMC linker or CAezrin.
(A) Schematic of the re-plating assay used to assess the pluripotency state.
(B) Representative images of the re-plating assay for mESC Rex1-GFPd2 ind-iMC linker and ind-CAezrin cells. Control: uninduced cells. Scale bar: 500 µm.

(C) Normalized colony number (Dox/Control) for mESC Rex1-GFPd2 ind-iMC linker, ind-Lyn motif-mCherry, ind-mCherry-CHCH(Utr), ind-CAEzrin and ind-mCherry cells re-plated after a 48 h exit in N2B27±Dox medium. Dox: induced cells. Control: uninduced cells. nExp: number of independent experiments. Error bars: SEM. p-value: Welch's t-test.
Modified from (Bergert, Lembo et al., 2020).

Finally, we investigated whether our findings are also relevant in more complex contexts, beyond the naïve-to-primed transition in cell culture. To-that-end, we tested the effect of expressing iMC linker or CAezrin during embryoid body formation, organoids where cells spontaneously differentiate into lineages of the three primary germ layers (figure 3.24A) (Koike et al., 2007). We induced the expression of our constructs for the first 48 h of embryoid body formation and assessed the expression of general and naïve pluripotency markers (Kalkan et al., 2017) as well as differentiation markers, by RNA-seq after 2 additional days. Similarly to what observed in 2D culture (figure 3.21), we observed that the expression of iMC linker or CAezrin is sufficient to maintain the expression of the naïve transcription network and delays the upregulation of lineage specific markers (figure 3.24B).

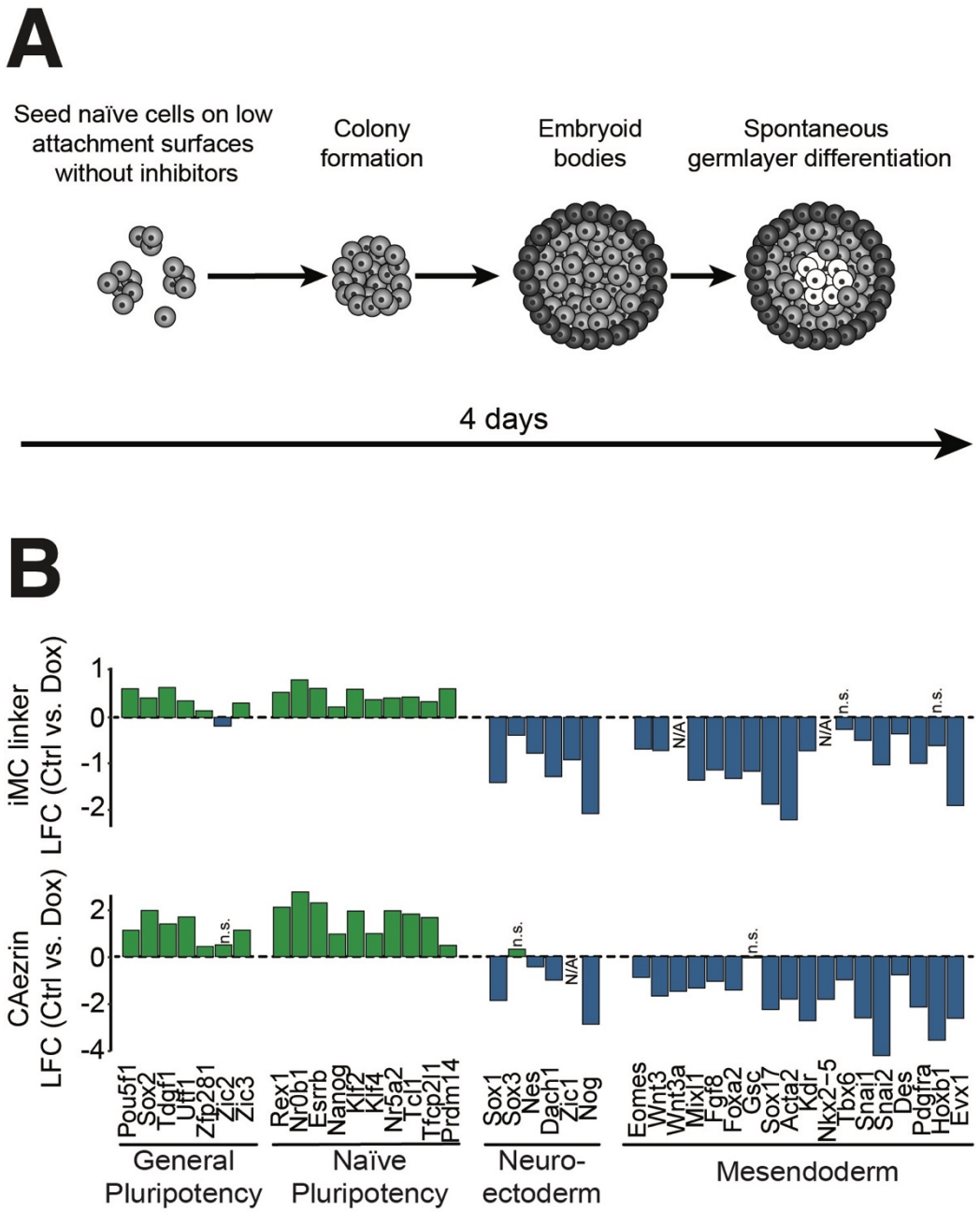

Figure 3.24. iMC linker or CAezrin expression during the formation of embryoid bodies delays the exit from naïve pluripotency and the upregulation of lineage specific markers.

(A) Schematic of embryoid body formation.

(B) RNAseq-derived mRNA fold-changes of general and naïve pluripotency markers (Kalkan et al., 2017) and markers for neuroectoderm and mesendoderm formation at day 4 of embryoid body differentiation for mESC Rex-GFPd2 ind-iMC linker (top) or ind-CAezrin (bottom) cells (data from 4 independent experiments). Green color indicates higher and blue color indicates lower expression in induced cells dissociated from embryoid bodies. N/A: expression

below detection limits. All log-fold-changes (LFC) are significant ($p<0.01$) except otherwise noted (n.s.).
Modified from (Bergert, Lembo et al., 2020).

3.2.5. MCA reduction is not sufficient to elicit exit from naïve pluripotency

In the previous section we showed that MCA reduction is necessary for the naïve-to-primed transition. To assess whether MCA reduction is also sufficient to drive this process, we engineered an mESCs line which expresses DNezrin [a dominant negative variant of Ezrin,T567A (Yonemura et al., 1999)] in an inducible manner (figure 3.25A). DNezrin significantly reduces MCA in naïve cells (figure 3.25B). Interestingly, DNezrin expression does not lead to the downregulation of the naïve markers Rex1 and Nanog (figure 3.25C), suggesting that MCA reduction is not sufficient to elicit the transition to the primed state. The experimentally-induced reduction in MCA might still favor the transition by accelerating it after its initiation. To evaluate this hypothesis, we dynamically monitored Rex1 expression during the exit from naïve pluripotency (figure 3.25D). We found no significant difference in Rex1 variation of expression between DNezrin- and mCherry-expressing cells. Consistently, the colony number in the re-plating assay was comparable between these two cell lines (figure 3.25E).

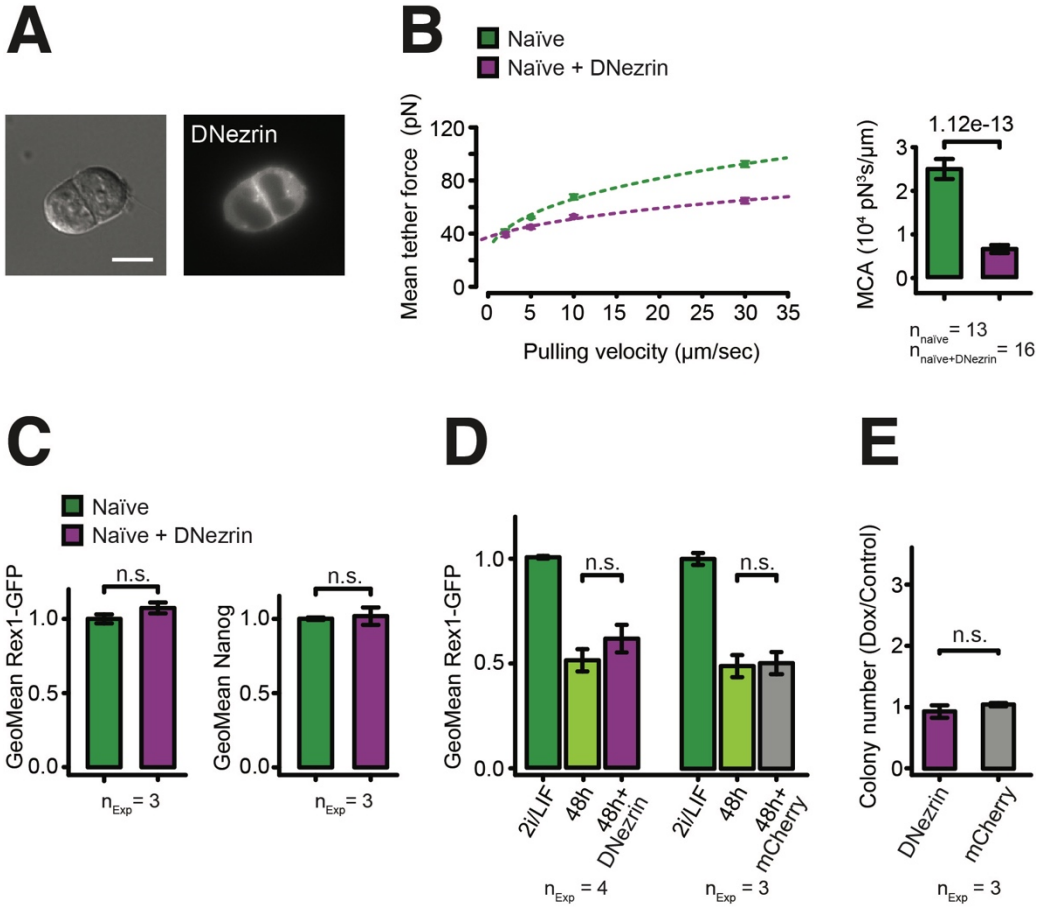

Figure 3.25. DNezrin-dependent reduction in MCA is not sufficient to elicit exit from naïve pluripotency.

(A) Representative brightfield (DIC) and fluorescent images of mESC Rex1-GFPd2 ind-DNezrin cells expressing DNezrin-mCherry in 2i/LIF+Dox medium.

(B) [Left] Force-velocity curve from dynamic tether pulling on mESC Rex1-GFPd2 ind-DNezrin cells in 2i/LIF medium and during exit from pluripotency in N2B27±Dox medium at 48 h. Data points are mean tether force f ± SEM at 2, 5, 10 and 30 µm/s pulling velocity. n: number of cells analyzed in 3 independent experiments. [Right] Mean and standard deviation of the MCA parameter a obtained from Monte-Carlo-based fitting. p-value: Z test.

(C) [Left] Normalized GFP geometric mean intensities for mESC Rex1-GFPd2 ind-DNezrin cells plated for 48 h in 2i/LIF or in 2i/LIF+Dox medium. nExp: number of independent experiments. Error bars: SEM. p-values: Welch's t-test. [Right] Normalized geometric mean intensities of Nanog immunofluorescence levels for mESC Rex1-GFPd2 ind-DNezrin cells plated for 48h in 2i/LIF or in 2i/LIF+Dox medium. nExp: number of independent experiments. Error bars: SEM. p-values: Welch's t-test.

(D) Normalized GFP geometric mean intensities for mESC Rex1-GFPd2 ind-DNezrin and ind-mCherry cells in 2i/LIF medium and during exit from naïve pluripotency in N2B27±Dox medium at 48 h. nExp: number of independent experiments. Error bars: SEM. p-value: Welch's t-test.

(E) Normalized colony number (Dox/Control) mESC Rex1-GFPd2 ind-DNezrin and ind-mCherry cells re-plated after a 48 h exit in N2B27±Dox medium. nExp: number of independent experiments. Control: uninduced cells. Error bars: SEM. p-value: Welch's t-test.
Modified from (Bergert, Lembo et al., 2020).

Together, these findings show that DNEzrin expression is not sufficient to speed up the naïve-to-primed transition and suggest that MCA acts as a gate, not a driver, of the exit from naïve pluripotency.

3.2.6. Final discussion of part B

In part B of my thesis, I described our study on the role of MCA in naïve-to-Primed transition of mESCs. Thanks to the use of iMC linker, we showed that naïve cells need to reduce the linkage of the plasma membrane to the underlying actomyosin cortex in order to differentiate into primed cells. Importantly, as indicated by experiments involving DNezrin, the reduction in MCA is necessary but not sufficient to elicit this process, suggesting that MCA may acts as a checkpoint prior to the onset of the transition, rather than a driver of differentiation.

Our findings are in line with several studies that have linked mechanical properties – such as substrate stiffness, cortical contractility, fluid flow, cyclic stress, compression or luminal pressure – to *in vitro* and *in vivo* cell differentiation (Aguilar et al., 2016) (Chan et al., 2019) (Chowdhury, Na, et al., 2010) (Cohen & Chen, 2008) (Engler et al., 2006) (Farge, 2003) (Maître et al., 2016) (North et al., 2009) (Pathak et al., 2014) (J. Li et al., 2018). Albeit the importance of MCA in embryonic stem cells differentiation has to be determined *in vivo*, several clues point toward that direction. As discussed in greater details in section *3.3.* and preliminary tested in section *3.3.4.*, the MCA linker Ezrin re-localizes at the apical surface of the blastomeres in the 8-cell mouse embryo. These Ezrin-rich apical domains are necessary and sufficient for the first lineage segregation in early mouse embryos (Korotkevich et al., 2017). Furthermore,

experimental abrogation of the accumulation of Ezrin in the apical domains disrupt the development of the embryo (Dard et al., 2004). A more insightful approach might the development and use of an optogenetic version of iMC linker (discussed in section *3.1.5.1.*). Such a tool, would have sufficient subcellular space resolution to investigate the role of the asymmetric MCA within a blastomere after the formation of the apical domain.

3.3. PART C: Unravelling MCA-dependent regulation of cortex mechanics

A recurring theme throughout this thesis is the little understanding we have of MCA, especially compared to other elements and mechanical properties of the animal cell surface. A particularly striking lack of knowledge lies on the relationship between MCA and the cell cortex. Indeed – while a vast literature shows that MCA affects mechanical properties of the PM such as apparent tension and thermal fluctuations (Jianwu Dai & Sheetz, 1999) (Alert et al., 2015) – little effort has been made to unveil if and how MCA influences the cell cortex and vice versa. Notwithstanding, the existence of a reciprocal regulation has been hinted by several biological observations, according to which cell processes regulated by cortex mechanics are also characterized by a suspicious re-localization and coordinated activity of ERM proteins and other MCA linkers.

A first example of such biological processes is cytokinesis, the physical cleavage of daughter cells that occurs at the end of mitosis (figure 3.26A) (reviewed in (Yinan Liu & Robinson, 2018)). Cytokinesis starts with the formation of the cytokinetic actin ring at the equatorial plane, which occurs during the segregation of the sister chromatids (Satterwhite & Pollard, 1992) (reviewed in (Ramkumar & Baum, 2016)). This structure is assembled through localized myosin-II-dependent contractility, which generates an actin flow toward the equatorial plane, and through Formin-dependent *de novo* nucleation of actin filaments (Reymann et al., 2016) (Severson et al., 2002). Subsequently, the cytokinetic ring contracts and forms a furrow which in turn constricts until the daughter cells completely separate (figure 3.26A) (reviewed in (Satterwhite & Pollard, 1992)).

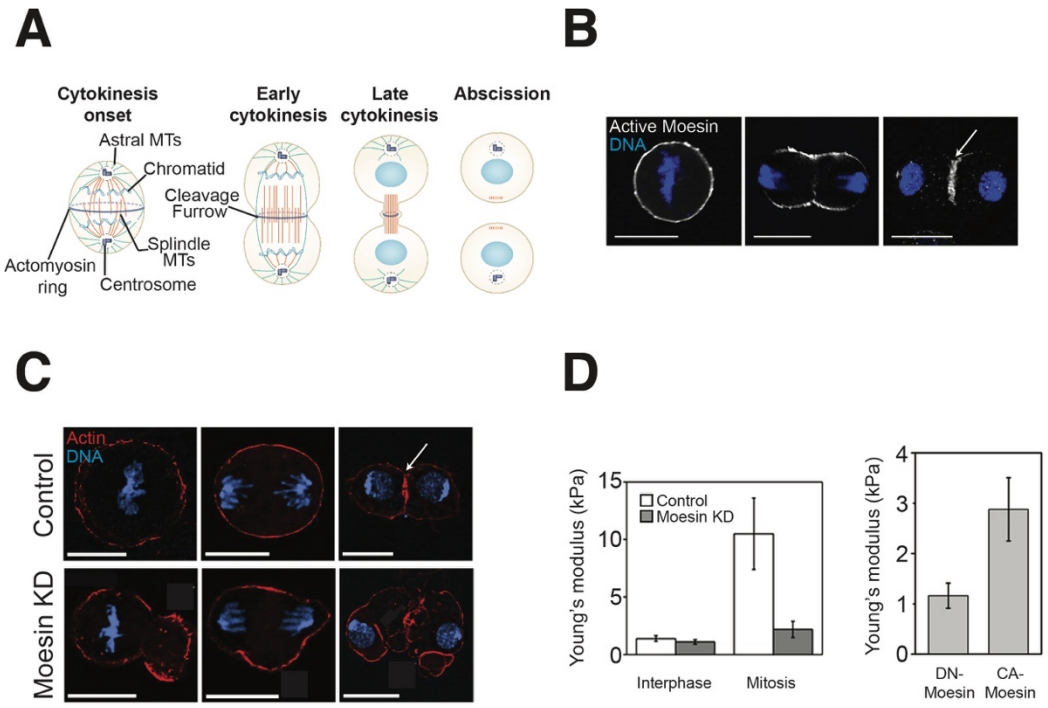

Figure 3.26. Dynamics and functions of Moesin in cytokinesis.
(A) Schematic of cytokinesis in animal cells. Modified from (Lens & Medema, 2019).
(B) Active Moesin re-localizes to the equatorial plane at the onset of cytokinesis in wild type Drosophila C2 cells. White arrow: cytokinetic ring. Scale bar: 10 µm. Modified from (Carreno et al., 2008).
(C) Moesin downregulation in Drosophila C2 cells via knock down (KD) results in the absence of a physiological cytokinetic ring and in cell division disruption. White arrow: cytokinetic ring. Scale bar: 10 µm. Modified from (Carreno et al., 2008).
(D) [Left] Moesin downregulation in mitotic Drosophila C2 cells via knock down (KD) leads to a reduction of cell surface stiffness in mitosis. [Right] Ectopic expression of a dominant negative version (DN-) or a constitutively active version of (CA-) of Moesin in mitotic Drosophila C2 cells results in a decrease and an increase in cell surface stiffness respectively. Modified from (Kunda et al., 2008).

The engagement of MCA linkers in cytokinesis, has been shown by two parallel studies carried out using Drosophila S2 cells (Carreno et al., 2008) (Kunda et al., 2008). Active Moesin, the only ERM protein in Drosophila, re-localizes to the equatorial plane at the onset of cytokinesis and becomes progressively restricted to the cleavage furrow during the cytokinetic ring constriction (figure 3.26B). Moesin downregulation at the translational level via RNA interference results in the lack of formation of the cytokinetic ring and in the disruption of cell division

(figure 3.26C). Furthermore, cell surface stiffness, which depends primarily on cortical mechanics (see section *3.3.1.*), is dramatically changed in mitotic C2 cells upon a reduction in Meosin activity via downregulation or ectopic expression of a dominant negative (DN-) or a constitutively active version of Moesin (figure 3.26D). These observations strongly suggest a role for the MCA linker in the regulation of cortex mechanics during cytokinesis.

A second intriguing correlation between MCA linker activity and a cortex mechanics-regulated process has been observed during the early phases of mouse embryo development. At the 8-cell stage, the embryo undergoes compaction and the cells become polarized (figure 3.27A) (reviewed in (Johnson, 2009)). Cell polarization is characterized by the formation of an apical domain at the cell contact-free surface of the blastomeres; this is considered as the first fate specification event during mouse embryo development. In fact, at the next round of division, only half of the cells inherit the apical domain and become committed to the trophectoderm, while the other cells form the actual embryo, at this stage referred to as the inner cell mass (figure 3.27A). Several groundbreaking studies have shown that asymmetric division is driven by positional information and asymmetric contractility within each blastomere (Maître et al., 2016) (Maître et al., 2015) (reviewed in (M. Zhu & Zernicka-Goetz, 2020)). In brief, apicobasal polarization is instructed by the position of the cell-cell junctions, which force the formation of apical domains at the cell contact-free surfaces of the blastomeres (figure 3.27B top). The apical domain, in turn, reduces the actomyosin contractility in the domain of the cortex beneath (figure 3.27B center). The resulting contractility gradient governs the orientation of the cell division plane leading to the asymmetric inheritance of the apical domain (figure 3.27B bottom).

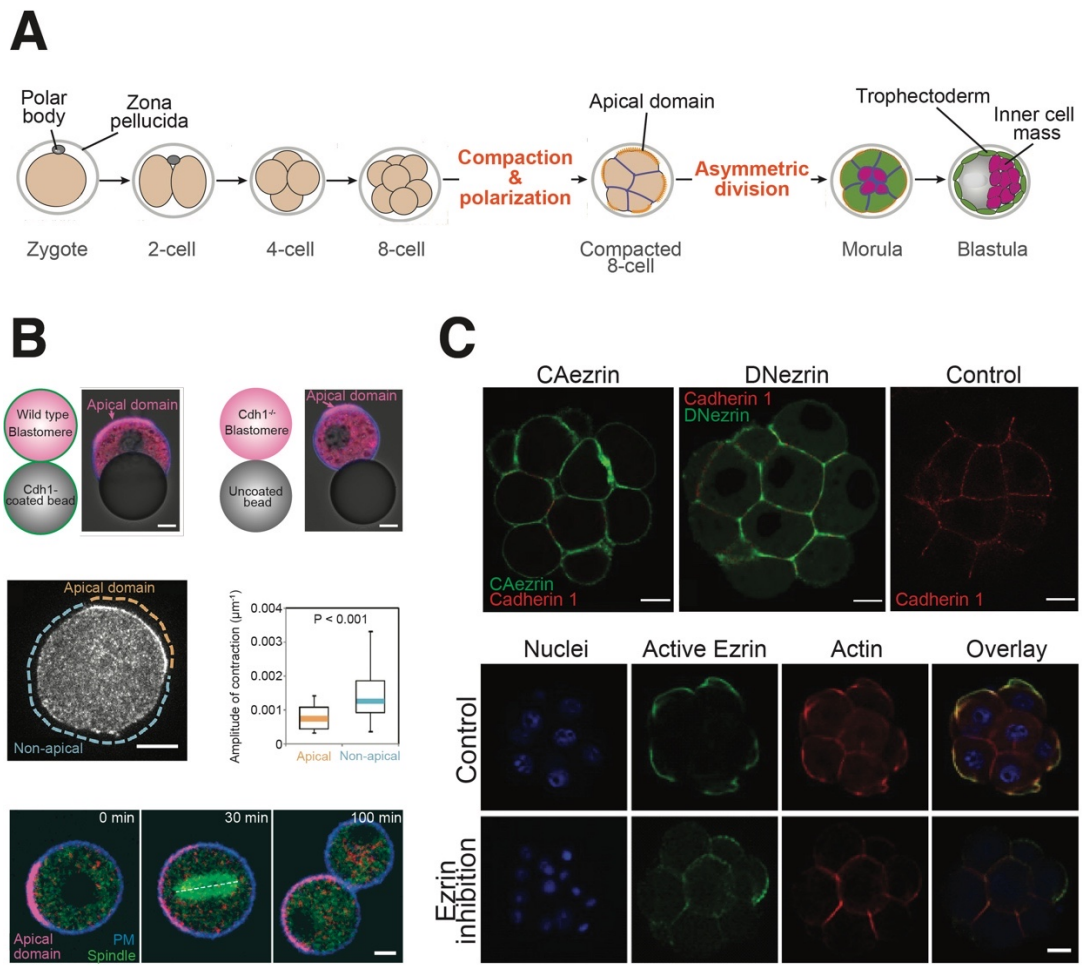

Figure 3.27. Ezrin functions in the first fate specification event during mouse embryo development.

(A) Schematic of the early phases of mouse embryo development. Modified from (Chazaud & Yamanaka, 2016).

(B) Key processes that lead to the first fate specification event during mouse embryo development. The blastomeres showed herein have been isolated from the non-compacted 8-cell embryos. Scale bars: 10 µm. [Top] Positional information determines localization of the apical domain which always form at the antipode of the PM domain in contact with the bead. This process is independent of Cadherin 1 (Cdh1). Modified from (Korotkevich et al., 2017). [Center]. The apical domain controls the amplitude of cortex contractility. Modified from (Maître et al., 2016). [Bottom] The apical domain governs the orientation of the division plane through the generation of differential contractility in the cortex. Dashed line: spindle. Modified from (Korotkevich et al., 2017).

(C) [Top] 8/16-cell mouse embryos expressing either CAezrin or DNezrin. Scale bar 10 µm. Modified from (Dard et al., 2004). [Bottom] Inhibition of Ezrin activation at the 8-cell stage abolishes cortex repolarization. Scale bar: 20 µm. Modified from (H. Liu et al., 2013).

The mechanism through which the apical domain controls cortex contractility is still unclear. Interestingly, the ERM protein Ezrin localizes to the apical domain and is often used as the main marker of this structure (Louvet et al., 1995). Consistent with a functional engagement of the protein in the apical domain, ectopic expression of CAezrin or DNezrin disrupts embryo development at the 8-cell stage, with the former preventing embryo compaction and the latter inhibiting blastomere polarization (figure 3.27C top) (Dard et al., 2001) (Dard et al., 2004). Finally, inhibition of Ezrin activation at the 8-cell stage results in striking failure of apical enrichment of actin filaments – strongly suggesting a role for MCA in the organization of the asymmetric cortex of the polarized blastomeres (figure 3.27C bottom) (H. Liu et al., 2013).

The two case studies described above, illustrate clearly the importance of shedding light on the relationship between MCA and cortex mechanics. In this part of my thesis, I am presenting the preliminary results of our attempts to cover this knowledge gap.

3.3.1. MCA as novel regulator of cell cortex stiffness

In order to evaluate a putative role of MCA in regulating cortex mechanics, we measured cell surface stiffness by nano-indenting iMC linker expressing cells with AFS (figures 3.28A,B). Cell surface stiffness can be defined as a coefficient which quantitatively describes the deformation of an object upon application of a force. Despite the similarities to elastic moduli (see section *1.2.1.2.*), stiffness is an effective parameter, and hence depends not only on the material properties of the object, but also on its geometric features and the nature of the deformation (Pharr et al., 1992). More specifically, cell surface stiffness depends on the elastic moduli of the PM and the cortex, on cell surface tension and on cell geometry (Salbreux et al., 2012). Several studies have shown that the cell cortex dominates the mechanical response during nano-indentation

experiments, therefore cell surface stiffness can be approximated to cortex stiffness, which encapsulates both cortical tension and elasticity (Rotsch & Radmacher, 2000) (Rosenbluth et al., 2006) (Nawaz et al., 2012).

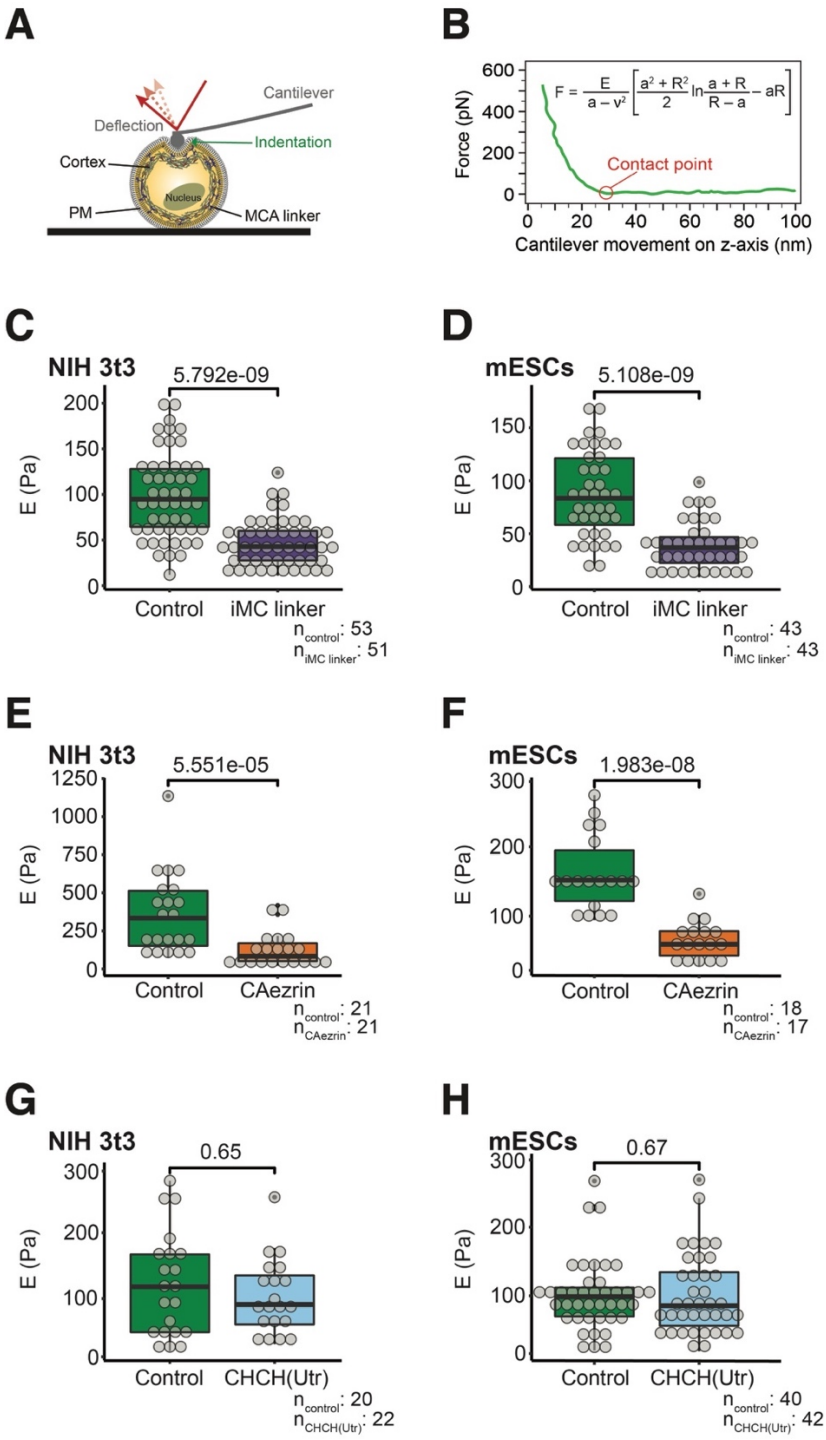

Figure 3.28. Increasing MCA leads to a reduction in cell cortex stiffness.

(A). Schematic of the indentation experiment performed with AFS.
(B) Exemplary force-distance curve. Equation: Hertz model for spherical indenters (Lin et al., 2009). E: apparent Young's modulus; ν: Poisson's ratio; a: displacement; R: indenter radius.
(C) Cell cortex stiffness of spherical inducible iMC linker-NIH 3t3 (clone gamma). E: apparent Young's modulus. Control: uninduced cells. Gray dots: single cells. n: number of cells analyzed in 5 independent experiments. p-value: Mann-Whitney U-test.
(D) Cell cortex stiffness of inducible iMC linker-mESCs (clonal line). E: apparent Young's modulus. Control: uninduced cells. Gray dots: single cells. n: number of cells analyzed in 4 independent experiments. p-value: Mann-Whitney U-test. (E) Cell cortex stiffness of spherical NIH 3t3 constitutively expressing CAezrin. E: apparent Young's modulus. Control: wild type cells. Gray dots: single cells. n: number of cells analyzed in 2 independent experiments. p-value: Mann-Whitney U-test.
(F) Cell cortex stiffness of inducible CAezrin-mESCs (clonal line). E: apparent Young's modulus. Control: uninduced cells. Gray dots: single cells. n: number of cells analyzed in 3 independent experiments. p-value: Mann-Whitney U-test.
(G) Cell cortex stiffness of spherical inducible CHCH(Utr)-NIH 3t3 (clonal line). E: apparent Young's modulus. Control: uninduced cells. Gray dots: single cells. n: number of cells analyzed in 2 independent experiments. p-value: Mann-Whitney U-test.
(H) Cell cortex stiffness of inducible CHCH(utr)-mESCs (clonal line). E: apparent Young's modulus. Control: uninduced cells. Gray dots: single cells. n: number of cells analyzed in 4 independent experiments. p-value: Mann-Whitney U-test.
In all cases: 3T3 cells were micropatterned on 20um FN patches to inforce a spherical geometry. mESC are round and thus required no micropatterning to obtain a spherical geometry

We measured cortex stiffness on NIH 3t3 and mESC clonal lines expressing iMC linker in an inducible manner (figure 3.28C,D). Strikingly, increasing MCA through the expression of iMC linker leads to a strong reduction in cell cortex stiffness. CAezrin expression phenocopies iMC linker further corroborating this novel regulatory function of MCA on cortex mechanics (figure 3.28E,F). Importantly, the solely expression of the actin-binding component of iMC linker is not sufficient to affect cell cortex stiffness (figure 3.28G,H). Consequently, the phenotype observed in figure 3.28C-F is not the result of alterations of cortex dynamics due by the direct binding of the actin-binding domains to filamentous actin.

We then asked whether the reduction in cell cortex stiffness is dependent on the concentration of iMC linker used, and if so how does that relationship look like. To-that-end, we generated NIH 3t3 clonal lines expressing different levels of iMC linker upon induction (figure 3.29A) and measured cortical stiffness with AFS. Importantly, the different clones display different basal values of cortical stiffness owing to their specific characteristics (figure 3.29B). Therefore, to allow comparisons between the different clones, we normalized the cortical stiffness reductions by dividing the median of the apparent Young's moduli of each induced cell, to the median apparent Young's modulus of the uninduced population. By plotting the softening ratios against the expression levels of iMC linker of the different clone, we found that the degree of reduction in cortical stiffness negatively correlates with iMC linker density (figure 3.29C).

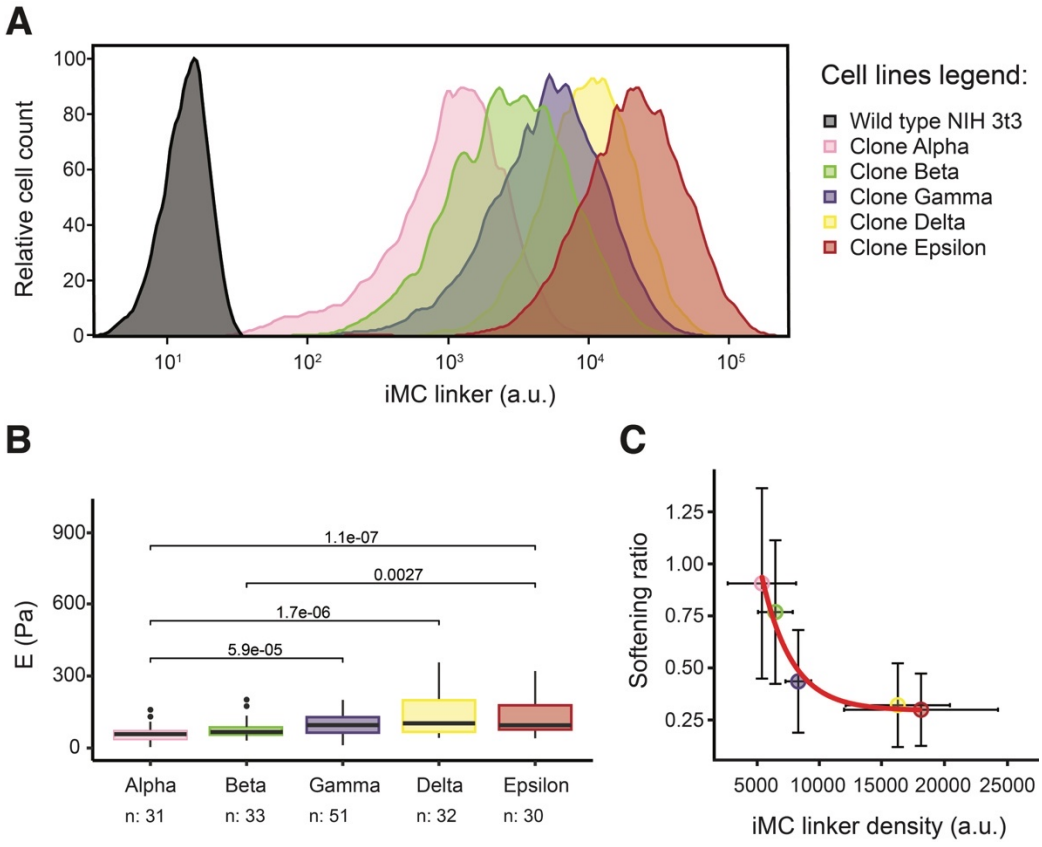

Figure 3.29. iMC linker reduces cell cortex stiffness in a density-dependent manner.

(A) iMC linker expression level upon induction of the inducible iMC-linker NIH 3t3 clonal lines selected; determined by flow cytometry.
(B) Cell cortex stiffness of "spherical" uninduced iMC linker-NIH 3t3 clonal lines. E: apparent Young's modulus. n: number of cells analyzed in 3 (Alpha, Beta, Delta, Epsilon) and 5 (Gamma) independent experiments. Data used also in figure 3.29C. p-value: Mann-Whitney U-test; showed only statistically significant p-values.
(C)Cortical stiffness reduction of the inducible iMC linker-NIH 3t3 clonal lines shown in A, over their respective iMC linker density.
[x-axis]: iMC linker geometric mean intensities for induced inducible iMC linker-NIH 3t3 cells. Data analyzed in 3 independent experiments. Error bars: standard error of the mean.
[y-axis]: cell cortex stiffnesses of the inducible iMC linker-NIH 3t3 clonal lines shown in A. Cortex stiffness of each clone expressed as softening ratio, calculated as the median of the apparent Young's moduli of each induced cell, normalized to the median apparent Young's modulus of the uninduced population. Clone Alpha: 31 induced and 31 uninduced cells analyzed in 3 independent experiments. Clone Beta: 32 induced and 33 uninduced cells analyzed in 3 independent experiments. Clone Gamma: 53 induced and 51 uninduced cells analyzed in 5 independent experiments. Same data showed in figure 3.28C. Clone Delta: 34 induced and 32 uninduced cells analyzed in 3 independent experiments. Clone Epsilon: 26 induced and 30 uninduced cells analyzed in 3 independent experiments. Red line: simple exponential decay fitted with the least-squares method ([softening ratio] = $a^{-[\text{iMC linker density}]} + c$). Residual standard error: 0.0639.

Taken together these results show that MCA influences cortex mechanics by negatively regulating cortical stiffness. Importantly, we found that the rate of reduction in cortical stiffness positively correlates with the iMC linker density at the cell surface.

3.3.2. MCA affects both cortical tension and cortex elasticity

Cortical stiffness depends on both the elastic and viscous component of the cell cortex and is influenced by a combination of the cortex elastic moduli and cortical tension. Aiming to further disentangle the regulatory role of MCA on cortex mechanics, we measured independently cortical tension and cortex elasticity in NIH-3t3 cells expressing iMC linker (figure 3.30). Cortical tension was

measured through micropipette aspiration aspiration in collaboration with Joe Chii Chan at EMBL (figure 3.30A): by modeling cells as liquid droplets surrounded by a thin elastic membrane (A. Yeung & Evans, 1989), the pressure required to aspirate a spherical protrusion into the micropipette depends on the radii of the pipette and the cell, and on cell surface tension (see equation in figure 3.30A). The contribution of PM tension to cell surface tension is negligible, and hence the latter mechanical property can be used as a proxy for cortical tension.

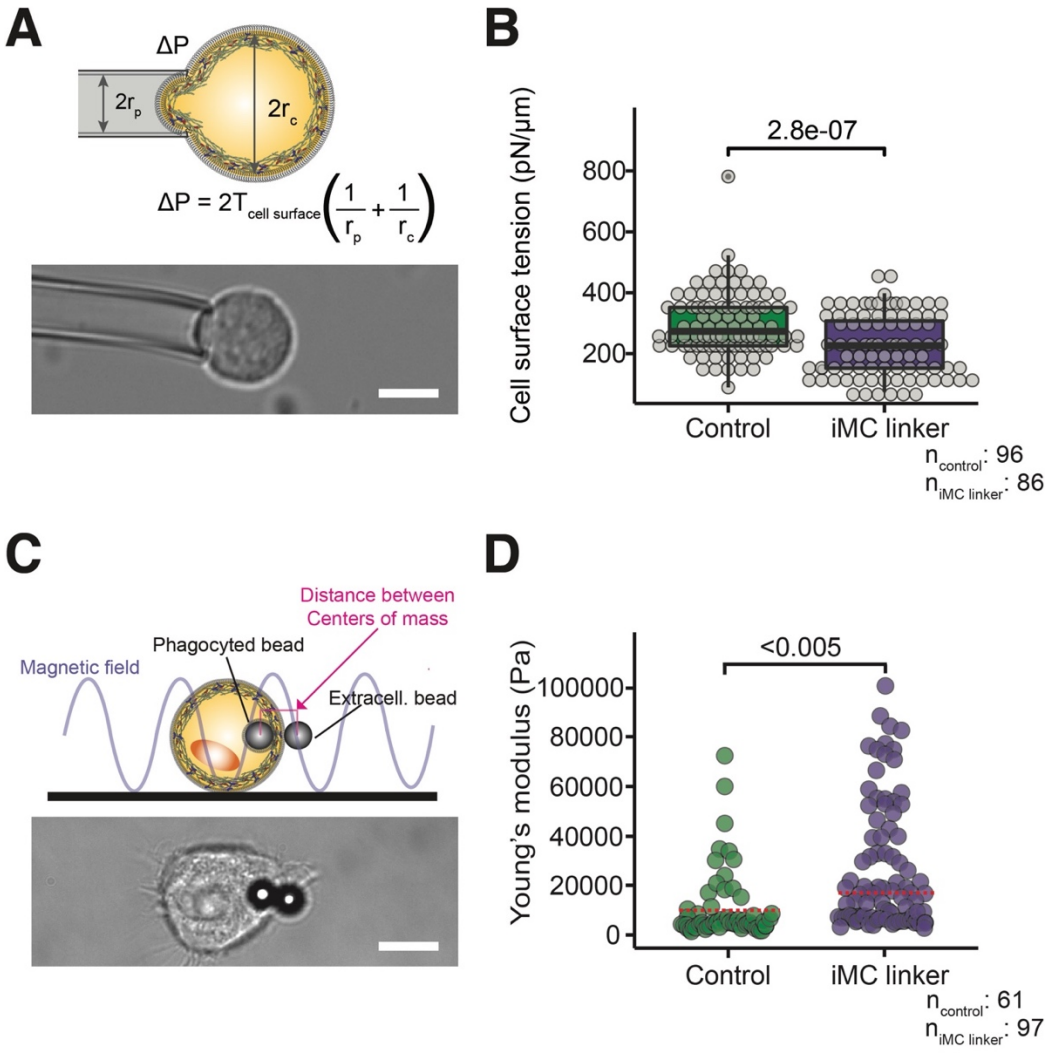

Figure 3.30. iMC linker-dependent increase in MCA leads to a reduction in cortical tension and an increase in cortical elasticity.

(A) [Top] Schematic of micropipette aspiration. Equation: law of Laplace. P: pressure. r_p: radius of the pipette, r_c: radius of the cell, $T_{cell\ surface}$: cell surface

tension. [Bottom] Representative bright field image of NIH 3t3 cell undergoing micropipette aspiration.

(B) Mean cell surface tension (~cortical tension) of expressing (iMC linker) and uninduced (Control) NIH 3t3 cells (clone gamma) in suspension. Gray dots: single cells. n: number of cells analyzed in 4 independent experiments. p-value: Welch's t-test.

(C) [Top] Schematic of magnetic pinching. [Bottom] Representative bright field image of adherent NIH 3t3 cell undergoing micropipette aspiration.

(D) Young's elastic modulus of cell cortex fitted from compression assays. n: number of compressions from 11 iMC linker expressing cells 7 uninduced control cells. p-value: Mann-Whitney U-test.

We found that iMC linker-expressing cells have a lower cortical tension than their uninduced counterparts (figure 3.30B), in agreement with the MCA-dependent reduction in cortical stiffness observed with AFS (figure 3.29).

As discussed in section *1.2.2.2.* of the introduction, cortical tension results from the contribution of different phenomena: the architecture of the cortex, the crosslinking degree of the actin filaments, and myosin-II-dependent contractility. To preliminary screen which of these components is responsible for the MCA-dependent reduction in cortical tension, we measured cell cortex elasticity, which is mainly determined by the connectivity within the cortex. We used magnetic pinching, a method recently developed in Mathieu Piel's laboratory (Laplaud et al., 2020). In brief: two superparamagnetic microbeads, one in solution and one phagocyted by the cell, are brought next to the cortex through the application of a magnetic field (figure 3.30C). By measuring the distance between the centers of the two beads at different intensities of magnetic field – which determine the attractive force between the two beads – the local Young's modulus of the cell cortex can be derived (Dimitriadis et al., 2002). We found that iMC linker expressing cells display a higher Young's modulus than control cells (figure 3.30D).

Taken together, these results show that MCA influences cell cortex stiffness by negatively regulating cortical tension and positively regulating cortex elasticity.

3.3.3. Does MCA regulate cortex architecture?

In the previous section, I have shown an iMC linker-dependent increase in MCA leads to a reduction in cortical tension and a simultaneous increase in the Young's modulus of the cortex. This complex behavior is probably the result of global changes in the cortex architecture. To assess this hypothesis, we first employed the magnetic pincher (Laplaud et al., 2020) to measure the thickness of the cortex upon expression of iMC linker. We found no significant difference between cortexes of induced and uninduced cells (figure 3.31).

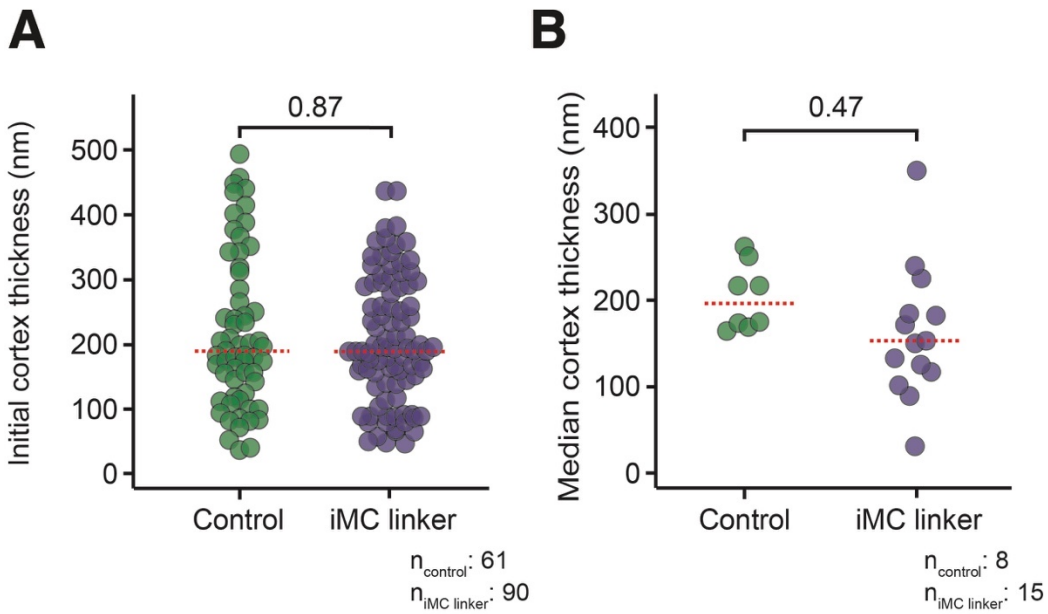

Figure 3.31. iMC linker expression does not lead to a change in cortex thickness.
(A) Initial thickness of the cortex fitted from compression assays. n: number of compressions from 11 iMC linker expressing cells 7 uninduced control cells. p-value: Mann-Whitney U-test.
(B) Median thickness of the cortex during constant magnetic field experiments with 10 mT. For each value the cortex was monitored for 5 min. n: number of cells analyzed in 3 independent experiments. p-value: Mann-Whitney U-test.

Next, we aimed at visualizing the cortex architecture through cryo-electron tomography in collaboration with the Julia Mahamid's laboratory at EMBL. To mimic the same conditions used in the nano-indentation experiments, we micropatterned gold mesh grids to force the 3t3 cells to acquire a spherical

shape (figure 3.32A left); we then confirmed that iMC linker-dependent reduction in cortical stiffness is reproduced even in this experimental setup (3.32A right). Importantly, micropatterning was designed to obtain cell pairs so that, upon snap freezing, the two cells would be in close proximity to each other but without forming cell adhesions (figure 3.32B top). The goal of this setup was to provide mechanical support to the side of the cells next to each other, which is essential to preserve the integrity of the lamella during milling (figure 3.32B bottom).

Figure 3.32 C, shows representative tomograms obtained from uninduced control (left) and iMC linker-expressing (right) cells. To determine cortical architecture, actin filaments segmentation is a critical step. Currently, despite the acquisition of a large number of tomograms from a large number of cells, our understanding of the cortex architecture is limited by our ability to segment actin filaments; manual segmentation has provided some insights (figure 3.32C bottom) but automation will be key in the future. To that end, we are currently training a neural network. Owing to the limited number of tomograms we have managed to segment so far, we cannot draw conclusions yet from the cryo-ET data. Nevertheless, by analyzing directly the tomograms, it is possible make some hypothesis, which will be discussed in the final discussion (section 3.3.4).

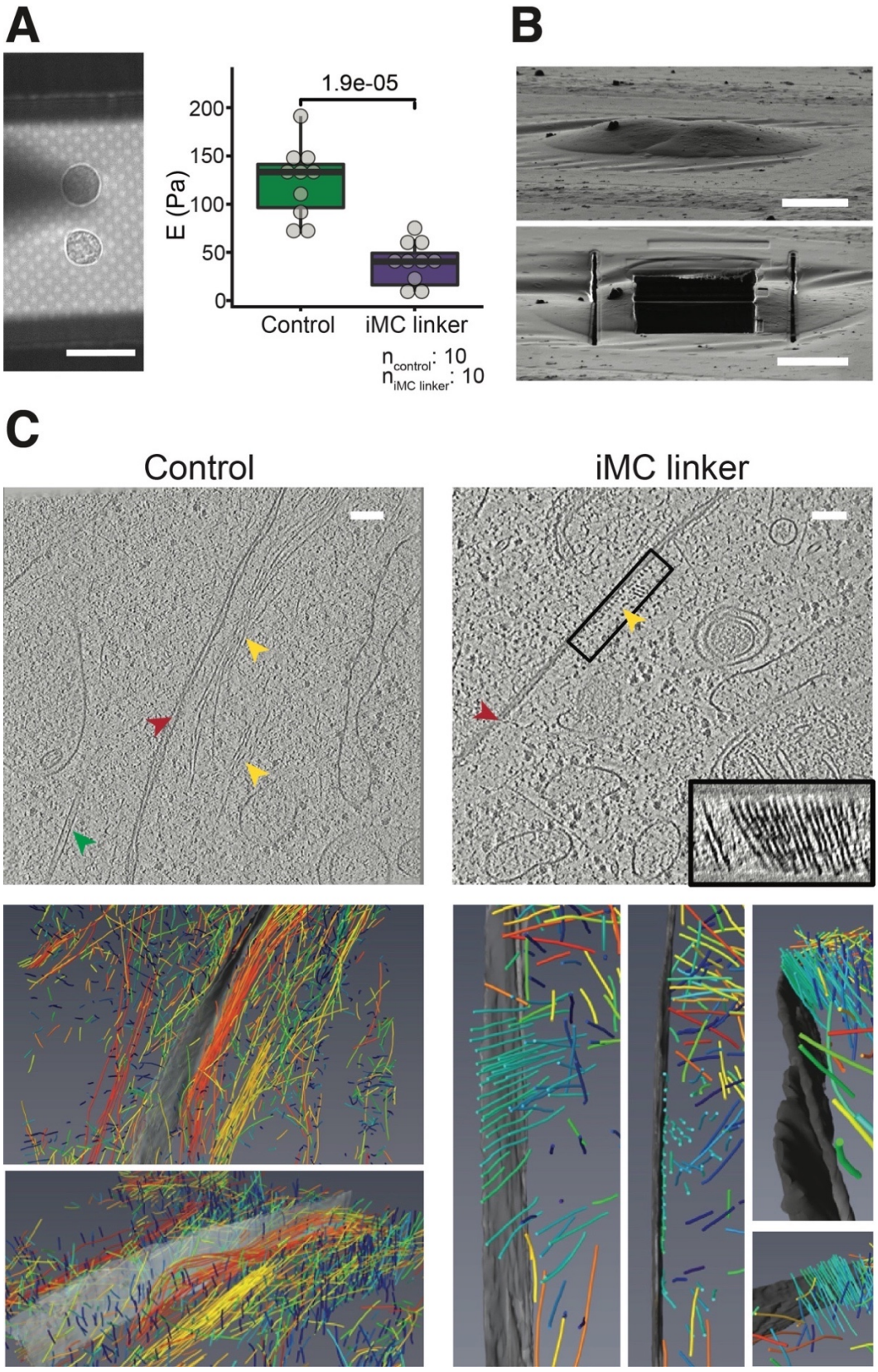

Figure 3.32. Visualization of the cell cortex architecture through cryo-electron tomography.

(A) [Left] Representative bright field image of “spherical” inducible iMC linker-NIH 3t3 (clone gamma) cell pair seeded on a gold EM mesh grid. Scale bar: 10 µm. [Right] Cell cortex stiffness of spherical inducible iMC linker-NIH 3t3 (clone gamma) seeded on gold EM mesh grids. E: apparent Young’s modulus. Control: uninduced cells. Gray dots: single cells. n: number of cells analyzed in 2 independent experiments. p-value: Mann-Whitney U-test.
(B) [Top] Representative scanning electron microscopy image of spherical inducible iMC linker-NIH 3t3 (clone gamma) seeded on gold EM mesh grids after snap freezing. Scale bar: 10 µm. [Bottom] Representative scanning electron microscopy image of a lamella obtained from spherical inducible iMC linker-NIH 3t3 (clone gamma) seeded on gold EM mesh grids. Scale bar: 10 µm.
(C) [Top] Representative cryo-EM tomograms of the cell surface of “spherical” inducible iMC linker-NIH 3t3 (clone gamma) cell pair seeded on a gold EM mesh grid. Scale bar: 100 nm. Yellow arrow heads: actin filaments. Red arrow heads: PMs. Green arrow heads: microtubule. [Bottom] Outcome of the segmentation of cortical actin filaments of the tomogram in C-top. Gray shade: PMs. Color code: filaments orientation.

3.3.4. Final discussion of part C

In the past two decades, a large number of studies have shown the pivotal roles of the cell cortex and its mechanics in a wide plethora of biological processes in animal cells and tissues (reviewed in (Clark et al., 2014) (Chalut & Paluch, 2016) (Chugh & Paluch, 2018)). In light of the importance of this subcellular structure, the community of scientists interested in cell mechanics has endeavored to describe its mechanical properties and how they are actively regulated by the cell (extensively discussed in section *1.2.2.*) (reviewed in (Tatyana M. Svitkina, 2020) and (Kelkar et al., 2020)).

In spite of all these works, several questions are yet to be answered. A surprising lack of knowledge lies in the contextualization of cortex mechanics within the general framework of cell surface mechanics. In other words, a comprehensive biophysical and biochemical model that integrates the different mechanical properties of the cell surface and establishes how they influence each other is currently missing. Indeed, aiming at simplifying the complexity of the system, several biophysical models assume cell cortex mechanics to dominate over the other mechanical properties of the cell surface, which in turn

are considered negligible (*e.g.* the liquid-droplet model (A. Yeung & Evans, 1989)) (reviewed in (Lim et al., 2006)). Alternatively, the cell cortex is modeled as a rigid sheet that cannot be deformed by the PM mechanics nor MCA (J. Dai & Sheetz, 1995) (Robert M. Hochmuth et al., 1996) (Jianwu Dai & Sheetz, 1999) (Brochard-Wyart et al., 2006) (Borghi & Brochard-Wyart, 2007).

The findings described in part C of my thesis challenge those assumptions since they show that variations in MCA do regulate cortex mechanics. Indeed, by indenting cells with AFS, we found that a iMC linker- or CAaezrin-dependent increase in MCA translates into a reduction in cortical stiffness. Importantly, this regulation has been measured in two different cell lines, suggesting the universality of the phenomenon.

Next, we measured the two major contributors of cortical stiffness, namely cortical tension and cell cortex elasticity (Salbreux et al., 2012). Upon the expression of iMC linker, we found that cells reduce their cortical tension while simultaneously increasing the local cortex elasticity. The contradiction between the opposite trends of these two mechanical properties is only apparent, since regulatory mechanisms often simultaneously affect multiple mechanical properties of the cortex in different manners. In particular, an increase in actin crosslinking degree, actin filaments length or cortex thickness does always positively regulate the cortex Young's modulus, whereas the effect on cortical tension depends on the magnitude of such increase (Ennomani et al., 2016) (Chugh et al., 2017) (Xia et al., 2019). Indeed, if these parameters undergo only a moderate increase, cortical tension does raise as well owing to their contribution to the passive component of cortical tension. On the contrary, a large increase in actin crosslinking, filaments length or cortex thickness cause a drop in contractility (the active component of cortical tension). This is attributed to the reduction in the pore size of the actin meshwork which prevents diffusion of myosin-II minifilaments into the cortex (Xia et al., 2019). Furthermore, according to the active gel theory discussed in section *1.2.2.2.*, too long filaments

and/or high level of crosslinking produce a very rigid cortex that cannot be remodeled and hence contracted (Ennomani et al., 2016) (Chugh et al., 2017).

In order to shed light on which of the cortical parameters described above underlies the MCA-dependent regulation of cortex mechanics, we first measured cortical thickness and found no significant difference between iMC linker-expressing and control cells. Moreover, we are currently evaluating iMC linker-dependent modifications of the architecture of the cortex with cryo-electron tomography. Our preliminary analysis of the tomograms revealed that spherical NIH 3t3 cells display highly anisotropic cortexes, regardless of iMC linker expression. Thus, the expression of iMC linker might not be sufficient to further increase the anisotropy level of the of the cortex. Nevertheless, proper segmentation of a larger number of tomograms will have to be carried out in order draw any conclusion on cortex architecture.

Given all our preliminary data, changes in cortical filaments length are a suitable candidate mechanism for explaining MCA-driven regulation of cortex mechanics. This hypothesis is backed up by two recent publications on the role of MCA in mesenchymal cell migration (Welf et al., 2019) (Bisaria et al., 2020). Both studies show that lamellipodia initiation is conditional on the local depletion of MCA linkers in the front of the cell. The reduction in MCA leads to the extension of the distance between the PM and the cortex, allowing actin regulators to bind the PM where they activate the actin remodeling factors that drive lamellipodia formation (Bisaria et al., 2020). In line with these findings, our biophysical measurements, and the prelimiar analysis from our cryo-electron tomograms, we speculate that iMC linker expression leads to a reduction in the distance between the PM and the cortex, preventing the diffusion of actin remodeling factors onto the PM. Filaments length in the cortex is governed by the activity of Arp2/3 complex and the Formin mDia1 (Bovellan et al., 2014). As discussed in section *1.1.2.3.*, the former is active only at the PM where it generates branched actin networks characterized by short filaments. On the contrary, mDia1 polymerizes long filaments by adding actin monomers to the

barbed end and it acts throughout the entire cortex (Fritzsche et al., 2016). Ergo, MCA may govern cortex mechanics by regulating the fraction of Arp2/3 complex-generated short branched actin filaments.

In order to test this hypothesis, we are currently engineering iMC linkers of different length by inserting a different number of dark-mCherry between the Lyn motif and CHCH(Utr). If the expression of longer linkers does not lead to a reduction in cortical stiffness, we will be able to conclude that the distance between the PM and the cortex is a crucial factor for the MCA-dependent regulation of cortex mechanics. Furthermore, deep analysis of the cryo-electron tomograms and measurements of cortical stiffness and tension on iMC linker expressing cells treated with actin nucleators inhibitors will give us a more comprehensive picture. Together this set of experiments will allow us to further understand the nature of the role of MCA in regulating cell cortex mechanics and will help in building a new comprehensive biophysical model to describe animal cell surface mechanics.

4. Experimental procedures

4.1. Cell culture

4.1.1. Adherent immortalized cell lines: A549, NIH 3t3, HeLa Kyoto, HEK 293T, MCF10a

A549 and HeLa Kyoto cells were kindly provided by the EMBL metabolomic facility and Carsten Schultz's laboratory (Oregon Health & State University) respectively. HEK 293T, NIH 3t3 and MCF10a were acquired from ATCC repository.

All the cell lines were cultured at 37 ˚C and at 5 % CO_2 on polystyrene culture dishes (Corning). A549 and NIH 3t3 cells were grown in DMEM low glucose (Sigma-Aldrich) supplemented with 10 % fetal bovine serum (Gibco), 1% Pen-strep (Gibco), 3.7 g/l sodium bicarbonate and 2.5 mM glucose. HeLa kyoto cells were grown in DMEM low glucose (Sigma-Aldrich) supplemented with 10 % fetal bovine serum (Gibco) and 1 % Pen-strep (Gibco). HEK 293T cells were grown in DMEM low glucose (Sigma-Aldrich) supplemented with 10 % fetal bovine serum (Gibco) and 1 % Pen-strep (Gibco), 2.5 mM glucose and 1 mM sodium

pyruvate (Gibco). MCF10a cells were grown in DMEM/F12 (Thermofisher) supplemented with 5 % horse serum (Thermofisher), 20 µg/l EGF (PeProtech), 0.5 mg/l hydrocortisone (Sigma-Aldrich), 10 mg/l insulin (Invitrogen), and 100 µg/l cholera toxin (Sigma-Aldrich).

Cells were passaged every 2-3 days (70-80 % confluency) using 0.05% trypsin-EDTA (Sigma-Aldrich) at ratios of 1/4–1/6. Cells were kept in culture for no longer than 12 passages and were routinely tested for Mycoplasma contamination (Mycoalert^{TM} detection kit, Lonza).

4.1.2. HL60

Undifferentiated HL60 cells were cultured at 37 ˚C and at 5 % CO_2 in 75 cm² U-shaped canted neck cell culture flasks with vent cap (Corning). Cells were grown in RPMI-1640 (Thermofisher) supplemented with 10% heat-inactivated fetal bovine serum (Gibco), 1 % Pen-strep (Gibco), 2 mM L-glutamine and 25 mM HEPES. Cells were passaged every 2 days (1.5-2*10^6 cells/ml) diluting them in fresh growth medium at ratios of 1/4–1/6. Cells were kept in culture for no longer than 12 passages and were routinely tested for Mycoplasma contamination (Mycoalert^{TM} detection kit, Lonza).

Cell terminal differentiation into neutrophil-like cells was initiated by adding 1.5 % DMSO (Sigma-Aldrich) to the cell medium. Cells were used in experiments 4 days after inducing differentiation.

4.1.3. Mouse Embryonic stem cells (mESCs)

Male mESCs expressing Rex1-GFPd2 (Toyooka et al., 2008) were kindly provided by Austin Smith's laboratory (Cambridge Stem Cell Institute). Cells were cultured at 37 ˚C and at 5 % CO_2 on polystyrene culture dishes coated with 0.1 % (w/v) Gelatin (Sigma-Aldrich).

Naïve cells were grown in serum-free N2B27 supplemented with 2i (1 µM PD0325901and 3 µM CHIR99021, both Tocris) and LIF (10 µg/ml, EMBL Protein Expression Facility) solution. Primed cells were cultured similarly in N2B27 medium supplemented with 12 ng/ml FGF2 and 20 ng/ml Activin A (both PeproTech). N2B27 medium was prepared from a 1:1 mixture of DMEM/F12 (without HEPES, with L-glutamine) and neurobasal medium (no L-glutamine), supplemented with 0.5× B-27 (without vitamin A) and 0.5× N-2 supplement, 1 % pen-strep, 2.5 mM L-glutamine (all Thermofisher), 10 µg/ml BSA fraction V and 10 µg/ml human recombinant insulin (both Sigma-Aldrich). Medium was changed every other day and cells were passaged using 0.05 % Trypsin-EDTA (Sigma-Aldrich) at ratios of 1/4–1/10. Cells were kept in culture for no longer than 12 passages and were routinely tested for Mycoplasma contamination (Mycoalert^{TM} detection kit, Lonza).

To induce differentiation and exit from naïve pluripotency, mESCs originating from 2i/LIF culture were plated on Gelatin-coated polystyrene dishes at a density of about 40.000 cells/cm^2 in plain N2B27 medium (or 2i/LIF medium as control) and cultured for 48 h. Expression of constructs was induced by adding 1 µg/ml doxycycline (Sigma-Aldrich) at the time of seeding.

4.2. Cell line generation

4.2.1. Constructs

All the sequences of interest were amplified from donor plasmids through Polymerase Chain Reaction (PCR). Source plasmids were kindly provided by other laboratories or acquired from Addgene and DNASU plasmid repositories, as summarized in table 4.1.

Table 4.1. List of sequences used in this thesis and source of the donor plasmid.

Sequences of interest	Source
Ezrin	Jan Ellenberg's laboratory (EMBL)
Moesin	Jan Ellenberg's laboratory (EMBL)
eGFP	Diz-Muñoz' laboratory (EMBL)
mCherry	Diz-Muñoz' laboratory (EMBL)
Myosin-Ic	DNASU repository
Stargazin	Addgene repository
IL2Rα	Guillaume Charras' laboratory (UCL, London)
PLCΔ1	Addgene repository
PKCα	Diz-Muñoz' laboratory (EMBL)
Tubby	DNASU repository
Akt1	Diz-Muñoz' laboratory (EMBL)
MgcRacGAP	DNASU repository
PI3K-C2γ	DNASU repository
Anillin	Peter Lenart's laboratory (MPI Göttinger)
TCGAP	DNASU repository
Villin	DNASU repository
Filamin A	Diz-Muñoz' laboratory (EMBL)
α Actinin	Rainer Pepperkok's laboratory (EMBL)
Abl1	Diz-Muñoz' laboratory (EMBL)
Utrophin	Diz-Muñoz' laboratory (EMBL)
CAezrin	Generated from Ezrin (T567D)
DNezrin	Generated from Ezrin (T567A)

Amplified sequences of interests were then cloned into a suitable vector through Gibson assembly as described in (Gibson et al., 2009). Three vectors were used in this thesis: pCI-NEO (Promega) for transient transfection (section *4.2.2.*), and pHR and pPB for stable transfection (section *4.2.3.*).

4.2.2. Transient transfection

Cell lines transiently expressing exogenous constructs were generated via lipofection. It was performed as follows: first, sequences of interest were cloned

into pCI-NEO vector (Promega). Then, target cells were grown to 50 % confluency on a polystyrene 6-well plate and transfected using 1 µg of plasmid with lipofectamine 2000 (Invitrogen) according to manufacturer's instructions. Cells were used in experiments the day after lipofection.

4.2.3. Stable transfection

4.2.3.1. Constitutive expression of the constructs

Stable cell lines constitutively expressing exogenous constructs were generated via lentiviral transduction. Lentiviral vector production was performed as follows: first, sequences of interest were cloned into pHR vector (pHR-CMV) to generate the lentivirus plasmids. Then, producer cells (HEK 293T) were grown to 50-70% confluency on a polystyrene 6-well plate and transfected using 1.5 µg lentivirus plasmid, 160 ng VSV-G, and 1.3 µg CMV 8.91 with TransIT-Lenti transfection reagent (Mirus Bio) according to manufacturer's instructions. Supernatants were collected 2 days after transfection, passed through a 0.45 µm filters, and concentrated using Lenti-X concentrator (Clontech) according to manufacturer's instructions. Concentrated virus was used for infection immediately or kept at –20 °C for long-term storage.

For lentiviral transduction, 10 µl (for adherent cell lines) or 100 µl (for HL60) of each concentrated virus was added directly to the target cells in the presence of 4 µg/ml polybrene. Virus-containing medium was replaced with normal growth media after 24 h.

4.2.3.2. Inducible expression of the constructs

To generate stable cell lines with inducible constructs, sequences of interest were cloned into a PiggyBac vector expressing a Neomycin resistance gene (pPB-TRE_CAG-Tet3G-IN). Stable integration was achieved by co-transfecting the PiggyBac plasmid and a plasmid encoding the PiggyBac

transposase using Lipofectamine 3000 (Invitrogen) according to manufacturer's instructions. Selection of cells successfully undergone integration of the construct in the genome were performed adding 400 µg/ml (for mESCs) or 1000 µg/ml (for NIH 3t3) Geneticin (Gibco). Expression of constructs was induced by adding 1 µg/ml doxycycline (Sigma-Aldrich) at the day before using the cells in an experiment.

4.2.4. Transgenic cell line sorting

4.2.4.1. Cell population bulk sorting

All the transgenic cell lines constitutively expressing CAezrin or iMC linker were sorted for high expressers by fluorescence-activated cell sorting (FACS) on a BD FacsAria fusion (BD BioSciences), and bulk-sorted populations consisting of fluorescence positive cells were used for each experiment. CAezrin-HeLa, CAezrin-HEK, CAezrin-HL60, iMC-linker-HL60 expressing cells were then re-transfected with the same construct (*i.e.* super-infection) to further enhance the expression of the transgenic construct.

4.2.4.2. Single clone generation

All the transgenic inducible cell lines used in this thesis were clonal lines. mESC clonal lines were generated by picking single colonies using 10 µl micropipette tips under bright field microscopy by gently scraping off the colonies from the plastic and sucking them into the tip. Each colony was then expanded independently on Gelatin-coated multi-well dishes.

NIH 3t3 clonal lines were generated by de-adhering the cells from the culture dish, diluting them in growth media up to a concentration of ~100 cells/ml and seeding 100 µl of cell suspension on polystyrene 96-well plates. Wells containing only one cell were then kept for the expansion of the clones.

Finally, Single clones were screened for low background expression levels and matching expression levels upon induction using an LSRFortessa flow cytometer (BD BioSciences).

4.3. Artificial MCA linker screening

Production of the screening dishes was performed as follows: low gelling temperature agarose was dissolved in double distilled water to a final concentration of 1.5 % (w/v). The agarose solution was then supplemented with growth medium (1:10 volume), 10x PBS (1:10 volume), and FBS (to a final concentration of 10% (v/v). The final solution was then poured into 3.5-cm glass-bottomed dishes (Ibidi) previously coated with 0.2 mg/ml PLL-g-PEG (Susos) and stored at 4 ˚C for solidification.

Before a screening session, a small hole was made on the agarose by using a 3-mm biopsy punch and the agarose-coated dish was incubated for 1 h at 37 ˚C and 5 % CO_2. Subsequently, A549 cells constitutively expressing CAezrin, GFP, or a candidate artificial MCA linker were detached from the culture plate through trypsinization, concentrated through centrifugation and injected between the layer of agarose and the bottom of the dish.

Cells were imaged on an Eclipse Ti inverted light microscope (Nikon) using a 40x air objective. Time-lapse DIC (2 min, 0.1 fps) and epifluorescence images were acquired to evaluate blebbing behavior and exogenous construct expression level.

4.4. Atomic force spectroscopy

4.4.1. Concanavalin A stress test

Cell lines selected for tether pulling experiments (section *4.4.2.*) were tested for resilience to concanavalin A (con A) cytotoxicity. In brief, cells were

seeded at a low confluency on polystyrene 6-well plate (Corning) and incubated over night at 37 ˚C and 5 % CO_2. Prior to the con A treatment, bright field images of the cells were acquired on an Eclipse Ti inverted light microscope (Nikon). Con A (Sigma-Aldrich) was then added to the medium at a final concentration 0.3 mg/ml and cells were incubated at 37 ˚C and 5 % CO_2 for 2 h. Afterwards, bright field images of the cells were acquired and large changes in cell shape were evaluated. Cell lines displaying dysmorphologies upon con A treatment were not considered for tether pulling experiments (Table 4.2).

Table 4.2. list of cell lines tested for con A resiliency. Y: resilient. N: non-resilient.

Cell line	Con A resiliency
A549	N
mESCs	Y
HEK 293T	Y
HeLa kyoto	Y
MCF10a	Y
HL60	Y
NIH 3t3	Y
A375	N
MDCK	Y

4.4.2. Micropatterning

Micropatterning was performed using an inverted Nikon microscope Ti2 equipped with the Primo micropatterning module (Alvéole lab). In brief, a 35-mm glass-bottomed dish was plasma treated for 1 min and coated with 0.2 mg/ml PLL-g-PEG (Susos) for 1 h and at room temperature. The dish was then rinsed in PBS and the glass bottomed surface was covered with a thin layer PLPP (Alveole lab). The dish was placed on the microscope stage and photo-patterning was controlled with the μmanager software v.1.4.22 by the Leonardo plugin

software v.4.12 (Alvéole lab). A 375 nm (4.5 mW) laser was used, applying a dose of 2000 mJ/mm^2. ~300 20-µm circles distant 40 µm from each other were patterned on the dish. Finally the dish was coated with 50 µg/ml Fibronectin.

4.4.3. Tether Pulling

Apparent PM tension and MCA were measured extruding plasma membrane tethers. In brief, OBL-10 cantilevers (Bruker) were mounted on a CellHesion 200 AFM (Bruker) which is integrated into an Eclipse Ti inverted light microscope (Nikon). Cantilevers were then calibrated using the thermal noise method (spring constant ~ 60 pN/nm) (reviewed in (Gauthier et al., 2011) (Houk et al., 2012)) and coated with 2.5 mg/ml Con A for 1 h at 37˚ C. Before the measurements, cantilevers were rinsed in PBS. For the measurements, cells were seeded on Cellview glass bottom dishes (Greiner) or 35-mm glass-bottomed low µ-Dishes (Ibidi).

Measurements were run as follows: approach velocity was set to 0.5 µm/s while contact force and contact time were varied between 100 to 200 pN and 100 ms to 10 s respectively, aiming to maximize the probability to extrude single tethers. Apparent PM tension was measured using the static tether method: to ensure tether breakage at 0 velocity, the cantilever was retracted for 10 µm at a velocity of 10 µm/s. The position was then kept constant for 20 s and tether force at the moment of tether breakage was recorded at a sampling rate of 2000 Hz. MCA was measured using the dynamic tether method: each cell was probed multiple times at different pulling velocities (2, 5, 10, 30 µm/s) in a random order; only tethers which broke during the pulling phase were considered. Tethers were allowed to retract completely between successive pulls. Resulting force–time curves were analyzed using JPK Data Processing Software. Measurements were run at 37˚ C with 5 % CO_2 and samples were used no longer than 1 h for data acquisition.

4.4.4. Tether data analysis and model assumptions

Static tether puling: apparent PM tension (T) depends on the breakage tether force (f_0) and the bending rigidity (B). We used a previously measured values for B ($2.7*10^{-19}$ Nm for mESCs (Robert M. Hochmuth et al., 1996), and $6.8*10^{-20}$ Nm for NIH 3t3 cells (Raucher et al., 2000)), which we assumed to be unchanged throughout the experiment:

$$f_0 = 2\pi\sqrt{2TB}$$

Dynamic tether pulling: To estimate MCA, PM tethers were pulled at different retraction velocities (v), where the tether force (f) increases with increasing velocity. To interpret such measurements, the Brochard-Wyart et al. model was applied to the data using Monte-Carlo based fitting (Pedroni & Sconfietti, 2020):

$$a \cong (2\pi)^3 2B^2 \upsilon\eta_e \ln\left(\frac{R}{r_t}\right)$$

Since the radius of the cell (R_c) >> radius of the tether (R_t), and bending rigidity B is assumed to be constant, the tether force increase with pulling velocity depends only on effective viscosity (η_e) and the density of the MCA linkers (ν).

4.4.5. Nano-indentation

Cortical stiffness was measured by indenting the apical domain of the cell surface with a spherical indenter and calculating the apparent elastic response of the cortex. In brief, a 10-µm borosicate glass bead (Novascan) was attached to the flat tip of a MLCT-O10 cantilever (Bruker) using epoxy glue (Araldite). The

cantilever was mounted on CellHesion 200 AFM (Bruker) which is integrated into an Eclipse Ti inverted light microscope (Nikon). The cantilever was then calibrated using the thermal noise method (spring constant ~0.01 N/m) (reviewed in (Gauthier et al., 2011) (Houk et al., 2012)) and coated with 1 % Pluronic (Sigma-Aldrich) for 30 min at 37˚ C. Before the measurements, the cantilever was rinsed in PBS. For the measurements, cells were seeded on 35-mm glass-bottomed low µ-Dishes (Ibidi) previously coated with Gelatin (for mESCs) or micropatterned as described in section 4.4.1 (for NIH 3t3). Cells were approached at 4 µm/s and indented at a 0.4 µm/s rate, with a maximum force of 500 pN. Cells were allowed to recover the original shape between successive indentations.

The Hertz model for spherical indenters was used to determine the cortical stiffness of cells (Lin et al., 2009). The upper 300 nm of the cell surface were considered for all fits. Cells were assumed to be incompressible and a Poisson's ratio of 0.5 was used in the calculation of the apparent Young's elastic modulus.

4.5. Re-plating assay

Cells were allowed to exit from naïve pluripotency in plain N2B27 medium. After 48 h, cells were resuspended and counted using trypan blue. A specific number of living cells (typical density: 5000-10.000/cm2) was then re-plated in 2i/LIF medium. After 4-6 days, the number of colonies was manually counted. This assay quantifies the efficiency of pluripotency exit, as only naïve cells survive in 2i/LIF medium (Mulas et al., 2019).

4.6. Flow cytometry

Cells were dissociated to single-cell suspension with 0.05 % Trypsin-EDTA (Thermofisher), resuspended in PBS supplemented with 0.1 % BSA and 2.5 mM

EDTA, strained through a 40 µm cell strainer (BD Biosciences) and analysed on an LSRFortessa flow cytometer (BD BioSciences). Flow cytometry data was gated on forward and side scatters using FlowJo software. Occasionally, DAPI was added as live-dead-stain to the cells and data was gated further on DAPI fluorescence to check for cellular integrity. Fluorescent levels of individual populations were quantified by their geometric means.

4.7. Scanning electron microscopy

For scanning electron microscopy imaging, Rex1-GFPd2 mESCs were cultured for 24 h on glass coverslips previously cleaned, plasma treated for 2 min and coated with 0.1 % Gelatin (Sigma-Aldrich), 10 µg/ml human fibronectin (Corning) or 5 µg/ml Laminin 511 (Biolamina). Cells were fixed for 30 min at room temperature with 4 % (w/v) formaldehyde (EMS) and 2.5 % (w/v) glutaraldehyde (EMS) dissolved in 0.1 M PHEM buffer (60 mM PIPES; 25 mM HEPES; 10 mM EGTA; 2 mM Magnesium chloride; pH 6.9). Afterwards, rinsing in PHEM buffer and water, post-fixation with 1 % (w/v) osmium tetroxide (EMS) in water and 0.8 % potassium hexacyanoferrate (III) (EMS) in water, 1 % (w/v) tannic acid (EMS) in water and 1 % (w/v) uranyl acetate (Serva) in water, and dehydration in ascending series of ethanol and drying in ascending series of HMDS (Sigma-Aldrich) were performed using microwave-assisted processing (Biowave Pro, Pelco). Prior to imaging, a layer of gold was sputter-coated onto the sample (Quorum Q150RS). Cells were acquired with either the Teneo (Thermofisher) or the Crossbeam-540 (Zeiss) at an accelerating voltage of 5 kV detecting secondary electrons. Cell area was quantified manually using Fiji.

4.8. RNA-sequencing

105 to 107 cells were pelleted via centrifugation and total RNA was extracted with the mirVana miRNA Isolation Kit (Thermofisher) according to the

manufacturers recommendations. NGS Libraries were prepared and sequenced by the EMBL Genomics Core Facility. The obtained mRNA sequencing reads were mapped against the mouse genome (GRCm38) using STAR (with default options). Read per gene counts were produced during alignment (--quantMode) based on GRCm38.83 annotation. The obtained raw read counts were processed as follows: Genes with less than 1 count-per-million reads (cpm) in half the samples were removed using the cpm function in the edgeR library. Next, the voom function in the limma package was used to normalise the read counts and a linear model to the normalised data was applied for identification of differentially expressed genes. Genes with false discovery rate (FDR) corrected p-value <0.05 and fold change of >1 were considered as differentially expressed genes. ggplot2 in R was used for data visualisation. Pathway map enrichments were performed using the enrichR package.

4.9. DNA methylation analysis

LUMA was used to measure the global CpG methylation status (Karimi et al., 2006). In brief, genomic DNA from mESCs was isolated using the Quick-DNA Microprep Plus Kit (Zymo Research, #D4074) and quantified using Qubit III. Each sample of genomic DNA (75-150ng) was digested in two parallel reactions at 37˚ C for 4 h with HpaII or MspI and EcoRI as an internal control for both reactions. Overhangs from both reactions were then analyzed using the PyroMark Q24 Advanced system from Qiagen, with the dispensation order GTGTGTCACACA GTGT. Percentage of genome-scale methylated CpGs was determined by comparing the EcoRI normalized HpaII signal intensity ratio to the normalized MspI signal intensity ratio using the following equations:

$$HpaII\ ratio: \frac{Dispensation\ 7 + 13}{\left(\frac{Dispensation\ 8 + 14}{2}\right)}$$

$$MspI\ ratio: \frac{Dispensation\ 7 + 13}{\left(\frac{Dispensation\ 8 + 14}{2}\right)}$$

$$\%\, mCpG : 100\% \times \left(1 - \frac{HpaII\ ratio}{MspI\ ratio}\right)$$

4.10. Micropipette aspiration

A microforged micropipette coupled to a microfluidic pump (Fluigent) and mounted on an inverted Axio A1 microscope (Zeiss) was used to measure cortical tension of cells. In brief, micropipettes of radii 7–8 µm were used to apply step-wise increasing pressures on NIH 3t3 cells in suspension until (seeded on PLL-g-PEG-coated 60-mm glass-bottomed Ibidi dishes) reaching a deformation which has the radius of the micropipette (R_p) . At steady state, the cortical tension (T) of the cell is calculated based Law of Laplace: $T = P_c/2(1/R_p - 1/R_c)$, where Pc is the pressure used to deform the cell of radius R_c.

4.11. Magnetic pincher

4.11.1. Experimental chamber and cell preparation

Magnetic pinching experiments were performed in custum-made 8x8x5 mm glass and PDMS chambers. In brief, the PDMS was prepared from Sylgard raw products (Sigma-Aldrich) with a ratio base-curing agent of 9:1 using a standard protocol (curing step: 1h at 90°C). The block forming the walls of the chamber was then cut and bond to a 64x20x0.17 mm glass coverslip using a plasma cleaner. Prior to the beginning of the experiment, the chambers was coated with a 5% BSA for 30 min in order to reduce the adhesiveness of the substrate and force the cell to acquire a quasi-spherical shape.

iMC linker-NIH 3t3 cells, either induced or uninduced, were seeded on the experimental chamber the day before the experiment. Immediately after cell seeding, the medium was supplemented with Dynabeads M-450 Epoxy

(Invitrogen). Cells were then incubated over night at 37 ˚C and 5 % CO_2 to allow adhesion and bead phagocytosis.

4.11.2. Magnetic pincher setup

The whole setup is mounted on an inverted Axio A1 microscope (Zeiss). The customized microscope stage supports two coils, responsible for the generation of a magnetic field, and the experimental chamber. The coils are positioned in a pseudo-Helmoltz configuration so that the generated magnetic field at the position of the sample is homegeneous. They are alimented by a Bipolar Operational Power (BOP) supply of 6A, which delivered a current of controlled intensity. Bright field films were recorded with an Orca Flash 4 camera (Hamamatsu). The precise motion of the objective (100x, oil immersion) along the Z-axis is realized with a P-725.SDD PIFOC piezo scanner and its E-709 controller (PI instruments). All the elements of the pincher were controlled by Labview. The whole setup was placed inside an incubation box and the experiment was performed at 37 °C and 5 % CO_2.

Median cortical thickness was measured via a constant field assay, in which the intensity of the magnetic field is kept constant to 10mT and oscillations in cortical thickness are recorded for 5 min. Cortex elastic modulus was measured via a compression assay. In brief, cells were subjected to a fluctuating magnetic field, with ramps ranging from 3 mT to 40 mT and a constant field of 10 mT between ramps.

4.12. Quantification and statistical analysis

Data were analyzed, tested for statistical significance, fitted and visualized using R. No statistical method was used to predetermine sample size. No estimation of variance was performed. The Shapiro–Wilk test was used to test for normality of data. Welch’s t-test was chosen for statistical testing of normal

distributed data with low sample size (n<30). For non-normal distributed data with low sample size (n<30), Mann-Whitney U-test was performed. For large sample sizes (n>30), the Z Test was used.

5. References

Aguilar, A., Pertuy, F., Eckly, A., Strassel, C., Collin, D., Gachet, C., Lanza, F., & Léon, C. (2016). Importance of environmental stiffness for megakaryocyte differentiation and proplatelet formation. *Blood*, *128*(16), 2022–2032. https://doi.org/10.1182/blood-2016-02-699959

Akkas, N. (1981). A viscoelastic model for cytokinesis in animal cells. *Journal of Biomechanics*, *14*(9), 621–631. https://doi.org/10.1016/0021-9290(81)90088-9

Alberts, B., Johnson, A., Lewis, J., Morgan, D., Raff, M., Roberts, K., & Walter, P. (2015). Molecular Biology of the Cell. In J. Wilson & T. Hunt (Eds.), *Molecular Biology of the Cell* (4th ed., pp. 565–596). Garland Science. https://doi.org/10.1201/9781315735368

Alert, R., Casademunt, J., Brugués, J., & Sens, P. (2015). Model for Probing Membrane-Cortex Adhesion by Micropipette Aspiration and Fluctuation Spectroscopy. *Biophysical Journal*, *108*(8), 1878–1886. https://doi.org/10.1016/j.bpj.2015.02.027

Álvarez-González, B., Meili, R., Bastounis, E., Firtel, R. A., Lasheras, J. C., & del Álamo, J. C. (2015). Three-Dimensional Balance of Cortical Tension and Axial Contractility Enables Fast Amoeboid Migration. *Biophysical Journal*, *108*(4), 821–832. https://doi.org/10.1016/j.bpj.2014.11.3478

Ananthakrishnan, R., Guck, J., Wottawah, F., Schinkinger, S., Lincoln, B., Romeyke, M., Moon, T., & Käs, J. (2006). Quantifying the contribution of actin networks to the elastic

strength of fibroblasts. *Journal of Theoretical Biology*, *242*(2), 502–516. https://doi.org/10.1016/j.jtbi.2006.03.021

Armstrong, R., & Hanczyc, M. (2013). Bütschli Dynamic Droplet System. *Artificial Life*, *19*(3_4), 331–346. https://doi.org/10.1162/ARTL_a_00111

Baluška, F., Volkmann, D., & Barlow, P. W. (2004). Eukaryotic cells and their Cell Bodies: Cell theory revised. *Annals of Botany*, *94*(1), 9–32. https://doi.org/10.1093/aob/mch109

Barreiro, O., Yáñez-Mó, M., Serrador, J. M., Montoya, M. C., Vicente-Manzanares, M., Tejedor, R., Furthmayr, H., & Sánchez-Madrid, F. (2002). Dynamic interaction of VCAM-1 and ICAM-1 with moesin and ezrin in a novel endothelial docking structure for adherent leukocytes. *Journal of Cell Biology*, *157*(7), 1233–1245. https://doi.org/10.1083/jcb.200112126

Batchelder, E. L., Hollopeter, G., Campillo, C., Mezanges, X., Jorgensen, E. M., Nassoy, P., Sens, P., & Plastino, J. (2011). Membrane tension regulates motility by controlling lamellipodium organization. *Proceedings of the National Academy of Sciences*, *108*(28), 11429–11434. https://doi.org/10.1073/pnas.1010481108

Bausch, A. R., & Kroy, K. (2006). A bottom-up approach to cell mechanics. *Nature Physics*, *2*(4), 231–238. https://doi.org/10.1038/nphys260

Bennett, V., & Chen, L. (2001). Ankyrins and cellular targeting of diverse membrane proteins to physiological sites. *Current Opinion in Cell Biology*, *13*(1), 61–67. https://doi.org/10.1016/S0955-0674(00)00175-7

Bereiter-Hahn, J., Luck, M., Miebach, T., Stelzer, H. K., & Voth, M. (1990). Spreading of trypsinized cells: Cytoskeletal dynamics and energy requirements. *Journal of Cell Science*, *96*(1), 171–188.

Bergert, M., Chandradoss, S. D., Desai, R. A., & Paluch, E. (2012). Cell mechanics control rapid transitions between blebs and lamellipodia during migration. *Proceedings of the National Academy of Sciences*, *109*(36), 14434–14439. https://doi.org/10.1073/pnas.1207968109

Bergert, M., Erzberger, A., Desai, R. A., Aspalter, I. M., Oates, A. C., Charras, G., Salbreux, G., & Paluch, E. K. (2015). Force transmission during adhesion-independent migration. *Nature Cell Biology*, *17*(4), 524–529. https://doi.org/10.1038/ncb3134

Bergert, M., Lembo, S., Sharma, S., Russo, L., Milovanović, D., Gretarsson, K. H., Börmel, M., Neveu, P. A., Hackett, J. A., Petsalaki, E., & Diz-Muñoz, A. (2020). Cell Surface Mechanics Gate Embryonic Stem Cell Differentiation. *Cell Stem Cell*, 1–8. https://doi.org/10.1016/j.stem.2020.10.017

Betschinger, J., Nichols, J., Dietmann, S., Corrin, P. D., Paddison, P. J., & Smith, A. (2013). Exit from Pluripotency Is Gated by Intracellular Redistribution of the bHLH Transcription Factor Tfe3. *Cell*, *153*(2), 335–347. https://doi.org/10.1016/j.cell.2013.03.012

Biro, M., Romeo, Y., Kroschwald, S., Bovellan, M., Boden, A., Tcherkezian, J., Roux, P. P., Charras, G., & Paluch, E. K. (2013). Cell cortex composition and homeostasis resolved by integrating proteomics and quantitative imaging. *Cytoskeleton*, *70*(11), 741–754. https://doi.org/10.1002/cm.21142

Bisaria, A., Hayer, A., Garbett, D., Cohen, D., & Meyer, T. (2020). Membrane-proximal F-actin restricts local membrane protrusions and directs cell migration. *Science*, *368*(6496), 1205–1210. https://doi.org/10.1126/science.aay7794

Blanchoin, L., Boujemaa-Paterski, R., Sykes, C., & Plastino, J. (2014). Actin Dynamics, Architecture, and Mechanics in Cell Motility. *Physiological Reviews*, *94*(1), 235–263. https://doi.org/10.1152/physrev.00018.2013

Blin, G., Margeat, E., Carvalho, K., Royer, C. A., Roy, C., & Picart, C. (2008). Quantitative Analysis of the Binding of Ezrin to Large Unilamellar Vesicles Containing Phosphatidylinositol 4,5 Bisphosphate. *Biophysical Journal*, *94*(3), 1021–1033. https://doi.org/10.1529/biophysj.107.110213

Borghi, N., & Brochard-Wyart, F. (2007). Tether Extrusion from Red Blood Cells: Integral Proteins Unbinding from Cytoskeleton. *Biophysical Journal*, *93*(4), 1369–1379. https://doi.org/10.1529/biophysj.106.087908

Borrego-Diaz, E., Kerff, F., Lee, S. H., Ferron, F., Li, Y., & Dominguez, R. (2006). Crystal structure of the actin-binding domain of α-actinin 1: Evaluating two competing actin-binding models. *Journal of Structural Biology*, *155*(2), 230–238. https://doi.org/10.1016/j.jsb.2006.01.013

Bovellan, M., Romeo, Y., Biro, M., Boden, A., Chugh, P., Yonis, A., Vaghela, M., Fritzsche,

M., Moulding, D., Thorogate, R., Jégou, A., Thrasher, A. J., Romet-Lemonne, G., Roux, P. P., Paluch, E. K., & Charras, G. (2014). Cellular Control of Cortical Actin Nucleation. *Current Biology*, *24*(14), 1628–1635. https://doi.org/10.1016/j.cub.2014.05.069

Braet, F., Soon, L., Vekemans, K., Thordarson, P., & Spector, I. (2008). Actin-Binding Drugs: An Elegant Tool to Dissect Subcellular Processes in Endothelial and Cancer Cells. In C. G. dos Remedios & D. Chhabra (Eds.), *Actin-Binding Proteins and Disease* (pp. 37–49). Springer New York. https://doi.org/10.1007/978-0-387-71749-4_3

Bray, D., & White, J. (1988). Cortical flow in animal cells. *Science*, *239*(4842), 883–888. https://doi.org/10.1126/science.3277283

Breitsprecher, D., & Goode, B. L. (2013). Formins at a glance. *Journal of Cell Science*, *126*(1), 1–7. https://doi.org/10.1242/jcs.107250

Bretscher, A., Edwards, K., & Fehon, R. G. (2002). ERM proteins and merlin: integrators at the cell cortex. *Nature Reviews Molecular Cell Biology*, *3*(8), 586–599. https://doi.org/10.1038/nrm882

Brochard-Wyart, F., Borghi, N., Cuvelier, D., & Nassoy, P. (2006). Hydrodynamic narrowing of tubes extruded from cells. *Proceedings of the National Academy of Sciences*, *103*(20), 7660–7663. https://doi.org/10.1073/pnas.0602012103

Brochard, F., De Gennes, P. G., & Pfeuty, P. (1976). Surface tension and deformations of membrane structures : relation to two-dimensional phase transitions. *Journal de Physique*, *37*(10), 1099–1104. https://doi.org/10.1051/jphys:0197600370100109900

Butschli, O. (1892). *Untersuchungen über mikroskopische Schäume und das Protoplasma; Versuche und Beobachtungen zur Lösung der Frage nach den physikalischen Bedingungen der Lebenserscheinungen.* Engelmann.

Carlsson, A. E. (2010). Actin Dynamics: From Nanoscale to Microscale. *Annual Review of Biophysics*, *39*(1), 91–110. https://doi.org/10.1146/annurev.biophys.093008.131207

Carpten, J. D., Faber, A. L., Horn, C., Donoho, G. P., Briggs, S. L., Robbins, C. M., Hostetter, G., Boguslawski, S., Moses, T. Y., Savage, S., Uhlik, M., Lin, A., Du, J., Qian, Y.-W., Zeckner, D. J., Tucker-Kellogg, G., Touchman, J., Patel, K., Mousses, S., … Thomas, J. E. (2007). A transforming mutation in the pleckstrin homology domain of AKT1 in cancer. *Nature*, *448*(7152), 439–444. https://doi.org/10.1038/nature05933

Carreno, S., Kouranti, I., Glusman, E. S., Fuller, M. T., Echard, A., & Payre, F. (2008). Moesin and its activating kinase Slik are required for cortical stability and microtubule organization in mitotic cells. *Journal of Cell Biology*, *180*(4), 739–746. https://doi.org/10.1083/jcb.200709161

Carroll, K., Gomez, C., & Shapiro, L. (2004). Tubby proteins: the plot thickens. *Nature Reviews Molecular Cell Biology*, *5*(1), 55–64. https://doi.org/10.1038/nrm1278

Carvalho, K., Lemière, J., Faqir, F., Manzi, J., Blanchoin, L., Plastino, J., Betz, T., & Sykes, C. (2013). Actin polymerization or myosin contraction: two ways to build up cortical tension for symmetry breaking. *Philosophical Transactions of the Royal Society B: Biological Sciences*, *368*(1629), 20130005. https://doi.org/10.1098/rstb.2013.0005

Chaigne, A., Campillo, C., Gov, N. S., Voituriez, R., Azoury, J., Umaña-Diaz, C., Almonacid, M., Queguiner, I., Nassoy, P., Sykes, C., Verlhac, M.-H., & Terret, M.-E. (2013). A soft cortex is essential for asymmetric spindle positioning in mouse oocytes. *Nature Cell Biology*, *15*(8), 958–966. https://doi.org/10.1038/ncb2799

Chalut, K. J., & Paluch, E. K. (2016). The Actin Cortex: A Bridge between Cell Shape and Function. *Developmental Cell*, *38*(6), 571–573. https://doi.org/10.1016/j.devcel.2016.09.011

Chan, C. J., Costanzo, M., Ruiz-Herrero, T., Mönke, G., Petrie, R. J., Bergert, M., Diz-Muñoz, A., Mahadevan, L., & Hiiragi, T. (2019). Hydraulic control of mammalian embryo size and cell fate. *Nature*, *571*(7763), 112–116. https://doi.org/10.1038/s41586-019-1309-x

Charras, G., & Paluch, E. (2008). Blebs lead the way: how to migrate without lamellipodia. *Nature Reviews Molecular Cell Biology*, *9*(9), 730–736. https://doi.org/10.1038/nrm2453

Charras, G.T. (2008). A short history of blebbing. *Journal of Microscopy*, *231*(3), 466–478. https://doi.org/10.1111/j.1365-2818.2008.02059.x

Charras, Guillaume T., Hu, C.-K., Coughlin, M., & Mitchison, T. J. (2006). Reassembly of contractile actin cortex in cell blebs. *Journal of Cell Biology*, *175*(3), 477–490. https://doi.org/10.1083/jcb.200602085

Chazaud, C., & Yamanaka, Y. (2016). Lineage specification in the mouse preimplantation

embryo. In *Development (Cambridge)* (Vol. 143, Issue 7, pp. 1063–1074). https://doi.org/10.1242/dev.128314

Chiang, S.-H. (2003). TCGAP, a multidomain Rho GTPase-activating protein involved in insulin-stimulated glucose transport. *The EMBO Journal*, *22*(11), 2679–2691. https://doi.org/10.1093/emboj/cdg262

Chikina, A. S., Svitkina, T. M., & Alexandrova, A. Y. (2019). Time-resolved ultrastructure of the cortical actin cytoskeleton in dynamic membrane blebs. *Journal of Cell Biology*, *218*(2), 445–454. https://doi.org/10.1083/jcb.201806075

Chishti, A. H., Kim, A. C., Marfatia, S. M., Lutchman, M., Hanspal, M., Jindal, H., Liu, S.-C., Low, P. S., Rouleau, G. A., Mohandas, N., Chasis, J. A., Conboy, J. G., Gascard, P., Takakuwa, Y., Huang, S.-C., Benz Jr, E. J., Bretscher, A., Fehon, R. G., Gusella, J. F., … Hoover, K. B. (1998). The FERM domain: a unique module involved in the linkage of cytoplasmic proteins to the membrane. *Trends in Biochemical Sciences*, *23*(8), 281–282. https://doi.org/10.1016/S0968-0004(98)01237-7

Chizmadzhev, Y. A., Kumenko, D. A., Kuzmin, P. I., Chernomordik, L. V., Zimmerberg, J., & Cohen, F. S. (1999). Lipid Flow through Fusion Pores Connecting Membranes of Different Tensions. *Biophysical Journal*, *76*(6), 2951–2965. https://doi.org/10.1016/S0006-3495(99)77450-3

Chowdhury, F., Li, Y., Poh, Y.-C., Yokohama-Tamaki, T., Wang, N., & Tanaka, T. S. (2010). Soft Substrates Promote Homogeneous Self-Renewal of Embryonic Stem Cells via Downregulating Cell-Matrix Tractions. *PLoS ONE*, *5*(12), e15655. https://doi.org/10.1371/journal.pone.0015655

Chowdhury, F., Na, S., Li, D., Poh, Y.-C., Tanaka, T. S., Wang, F., & Wang, N. (2010). Material properties of the cell dictate stress-induced spreading and differentiation in embryonic stem cells. *Nature Materials*, *9*(1), 82–88. https://doi.org/10.1038/nmat2563

Chugh, P., Clark, A. G., Smith, M. B., Cassani, D. A. D., Dierkes, K., Ragab, A., Roux, P. P., Charras, G., Salbreux, G., & Paluch, E. K. (2017). Actin cortex architecture regulates cell surface tension. *Nature Cell Biology*, *19*(6), 689–697. https://doi.org/10.1038/ncb3525

Chugh, P., & Paluch, E. K. (2018). The actin cortex at a glance. *Journal of Cell Science*,

131(14), jcs186254. https://doi.org/10.1242/jcs.186254

Cirera-Salinas, D., & Ciaudo, C. (2017). Exit from Pluripotency Assay of Mouse Embryonic Stem Cells. *BIO-PROTOCOL*, *7*(16), 1–8. https://doi.org/10.21769/BioProtoc.2507

Clark, A. G., Dierkes, K., & Paluch, E. K. (2013). Monitoring Actin Cortex Thickness in Live Cells. *Biophysical Journal*, *105*(3), 570–580. https://doi.org/10.1016/j.bpj.2013.05.057

Clark, A. G., Wartlick, O., Salbreux, G., & Paluch, E. K. (2014). Stresses at the Cell Surface during Animal Cell Morphogenesis. *Current Biology*, *24*(10), R484–R494. https://doi.org/10.1016/j.cub.2014.03.059

Clausen, M. P., Colin-York, H., Schneider, F., Eggeling, C., & Fritzsche, M. (2017). Dissecting the actin cortex density and membrane-cortex distance in living cells by super-resolution microscopy. *Journal of Physics D: Applied Physics*, *50*(6), 064002. https://doi.org/10.1088/1361-6463/aa52a1

Cohen, D. M., & Chen, C. S. (2008). Mechanical control of stem cell differentiation. In *StemBook* (pp. 1–16). Stembook. https://doi.org/10.3824/stembook.1.26.1

Coluccio, L. M. (2008). Myosin I. In L. M. Coluccio (Ed.), *Myosins* (pp. 95–124). Springer Netherlands. https://doi.org/10.1007/978-1-4020-6519-4_4

Craiem, D., & Magin, R. L. (2010). Fractional order models of viscoelasticity as an alternative in the analysis of red blood cell (RBC) membrane mechanics. *Physical Biology*, *7*(1), 013001. https://doi.org/10.1088/1478-3975/7/1/013001

Cueto, E., & González, D. (2018). An Introduction to Continuum Mechanics. In *Structural Integrity* (1st ed., pp. 1–31). Springer. https://doi.org/10.1007/978-3-319-72935-0_1

Dai, J., & Sheetz, M. P. (1995). Mechanical properties of neuronal growth cone membranes studied by tether formation with laser optical tweezers. *Biophysical Journal*, *68*(3), 988–996. https://doi.org/10.1016/S0006-3495(95)80274-2

Dai, Jianwu, Ping Ting-Beall, H., Hochmuth, R. M., Sheetz, M. P., & Titus, M. A. (1999). Myosin I Contributes to the Generation of Resting Cortical Tension. *Biophysical Journal*, *77*(2), 1168–1176. https://doi.org/10.1016/S0006-3495(99)76968-7

Dai, Jianwu, & Sheetz, M. P. (1997). Chapter 9 Cell Membrane Mechanics. In M. P. B. T.-M. in C. B. Sheetz (Ed.), *Methods in Cell Biology* (Vol. 55, pp. 157–171). Academic Press. https://doi.org/10.1016/S0091-679X(08)60407-0

Dai, Jianwu, & Sheetz, M. P. (1999). Membrane Tether Formation from Blebbing Cells. *Biophysical Journal*, *77*(6), 3363–3370. https://doi.org/10.1016/S0006-3495(99)77168-7

Dard, N., Louvet-Vallée, S., Santa-Maria, A., & Maro, B. (2004). Phosphorylation of ezrin on threonine T567 plays a crucial role during compaction in the mouse early embryo. *Developmental Biology*, *271*(1), 87–97. https://doi.org/10.1016/j.ydbio.2004.03.024

Dard, N., Louvet, S., Santa-Maria, A., Aghion, J., Martin, M., Mangeat, P., & Maro, B. (2001). In Vivo Functional Analysis of Ezrin during Mouse Blastocyst Formation. *Developmental Biology*, *233*(1), 161–173. https://doi.org/10.1006/dbio.2001.0192

de Brabander, M., Nuydens, R., Ishihara, A., Holifield, B., Jacobson, K., & Geerts, H. (1991). Lateral diffusion and retrograde movements of individual cell surface components on single motile cells observed with Nanovid microscopy. *Journal of Cell Biology*, *112*(1), 111–124. https://doi.org/10.1083/jcb.112.1.111

Delon, J., Kaibuchi, K., & Germain, R. N. (2001). Exclusion of CD43 from the Immunological Synapse Is Mediated by Phosphorylation-Regulated Relocation of the Cytoskeletal Adaptor Moesin. *Immunity*, *15*(5), 691–701. https://doi.org/10.1016/S1074-7613(01)00231-X

Dimitriadis, E. K., Horkay, F., Maresca, J., Kachar, B., & Chadwick, R. S. (2002). Determination of Elastic Moduli of Thin Layers of Soft Material Using the Atomic Force Microscope. *Biophysical Journal*, *82*(5), 2798–2810. https://doi.org/10.1016/S0006-3495(02)75620-8

Dimova, R. (2014). Recent developments in the field of bending rigidity measurements on membranes. *Advances in Colloid and Interface Science*, *208*, 225–234. https://doi.org/10.1016/j.cis.2014.03.003

Dix, C. L., Matthews, H. K., Uroz, M., McLaren, S., Wolf, L., Heatley, N., Win, Z., Almada, P., Henriques, R., Boutros, M., Trepat, X., & Baum, B. (2018). The Role of Mitotic Cell-Substrate Adhesion Re-modeling in Animal Cell Division. *Developmental Cell*, *45*(1), 132-145.e3. https://doi.org/10.1016/j.devcel.2018.03.009

Diz-Muñoz, A., Krieg, M., Bergert, M., Ibarlucea-Benitez, I., Muller, D. J., Paluch, E., & Heisenberg, C.-P. (2010). Control of Directed Cell Migration In Vivo by Membrane-to-

Cortex Attachment. *PLoS Biology*, *8*(11), e1000544. https://doi.org/10.1371/journal.pbio.1000544

Diz-Muñoz, A., Romanczuk, P., Yu, W., Bergert, M., Ivanovitch, K., Salbreux, G., Heisenberg, C.-P., & Paluch, E. K. (2016). Steering cell migration by alternating blebs and actin-rich protrusions. *BMC Biology*, *14*(1), 74. https://doi.org/10.1186/s12915-016-0294-x

Diz-Muñoz, A., Weiner, O. D., & Fletcher, D. A. (2018). In pursuit of the mechanics that shape cell surfaces. *Nature Physics*, *14*(7), 648–652. https://doi.org/10.1038/s41567-018-0187-8

Domin, J., Gaidarov, I., Smith, M. E. K., Keen, J. H., & Waterfield, M. D. (2000). The Class II Phosphoinositide 3-Kinase PI3K-C2α Is Concentrated in the Trans-Golgi Network and Present in Clathrin-coated Vesicles. *Journal of Biological Chemistry*, *275*(16), 11943–11950. https://doi.org/10.1074/jbc.275.16.11943

Dumont, S., & Mitchison, T. J. (2009). Compression Regulates Mitotic Spindle Length by a Mechanochemical Switch at the Poles. *Current Biology*, *19*(13), 1086–1095. https://doi.org/10.1016/j.cub.2009.05.056

Dupuy, A. D., & Engelman, D. M. (2008). Protein area occupancy at the center of the red blood cell membrane. *Proceedings of the National Academy of Sciences*, *105*(8), 2848 LP – 2852. https://doi.org/10.1073/pnas.0712379105

Edwards, M., Zwolak, A., Schafer, D. A., Sept, D., Dominguez, R., & Cooper, J. A. (2014). Capping protein regulators fine-tune actin assembly dynamics. *Nature Reviews Molecular Cell Biology*, *15*(10), 677–689. https://doi.org/10.1038/nrm3869

Eggert, U. S., Mitchison, T. J., & Field, C. M. (2006). Animal Cytokinesis: From Parts List to Mechanisms. *Annual Review of Biochemistry*, *75*(1), 543–566. https://doi.org/10.1146/annurev.biochem.74.082803.133425

Eghiaian, F., Rigato, A., & Scheuring, S. (2015). Structural, Mechanical, and Dynamical Variability of the Actin Cortex in Living Cells. *Biophysical Journal*, *108*(6), 1330–1340. https://doi.org/10.1016/j.bpj.2015.01.016

Ehrenstein, D., & Iwasa, K. H. (1996). Viscoelastic relaxation in the membrane of the auditory outer hair cell. *Biophysical Journal*, *71*(2), 1087–1094. https://doi.org/10.1016/S0006-3495(96)79310-4

Engelhardt, H., & Sackmann, E. (1988). On the measurement of shear elastic moduli and viscosities of erythrocyte plasma membranes by transient deformation in high frequency electric fields. *Biophysical Journal*, *54*(3), 495–508. https://doi.org/10.1016/S0006-3495(88)82982-5

Engler, A. J., Sen, S., Sweeney, H. L., & Discher, D. E. (2006). Matrix Elasticity Directs Stem Cell Lineage Specification. *Cell*, *126*(4), 677–689. https://doi.org/10.1016/j.cell.2006.06.044

Ennomani, H., Letort, G., Guérin, C., Martiel, J.-L., Cao, W., Nédélec, F., De La Cruz, E. M., Théry, M., & Blanchoin, L. (2016). Architecture and Connectivity Govern Actin Network Contractility. *Current Biology*, *26*(5), 616–626. https://doi.org/10.1016/j.cub.2015.12.069

Erickson, C. A., & Trinkaus, J. P. (1976). Microvilli and blebs as sources of reserve surface membrane during cell spreading. *Experimental Cell Research*, *99*(2), 375–384. https://doi.org/10.1016/0014-4827(76)90595-4

Essen, L.-O., Perisic, O., Lynch, D. E., Katan, M., & Williams, R. L. (1997). A Ternary Metal Binding Site in the C2 Domain of Phosphoinositide-Specific Phospholipase C-δ1 † , ‡. *Biochemistry*, *36*(10), 2753–2762. https://doi.org/10.1021/bi962466t

Evans, E., & Rawicz, W. (1990). Entropy-driven tension and bending elasticity in condensed-fluid membranes. *Physical Review Letters*, *64*(17), 2094–2097. https://doi.org/10.1103/PhysRevLett.64.2094

Evans, E.A., & Hochmuth, R. M. (1976). Membrane viscoelasticity. *Biophysical Journal*, *16*(1), 1–11. https://doi.org/10.1016/S0006-3495(76)85658-5

Evans, E.A., & Hochmuth, R. M. (1978). Mechanochemical Properties of Membranes. In *Current Topics in Membranes and Transport* (pp. 1–64). https://doi.org/10.1016/S0070-2161(08)60833-3

Evans, Evan A., & Hochmuth, R. M. (1976). A solid-liquid composite model of the red cell membrane. *The Journal of Membrane Biology*, *30*(1), 351–362. https://doi.org/10.1007/BF01869676

Farge, E. (2003). Mechanical Induction of Twist in the Drosophila Foregut/Stomodeal Primordium. *Current Biology*, *13*(16), 1365–1377. https://doi.org/10.1016/S0960-

9822(03)00576-1

Fehon, R. G., McClatchey, A. I., & Bretscher, A. (2010). Organizing the cell cortex: The role of ERM proteins. *Nature Reviews Molecular Cell Biology*, *11*(4), 276–287. https://doi.org/10.1038/nrm2866

Fenno, L., Yizhar, O., & Deisseroth, K. (2011). The Development and Application of Optogenetics. *Annual Review of Neuroscience*, *34*(1), 389–412. https://doi.org/10.1146/annurev-neuro-061010-113817

Field, C. M., & Alberts, B. M. (1995). Anillin, a contractile ring protein that cycles from the nucleus to the cell cortex. *Journal of Cell Biology*, *131*(1), 165–178. https://doi.org/10.1083/jcb.131.1.165

Fievet, B. T., Gautreau, A., Roy, C., Del Maestro, L., Mangeat, P., Louvard, D., & Arpin, M. (2004). Phosphoinositide binding and phosphorylation act sequentially in the activation mechanism of ezrin. *Journal of Cell Biology*, *164*(5), 653–659. https://doi.org/10.1083/jcb.200307032

Fischer-Friedrich, E., Toyoda, Y., Cattin, C. J., Müller, D. J., Hyman, A. A., & Jülicher, F. (2016). Rheology of the Active Cell Cortex in Mitosis. *Biophysical Journal*, *111*(3), 589–600. https://doi.org/10.1016/j.bpj.2016.06.008

Fischer, H., Polikarpov, I., & Craievich, A. F. (2009). Average protein density is a molecular-weight-dependent function. *Protein Science*, *13*(10), 2825–2828. https://doi.org/10.1110/ps.04688204

Fouassier, L., Yun, C. C., Fitz, J. G., & Doctor, R. B. (2000). Evidence for Ezrin-Radixin-Moesin-binding Phosphoprotein 50 (EBP50) Self-association through PDZ-PDZ Interactions. *Journal of Biological Chemistry*, *275*(32), 25039–25045. https://doi.org/10.1074/jbc.C000092200

Fritzsche, M., Erlenkämper, C., Moeendarbary, E., Charras, G., & Kruse, K. (2016). Actin kinetics shapes cortical network structure and mechanics. *Science Advances*, *2*(4), e1501337. https://doi.org/10.1126/sciadv.1501337

Fritzsche, M., Lewalle, A., Duke, T., Kruse, K., & Charras, G. (2013). Analysis of turnover dynamics of the submembranous actin cortex. *Molecular Biology of the Cell*, *24*(6), 757–767. https://doi.org/10.1091/mbc.e12-06-0485

Fujiwara, T. K., Iwasawa, K., Kalay, Z., Tsunoyama, T. A., Watanabe, Y., Umemura, Y. M., Murakoshi, H., Suzuki, K. G. N., Nemoto, Y. L., Morone, N., & Kusumi, A. (2016). Confined diffusion of transmembrane proteins and lipids induced by the same actin meshwork lining the plasma membrane. *Molecular Biology of the Cell*, *27*(7), 1101–1119. https://doi.org/10.1091/mbc.E15-04-0186

Fukata, Y., Oshiro, N., & Kaibuchi, K. (1999). Activation of moesin and adducin by Rho-kinase downstream of Rho. *Biophysical Chemistry*, *82*(2–3), 139–147. https://doi.org/10.1016/S0301-4622(99)00113-1

Gallagher, R., Collins, S., Trujillo, J., McCredie, K., Ahearn, M., Tsai, S., Metzgar, R., Aulakh, G., Ting, R., Ruscetti, F., & Gallo, R. (1979). Characterization of the continuous, differentiating myeloid cell line (HL-60) from a patient with acute promyelocytic leukemia. *Blood*, *54*(3), 713–733. https://doi.org/10.1182/blood.V54.3.713.713

Gao, J., Liao, J., & Yang, G.-Y. (2009). CAAX-box protein, prenylation process and carcinogenesis. *American Journal of Translational Research*, *1*(3), 312–325. http://www.ncbi.nlm.nih.gov/pubmed/19956441

Gardel, M., & Oakes, P. (2015). Measuring Cell Mechanics. *Colloquium Series on Quantitative Cell Biology*, *2*(1), 1–75. https://doi.org/10.4199/C00137ED1V01Y201508QCB003

Gary, R., & Bretscher, A. (1995). Ezrin self-association involves binding of an N-terminal domain to a normally masked C-terminal domain that includes the F-actin binding site. *Molecular Biology of the Cell*, *6*(8), 1061–1075. https://doi.org/10.1091/mbc.6.8.1061

Gauthier, N. C., Fardin, M. A., Roca-Cusachs, P., & Sheetz, M. P. (2011). Temporary increase in plasma membrane tension coordinates the activation of exocytosis and contraction during cell spreading. *Proceedings of the National Academy of Sciences*, *108*(35), 14467–14472. https://doi.org/10.1073/pnas.1105845108

Gautreau, A., Louvard, D., & Arpin, M. (2000). Morphogenic effects of ezrin require a phosphorylation-induced transition from oligomers to monomers at the plasma membrane. *Journal of Cell Biology*, *150*(1), 193–203. https://doi.org/10.1083/jcb.150.1.193

Gibson, D. G., Young, L., Chuang, R.-Y., Venter, J. C., Hutchison, C. A., & Smith, H. O. (2009).

Enzymatic assembly of DNA molecules up to several hundred kilobases. *Nature Methods*, *6*(5), 343–345. https://doi.org/10.1038/nmeth.1318

Gilden, J., & Krummel, M. F. (2010). Control of cortical rigidity by the cytoskeleton: Emerging roles for septins. *Cytoskeleton*, *67*(8), 477–486. https://doi.org/10.1002/cm.20461

Goldschmidt-Clermont, P. J., Furman, M. I., Wachsstock, D., Safer, D., Nachmias, V. T., & Pollard, T. D. (1992). The control of actin nucleotide exchange by thymosin beta 4 and profilin. A potential regulatory mechanism for actin polymerization in cells. *Molecular Biology of the Cell*, *3*(9), 1015–1024. https://doi.org/10.1091/mbc.3.9.1015

Goldstein, I. J., & So, L. L. (1965). Protein-carbonhydrate interaction. 3. Agar gel-diffusion studies on the interaction of Concanavalin A, a lectin isolated from jack bean, with polysaccharides. *Archives of Biochemistry and Biophysics*, *111*(2), 407–414. https://doi.org/10.1016/0003-9861(65)90203-1

Goudarzi, M., Tarbashevich, K., Mildner, K., Begemann, I., Garcia, J., Paksa, A., Reichman-Fried, M., Mahabaleshwar, H., Blaser, H., Hartwig, J., Zeuschner, D., Galic, M., Bagnat, M., Betz, T., & Raz, E. (2017). Bleb Expansion in Migrating Cells Depends on Supply of Membrane from Cell Surface Invaginations. *Developmental Cell*, *43*(5), 577-587.e5. https://doi.org/10.1016/j.devcel.2017.10.030

Gov, N. S., & Safran, S. A. (2005). Red Blood Cell Membrane Fluctuations and Shape Controlled by ATP-Induced Cytoskeletal Defects. *Biophysical Journal*, *88*(3), 1859–1874. https://doi.org/10.1529/biophysj.104.045328

Groulx, N., Boudreault, F., Orlov, S. N., & Grygorczyk, R. (2006). Membrane Reserves and Hypotonic Cell Swelling. *Journal of Membrane Biology*, *214*(1–2), 43–56. https://doi.org/10.1007/s00232-006-0080-8

Guimarães, C. F., Gasperini, L., Marques, A. P., & Reis, R. L. (2020). The stiffness of living tissues and its implications for tissue engineering. *Nature Reviews Materials*, *5*(5), 351–370. https://doi.org/10.1038/s41578-019-0169-1

Hackett, J. A., Dietmann, S., Murakami, K., Down, T. A., Leitch, H. G., & Surani, M. A. (2013). Synergistic Mechanisms of DNA Demethylation during Transition to Ground-State Pluripotency. *Stem Cell Reports*, *1*(6), 518–531.

https://doi.org/10.1016/j.stemcr.2013.11.010

Hackett, J. A., Huang, Y., Günesdogan, U., Gretarsson, K. A., Kobayashi, T., & Surani, M. A. (2018). Tracing the transitions from pluripotency to germ cell fate with CRISPR screening. *Nature Communications*, *9*(1), 4292. https://doi.org/10.1038/s41467-018-06230-0

Hackett, J. A., & Surani, M. A. (2014). Regulatory Principles of Pluripotency: From the Ground State Up. *Cell Stem Cell*, *15*(4), 416–430. https://doi.org/10.1016/j.stem.2014.09.015

Han, B., Zhou, R., Xia, C., & Zhuang, X. (2017). Structural organization of the actin-spectrin–based membrane skeleton in dendrites and soma of neurons. *Proceedings of the National Academy of Sciences*, *114*(32), E6678–E6685. https://doi.org/10.1073/pnas.1705043114

Haupt, A., & Minc, N. (2018). How cells sense their own shape – mechanisms to probe cell geometry and their implications in cellular organization and function. *Journal of Cell Science*, *131*(6), jcs214015. https://doi.org/10.1242/jcs.214015

Helfrich, W. (1973). Elastic Properties of Lipid Bilayers: Theory and Possible Experiments. *Zeitschrift Für Naturforschung C*, *28*(11–12), 693–703. https://doi.org/10.1515/znc-1973-11-1209

Hetmanski, J. H. R., de Belly, H., Busnelli, I., Waring, T., Nair, R. V., Sokleva, V., Dobre, O., Cameron, A., Gauthier, N., Lamaze, C., Swift, J., del Campo, A., Starborg, T., Zech, T., Goetz, J. G., Paluch, E. K., Schwartz, J. M., & Caswell, P. T. (2019). Membrane Tension Orchestrates Rear Retraction in Matrix-Directed Cell Migration. *Developmental Cell*, *51*(4), 460-475.e10. https://doi.org/10.1016/j.devcel.2019.09.006

Hochmuth, R. M., & Waugh, R. E. (1987). Erythrocyte Membrane Elasticity and Viscosity. *Annual Review of Physiology*, *49*(1), 209–219. https://doi.org/10.1146/annurev.ph.49.030187.001233

Hochmuth, Robert M., Shao, J. Y., Dai, J., & Sheetz, M. P. (1996). Deformation and flow of membrane into tethers extracted from neuronal growth cones. *Biophysical Journal*, *70*(1), 358–369. https://doi.org/10.1016/S0006-3495(96)79577-2

Hokanson, D. E., Laakso, J. M., Lin, T., Sept, D., & Ostap, E. M. (2006). Myo1c Binds

Phosphoinositides through a Putative Pleckstrin Homology Domain. *Molecular Biology of the Cell*, *17*(11), 4856–4865. https://doi.org/10.1091/mbc.e06-05-0449

Houk, A. R., Jilkine, A., Mejean, C. O., Boltyanskiy, R., Dufresne, E. R., Angenent, S. B., Altschuler, S. J., Wu, L. F., & Weiner, O. D. (2012). Membrane Tension Maintains Cell Polarity by Confining Signals to the Leading Edge during Neutrophil Migration. *Cell*, *148*(1–2), 175–188. https://doi.org/10.1016/j.cell.2011.10.050

Ingber, D. E. (2018). From mechanobiology to developmentally inspired engineering. *Philosophical Transactions of the Royal Society B: Biological Sciences*, *373*(1759), 20170323. https://doi.org/10.1098/rstb.2017.0323

Jähnig, F. (1996). What is the surface tension of a lipid bilayer membrane? *Biophysical Journal*, *71*(3), 1348–1349. https://doi.org/10.1016/S0006-3495(96)79336-0

Jainchill, J. L., Aaronson, S. A., & Todaro, G. J. (1969). Murine Sarcoma and Leukemia Viruses: Assay Using Clonal Lines of Contact-Inhibited Mouse Cells. *Journal of Virology*, *4*(5), 549–553. https://doi.org/10.1128/JVI.4.5.549-553.1969

Janson, I. A., & Putnam, A. J. (2015). Extracellular matrix elasticity and topography: Material-based cues that affect cell function via conserved mechanisms. *Journal of Biomedical Materials Research Part A*, *103*(3), 1246–1258. https://doi.org/10.1002/jbm.a.35254

Jarsch, I. K., Daste, F., & Gallop, J. L. (2016). Membrane curvature in cell biology: An integration of molecular mechanisms. *Journal of Cell Biology*, *214*(4), 375–387. https://doi.org/10.1083/jcb.201604003

Joanny, J. F., Kruse, K., Prost, J., & Ramaswamy, S. (2013). The actin cortex as an active wetting layer. *The European Physical Journal E*, *36*(5), 52. https://doi.org/10.1140/epje/i2013-13052-9

Johnson, M. H. (2009). From Mouse Egg to Mouse Embryo: Polarities, Axes, and Tissues. *Annual Review of Cell and Developmental Biology*, *25*(1), 483–512. https://doi.org/10.1146/annurev.cellbio.042308.113348

Kalkan, T., Olova, N., Roode, M., Mulas, C., Lee, H. J., Nett, I., Marks, H., Walker, R., Stunnenberg, H. G., Lilley, K. S., Nichols, J., Reik, W., Bertone, P., & Smith, A. (2017). Tracking the embryonic stem cell transition from ground state pluripotency.

Development, *144*(7), 1221–1234. https://doi.org/10.1242/dev.142711

Kamble, H., Barton, M. J., Jun, M., Park, S., & Nguyen, N.-T. (2016). Cell stretching devices as research tools: engineering and biological considerations. *Lab on a Chip*, *16*(17), 3193–3203. https://doi.org/10.1039/C6LC00607H

Kane, D., & Adams, R. (2002). Life at the Edge: Epiboly and Involution in the Zebrafish. In *Pattern formation in zebrafish* (pp. 117–135). Springer. https://doi.org/10.1007/978-3-540-46041-1_7

Kapus, A., & Janmey, P. (2013). Plasma membrane-cortical cytoskeleton interactions: A cell biology approach with biophysical considerations. *Comprehensive Physiology*, *3*(3), 1231–1281. https://doi.org/10.1002/cphy.c120015

Karimi, M., Johansson, S., Stach, D., Corcoran, M., Grandér, D., Schalling, M., Bakalkin, G., Lyko, F., Larsson, C., & Ekström, T. J. (2006). LUMA (LUminometric Methylation Assay)—A high throughput method to the analysis of genomic DNA methylation. *Experimental Cell Research*, *312*(11), 1989–1995. https://doi.org/10.1016/j.yexcr.2006.03.006

Keep, N. H., Winder, S. J., Moores, C. A., Walke, S., Norwood, F. L. M., & Kendrick-Jones, J. (1999). Crystal structure of the actin-binding region of utrophin reveals a head-to-tail dimer. *Structure*, *7*(12), 1539–1546. https://doi.org/10.1016/S0969-2126(00)88344-6

Kelkar, M., Bohec, P., & Charras, G. (2020). Mechanics of the cellular actin cortex: From signalling to shape change. *Current Opinion in Cell Biology*, *66*, 69–78. https://doi.org/10.1016/j.ceb.2020.05.008

Keren, K., & Shemesh, T. (2017). Buckle up: Membrane tension drives lamellipodial network compression and adhesion deposition. *Journal of Cell Biology*, *216*(9), 2619–2621. https://doi.org/10.1083/jcb.201706111

Koike, M., Sakaki, S., Amano, Y., & Kurosawa, H. (2007). Characterization of embryoid bodies of mouse embryonic stem cells formed under various culture conditions and estimation of differentiation status of such bodies. *Journal of Bioscience and Bioengineering*, *104*(4), 294–299. https://doi.org/https://doi.org/10.1263/jbb.104.294

Korotkevich, E., Niwayama, R., Courtois, A., Friese, S., Berger, N., Buchholz, F., & Hiiragi, T. (2017). The Apical Domain Is Required and Sufficient for the First Lineage Segregation

in the Mouse Embryo. *Developmental Cell*, *40*(3), 235-247.e7. https://doi.org/10.1016/j.devcel.2017.01.006

Kovar, D. R., & Pollard, T. D. (2004). Progressing actin: Formin as a processive elongation machine. *Nature Cell Biology*, *6*(12), 1158–1159. https://doi.org/10.1038/ncb1204-1158

Kovářová, M., Tolar, P., Arudchandran, R., Dráberová, L., Rivera, J., & Dráber, P. (2001). Structure-Function Analysis of Lyn Kinase Association with Lipid Rafts and Initiation of Early Signaling Events after Fcε Receptor I Aggregation. *Molecular and Cellular Biology*, *21*(24), 8318–8328. https://doi.org/10.1128/MCB.21.24.8318-8328.2001

Kozlov, M. M., & Chernomordik, L. V. (2015). Membrane tension and membrane fusion. *Current Opinion in Structural Biology*, *33*, 61–67. https://doi.org/10.1016/j.sbi.2015.07.010

Krieg, M., Helenius, J., Heisenberg, C.-P., & Muller, D. J. (2008). A Bond for a Lifetime: Employing Membrane Nanotubes from Living Cells to Determine Receptor-Ligand Kinetics. *Angewandte Chemie International Edition*, *47*(50), 9775–9777. https://doi.org/10.1002/anie.200803552

Kruse, K., Joanny, J. F., Jülicher, F., Prost, J., & Sekimoto, K. (2004). Asters, Vortices, and Rotating Spirals in Active Gels of Polar Filaments. *Physical Review Letters*, *92*(7), 078101. https://doi.org/10.1103/PhysRevLett.92.078101

Kumar, R., Saha, S., & Sinha, B. (2019). Cell spread area and traction forces determine myosin-II-based cortex thickness regulation. *Biochimica et Biophysica Acta (BBA) - Molecular Cell Research*, *1866*(12), 118516. https://doi.org/10.1016/j.bbamcr.2019.07.011

Kunda, P., Pelling, A. E., Liu, T., & Baum, B. (2008). Moesin Controls Cortical Rigidity, Cell Rounding, and Spindle Morphogenesis during Mitosis. *Current Biology*, *18*(2), 91–101. https://doi.org/10.1016/j.cub.2007.12.051

Kusumi, A., Fujiwara, T. K., Chadda, R., Xie, M., Tsunoyama, T. A., Kalay, Z., Kasai, R. S., & Suzuki, K. G. N. (2012). Dynamic Organizing Principles of the Plasma Membrane that Regulate Signal Transduction: Commemorating the Fortieth Anniversary of Singer and Nicolson's Fluid-Mosaic Model. *Annual Review of Cell and Developmental Biology*,

28(1), 215–250. https://doi.org/10.1146/annurev-cellbio-100809-151736

Kusumi, A., Nakada, C., Ritchie, K., Murase, K., Suzuki, K., Murakoshi, H., Kasai, R. S., Kondo, J., & Fujiwara, T. (2005). Paradigm Shift of the Plasma Membrane Concept from the Two-Dimensional Continuum Fluid to the Partitioned Fluid: High-Speed Single-Molecule Tracking of Membrane Molecules. *Annual Review of Biophysics and Biomolecular Structure*, *34*(1), 351–378. https://doi.org/10.1146/annurev.biophys.34.040204.144637

Kusumi, A., Suzuki, K. G. N., Kasai, R. S., Ritchie, K., & Fujiwara, T. K. (2011). Hierarchical mesoscale domain organization of the plasma membrane. *Trends in Biochemical Sciences*, *36*(11), 604–615. https://doi.org/10.1016/j.tibs.2011.08.001

Kwok, R., & Evans, E. (1981). Thermoelasticity of large lecithin bilayer vesicles. *Biophysical Journal*, *35*(3), 637–652. https://doi.org/10.1016/S0006-3495(81)84817-5

Laevsky, G. (2003). Cross-linking of actin filaments by myosin II is a major contributor to cortical integrity and cell motility in restrictive environments. *Journal of Cell Science*, *116*(18), 3761–3770. https://doi.org/10.1242/jcs.00684

Laliberte, A., & Gicquaud, C. (1988). Polymerization of actin by positively charged liposomes. *The Journal of Cell Biology*, *106*(4), 1221–1227. https://doi.org/10.1083/jcb.106.4.1221

Lancaster, O. M., Le Berre, M., Dimitracopoulos, A., Bonazzi, D., Zlotek-Zlotkiewicz, E., Picone, R., Duke, T., Piel, M., & Baum, B. (2013). Mitotic Rounding Alters Cell Geometry to Ensure Efficient Bipolar Spindle Formation. *Developmental Cell*, *25*(3), 270–283. https://doi.org/10.1016/j.devcel.2013.03.014

Landgraf, K. E., Malmberg, N. J., & Falke, J. J. (2008). Effect of PIP 2 Binding on the Membrane Docking Geometry of PKCα C2 Domain: An EPR Site-Directed Spin-Labeling and Relaxation Study †. *Biochemistry*, *47*(32), 8301–8316. https://doi.org/10.1021/bi800711t

Laplaud, V., Levernier, N., Pineau, J., San-Roman, M., Barbier, L., Saez, P. J., Lennon-Dumenil, A.-M., Vargas, P., Kruse, K., ROURE, O. DU, Piel, M., & Heuvingh, J. (2020). Pinching the cortex of live cells reveals thickness instabilities caused by Myosin II motors. *BioRxiv*, 2020.09.28.316729.

https://doi.org/https://doi.org/10.1101/2020.09.28.316729doi:

Lecuit, T., & Lenne, P.-F. (2007). Cell surface mechanics and the control of cell shape, tissue patterns and morphogenesis. *Nature Reviews Molecular Cell Biology*, *8*(8), 633–644. https://doi.org/10.1038/nrm2222

Legg, J. W., & Isacke, C. M. (1998). Identification and functional analysis of the ezrin-binding site in the hyaluronan receptor, CD44. *Current Biology*, *8*(12), 705–708. https://doi.org/10.1016/S0960-9822(98)70277-5

Leitch, H. G., McEwen, K. R., Turp, A., Encheva, V., Carroll, T., Grabole, N., Mansfield, W., Nashun, B., Knezovich, J. G., Smith, A., Surani, M. A., & Hajkova, P. (2013). Naive pluripotency is associated with global DNA hypomethylation. *Nature Structural & Molecular Biology*, *20*(3), 311–316. https://doi.org/10.1038/nsmb.2510

Lekomtsev, S., Su, K.-C., Pye, V. E., Blight, K., Sundaramoorthy, S., Takaki, T., Collinson, L. M., Cherepanov, P., Divecha, N., & Petronczki, M. (2012). Centralspindlin links the mitotic spindle to the plasma membrane during cytokinesis. *Nature*, *492*(7428), 276–279. https://doi.org/10.1038/nature11773

Lens, S. M. A., & Medema, R. H. (2019). Cytokinesis defects and cancer. *Nature Reviews Cancer*, *19*(1), 32–45. https://doi.org/10.1038/s41568-018-0084-6

Levskaya, A., Weiner, O. D., Lim, W. A., & Voigt, C. A. (2009). Spatiotemporal control of cell signalling using a light-switchable protein interaction. *Nature*, *461*(7266), 997–1001. https://doi.org/10.1038/nature08446

Li, G., Wen, Q., & Tang, J. X. (2005). Single filament electrophoresis of F-actin and filamentous virus fd. *The Journal of Chemical Physics*, *122*(10), 104708. https://doi.org/10.1063/1.1859284

Li, J., Wang, Z., Chu, Q., Jiang, K., Li, J., & Tang, N. (2018). The Strength of Mechanical Forces Determines the Differentiation of Alveolar Epithelial Cells. *Developmental Cell*, *44*(3), 297-312.e5. https://doi.org/10.1016/j.devcel.2018.01.008

Li, Q., Nance, M. R., Kulikauskas, R., Nyberg, K., Fehon, R., Karplus, P. A., Bretscher, A., & Tesmer, J. J. G. (2007). Self-masking in an Intact ERM-merlin Protein: An Active Role for the Central α-Helical Domain. *Journal of Molecular Biology*, *365*(5), 1446–1459. https://doi.org/10.1016/j.jmb.2006.10.075

Lieber, M., Todaro, G., Smith, B., Szakal, A., & Nelson-Rees, W. (1976). A continuous tumor-cell line from a human lung carcinoma with properties of type II alveolar epithelial cells. *International Journal of Cancer*, *17*(1), 62–70. https://doi.org/10.1002/ijc.2910170110

Lim, C. T., Zhou, E. H., & Quek, S. T. (2006). Mechanical models for living cells—a review. *Journal of Biomechanics*, *39*(2), 195–216. https://doi.org/10.1016/j.jbiomech.2004.12.008

Lin, D. C., Shreiber, D. I., Dimitriadis, E. K., & Horkay, F. (2009). Spherical indentation of soft matter beyond the Hertzian regime: numerical and experimental validation of hyperelastic models. *Biomechanics and Modeling in Mechanobiology*, *8*(5), 345–358. https://doi.org/10.1007/s10237-008-0139-9

Ling, M., Sunesson, L., & Larsson, C. (2007). Comparison of the PKCα and the PKCε C1b Domains: Identification of Residues Critical for PKCε-mediated Neurite Induction. *Journal of Molecular Biology*, *368*(4), 951–965. https://doi.org/10.1016/j.jmb.2007.02.073

Liu, A. P., Richmond, D. L., Maibaum, L., Pronk, S., Geissler, P. L., & Fletcher, D. A. (2008). Membrane-induced bundling of actin filaments. *Nature Physics*, *4*(10), 789–793. https://doi.org/10.1038/nphys1071

Liu, H., Wu, Z., Shi, X., Li, W., Liu, C., Wang, D., Ye, X., Liu, L., Na, J., Cheng, H., & Chen, L. (2013). Atypical PKC, regulated by Rho GTPases and Mek/Erk, phosphorylates Ezrin during eight-cell embryocompaction. *Developmental Biology*, *375*(1), 13–22. https://doi.org/10.1016/j.ydbio.2013.01.002

Liu, Yin, Belkina, N. V., Park, C., Nambiar, R., Loughhead, S. M., Patino-Lopez, G., Ben-Aissa, K., Hao, J.-J., Kruhlak, M. J., Qi, H., von Andrian, U. H., Kehrl, J. H., Tyska, M. J., & Shaw, S. (2012). Constitutively active ezrin increases membrane tension, slows migration, and impedes endothelial transmigration of lymphocytes in vivo in mice. *Blood*, *119*(2), 445–453. https://doi.org/10.1182/blood-2011-07-368860

Liu, Yinan, & Robinson, D. (2018). Recent advances in cytokinesis: understanding the molecular underpinnings. *F1000Research*, *7*, 1849. https://doi.org/10.12688/f1000research.16502.1

Louvet, S., Aghion, J., Maria, S. A., Mangeat, P., & Maro, B. (1995). Ezrin becomes restricted to outer cells following asymmetric division in the preimplantation mouse embryo. *Biology of the Cell*, *84*(1–2), 109–109. https://doi.org/10.1016/0248-4900(96)81421-3

Maître, J.-L., Niwayama, R., Turlier, H., Nédélec, F., & Hiiragi, T. (2015). Pulsatile cell-autonomous contractility drives compaction in the mouse embryo. *Nature Cell Biology*, *17*(7), 849–855. https://doi.org/10.1038/ncb3185

Maître, J.-L., Turlier, H., Illukkumbura, R., Eismann, B., Niwayama, R., Nédélec, F., & Hiiragi, T. (2016). Asymmetric division of contractile domains couples cell positioning and fate specification. *Nature*, *536*(7616), 344–348. https://doi.org/10.1038/nature18958

Manchanda, N., Lyubimova, A., Ho, H. Y. H., James, M. F., Gusella, J. F., Ramesh, N., Snapper, S. B., & Ramesh, V. (2005). The NF2 tumor suppressor merlin and the ERM proteins interact with N-WASP and regulate its actin polymerization function. *Journal of Biological Chemistry*, *280*(13), 12517–12522. https://doi.org/10.1074/jbc.C400583200

Marques, S. P. C., & Creus, G. J. (2012). Computational Viscoelasticity. In *SpringerBriefs in Applied Sciences and Technology* (Issue 9783642253102). Springer Berlin Heidelberg. https://doi.org/10.1007/978-3-642-25311-9

Martin, G. R. (1981). Isolation of a pluripotent cell line from early mouse embryos cultured in medium conditioned by teratocarcinoma stem cells. *Proceedings of the National Academy of Sciences*, *78*(12), 7634–7638. https://doi.org/10.1073/pnas.78.12.7634

Mascetti, V. L., & Pedersen, R. A. (2016). Contributions of Mammalian Chimeras to Pluripotent Stem Cell Research. *Cell Stem Cell*, *19*(2), 163–175. https://doi.org/10.1016/j.stem.2016.07.018

Mayer, M., Depken, M., Bois, J. S., Jülicher, F., & Grill, S. W. (2010). Anisotropies in cortical tension reveal the physical basis of polarizing cortical flows. *Nature*, *467*(7315), 617–621. https://doi.org/10.1038/nature09376

Mikkelsen, A., Stokke, B. T., & Elgsaeter, A. (1984). An electro-optic study of human erythrocyte spectrin dimers. *Biochimica et Biophysica Acta (BBA) - Protein Structure and Molecular Enzymology*, *786*(1–2), 95–102. https://doi.org/10.1016/0167-4838(84)90158-4

Minami, Y., Kono, T., Miyazaki, T., & Taniguchi, T. (1993). The IL-2 Receptor Complex: Its Structure, Function, and Target Genes. *Annual Review of Immunology*, *11*(1), 245–268. https://doi.org/10.1146/annurev.iy.11.040193.001333

Moeendarbary, E., & Harris, A. R. (2014). Cell mechanics: principles, practices, and prospects. *Wiley Interdisciplinary Reviews: Systems Biology and Medicine*, *6*(5), 371–388. https://doi.org/10.1002/wsbm.1275

Monzel, C., & Sengupta, K. (2016). Measuring shape fluctuations in biological membranes. *Journal of Physics D: Applied Physics*, *49*(24), 243002. https://doi.org/10.1088/0022-3727/49/24/243002

Morone, N., Fujiwara, T., Murase, K., Kasai, R. S., Ike, H., Yuasa, S., Usukura, J., & Kusumi, A. (2006). Three-dimensional reconstruction of the membrane skeleton at the plasma membrane interface by electron tomography. *Journal of Cell Biology*, *174*(6), 851–862. https://doi.org/10.1083/jcb.200606007

Morris, C. E., & Homann, U. (2001). Cell Surface Area Regulation and Membrane Tension. *The Journal of Membrane Biology*, *179*(2), 79–102. https://doi.org/10.1007/s002320010040

Mulas, C., Kalkan, T., von Meyenn, F., Leitch, H. G., Nichols, J., & Smith, A. (2019). Defined conditions for propagation and manipulation of mouse embryonic stem cells. *Development*, *146*(6), dev173146. https://doi.org/10.1242/dev.173146

Muncie, J. M., & Weaver, V. M. (2018). The Physical and Biochemical Properties of the Extracellular Matrix Regulate Cell Fate. In *Current Topics in Developmental Biology* (1st ed., Vol. 130, pp. 1–37). Elsevier Inc. https://doi.org/10.1016/bs.ctdb.2018.02.002

Munro, E., Nance, J., & Priess, J. R. (2004). Cortical Flows Powered by Asymmetrical Contraction Transport PAR Proteins to Establish and Maintain Anterior-Posterior Polarity in the Early C. elegans Embryo. *Developmental Cell*, *7*(3), 413–424. https://doi.org/10.1016/j.devcel.2004.08.001

Murray, P., Prewitz, M., Hopp, I., Wells, N., Zhang, H., Cooper, A., Parry, K. L., Short, R., Antoine, D. J., & Edgar, D. (2013). The self-renewal of mouse embryonic stem cells is regulated by cell–substratum adhesion and cell spreading. *The International Journal of Biochemistry & Cell Biology*, *45*(11), 2698–2705.

https://doi.org/10.1016/j.biocel.2013.07.001

Mutz, M., & Helfrich, W. (1990). Bending rigidities of some biological model membranes as obtained from the Fourier analysis of contour sections. *Journal de Physique*, *51*(10), 991–1001. https://doi.org/10.1051/jphys:019900051010099100

Nambiar, R., McConnell, R. E., & Tyska, M. J. (2009). Control of cell membrane tension by myosin-I. *Proceedings of the National Academy of Sciences of the United States of America*, *106*(29), 11972–11977. https://doi.org/10.1073/pnas.0901641106

Nawaz, S., Sánchez, P., Bodensiek, K., Li, S., Simons, M., & Schaap, I. A. T. (2012). Cell Visco-Elasticity Measured with AFM and Optical Trapping at Sub-Micrometer Deformations. *PLoS ONE*, *7*(9), e45297. https://doi.org/10.1371/journal.pone.0045297

Nguyen-Ngoc, T., Afshar, K., & Gönczy, P. (2007). Coupling of cortical dynein and Gα proteins mediates spindle positioning in Caenorhabditis elegans. *Nature Cell Biology*, *9*(11), 1294–1302. https://doi.org/10.1038/ncb1649

Nicolson, G. L. (2014). The Fluid - Mosaic Model of Membrane Structure: Still relevant to understanding the structure, function and dynamics of biological membranes after more than 40 years. *Biochimica et Biophysica Acta - Biomembranes*, *1838*(6), 1451–1466. https://doi.org/10.1016/j.bbamem.2013.10.019

Niwa, H. (2007). How is pluripotency determined and maintained? *Development*, *134*(4), 635–646. https://doi.org/10.1242/dev.02787

North, T. E., Goessling, W., Peeters, M., Li, P., Ceol, C., Lord, A. M., Weber, G. J., Harris, J., Cutting, C. C., Huang, P., Dzierzak, E., & Zon, L. I. (2009). Hematopoietic Stem Cell Development Is Dependent on Blood Flow. *Cell*, *137*(4), 736–748. https://doi.org/10.1016/j.cell.2009.04.023

Oegema, K., Savoian, M. S., Mitchison, T. J., & Field, C. M. (2000). Functional Analysis of a Human Homologue of the Drosophila Actin Binding Protein Anillin Suggests a Role in Cytokinesis. *Journal of Cell Biology*, *150*(3), 539–552. https://doi.org/10.1083/jcb.150.3.539

Ono, S. (2007). Mechanism of Depolymerization and Severing of Actin Filaments and Its Significance in Cytoskeletal Dynamics. In *International Review of Cytology* (Vol. 258, Issue 07, pp. 1–82). https://doi.org/10.1016/S0074-7696(07)58001-0

Ott, A., Magnasco, M., Simon, A., & Libchaber, A. (1993). Measurement of the persistence length of polymerized actin using fluorescence microscopy. *Physical Review E*, *48*(3), R1642.

Paluch, E., & Heisenberg, C.-P. (2009). Biology and Physics of Cell Shape Changes in Development. *Current Biology*, *19*(17), R790–R799. https://doi.org/10.1016/j.cub.2009.07.029

Paluch, E., Piel, M., Prost, J., Bornens, M., & Sykes, C. (2005). Cortical Actomyosin Breakage Triggers Shape Oscillations in Cells and Cell Fragments. *Biophysical Journal*, *89*(1), 724–733. https://doi.org/10.1529/biophysj.105.060590

Park, Y., Best, C. A., Auth, T., Gov, N. S., Safran, S. A., Popescu, G., Suresh, S., & Feld, M. S. (2010). Metabolic remodeling of the human red blood cell membrane. *Proceedings of the National Academy of Sciences*, *107*(4), 1289–1294. https://doi.org/10.1073/pnas.0910785107

Pasternak, C., & Elson, E. L. (1985). Lymphocyte mechanical response triggered by cross-linking surface receptors. *The Journal of Cell Biology*, *100*(3), 860–872. https://doi.org/10.1083/jcb.100.3.860

Pathak, M. M., Nourse, J. L., Tran, T., Hwe, J., Arulmoli, J., Le, D. T. T., Bernardis, E., Flanagan, L. A., & Tombola, F. (2014). Stretch-activated ion channel Piezo1 directs lineage choice in human neural stem cells. *Proceedings of the National Academy of Sciences*, *111*(45), 16148–16153. https://doi.org/10.1073/pnas.1409802111

Pearson, M. A., Reczek, D., Bretscher, A., & Karplus, P. A. (2000). Structure of the ERM Protein Moesin Reveals the FERM Domain Fold Masked by an Extended Actin Binding Tail Domain. *Cell*, *101*(3), 259–270. https://doi.org/10.1016/S0092-8674(00)80836-3

Pedroni, P., & Sconfietti, S. (2020). A new Monte Carlo-based fitting method. *Journal of Physics G: Nuclear and Particle Physics*, *47*(5), 054001. https://doi.org/10.1088/1361-6471/ab6c31

Pelling, A. E., & Horton, M. A. (2008). An historical perspective on cell mechanics. *Pflügers Archiv - European Journal of Physiology*, *456*(1), 3–12. https://doi.org/10.1007/s00424-007-0405-1

Pestonjamasp, K., Amieva, M. R., Strassel, C. P., Nauseef, W. M., Furthmayr, H., & Luna, E. J.

(1995). Moesin, ezrin, and p205 are actin-binding proteins associated with neutrophil plasma membranes. *Molecular Biology of the Cell*, *6*(3), 247–259. https://doi.org/10.1091/mbc.6.3.247

Pharr, G. M., Oliver, W. C., & Brotzen, F. R. (1992). On the generality of the relationship among contact stiffness, contact area, and elastic modulus during indentation. *Journal of Materials Research*, *7*(3), 613–617. https://doi.org/10.1557/JMR.1992.0613

Pollard, T. D., Blanchoin, L., & Mullins, R. D. (2001). Actin dynamics. *Journal of Cell Science*, *114*(1), 3.

Pollard, Thomas D. (2016). Actin and Actin-Binding Proteins. *Cold Spring Harbor Perspectives in Biology*, *8*(8), a018226. https://doi.org/10.1101/cshperspect.a018226

Pontes, B., Ayala, Y., Fonseca, A. C. C., Romão, L. F., Amaral, R. F., Salgado, L. T., Lima, F. R., Farina, M., Viana, N. B., Moura-Neto, V., & Nussenzveig, H. M. (2013). Membrane Elastic Properties and Cell Function. *PLoS ONE*, *8*(7), e67708. https://doi.org/10.1371/journal.pone.0067708

Pontes, B., Monzo, P., & Gauthier, N. C. (2017). Membrane tension: A challenging but universal physical parameter in cell biology. *Seminars in Cell & Developmental Biology*, *71*, 30–41. https://doi.org/10.1016/j.semcdb.2017.08.030

Ponuwei, G. A. (2016). A glimpse of the ERM proteins. *Journal of Biomedical Science*, *23*(1), 35. https://doi.org/10.1186/s12929-016-0246-3

Prost, J., Jülicher, F., & Joanny, J.-F. (2015). Active gel physics. *Nature Physics*, *11*(2), 111–117. https://doi.org/10.1038/nphys3224

Ramanathan, S. P., Helenius, J., Stewart, M. P., Cattin, C. J., Hyman, A. A., & Muller, D. J. (2015). Cdk1-dependent mitotic enrichment of cortical myosin II promotes cell rounding against confinement. *Nature Cell Biology*, *17*(2), 148–159. https://doi.org/10.1038/ncb3098

Ramkumar, N., & Baum, B. (2016). Coupling changes in cell shape to chromosome segregation. *Nature Reviews Molecular Cell Biology*, *17*(8), 511–521. https://doi.org/10.1038/nrm.2016.75

Rand, R. P. (1964). Mechanical Properties of the Red Cell Membrane. *Biophysical Journal*, *4*(4), 303–316. https://doi.org/10.1016/S0006-3495(64)86784-9

Rasmussen, M., Alexander, R. T., Darborg, B. V., Møbjerg, N., Hoffmann, E. K., Kapus, A., & Pedersen, S. F. (2008). Osmotic cell shrinkage activates ezrin/radixin/moesin (ERM) proteins: activation mechanisms and physiological implications. *American Journal of Physiology-Cell Physiology*, *294*(1), C197–C212. https://doi.org/10.1152/ajpcell.00268.2007

Raucher, D., & Sheetz, M. P. (1999). Characteristics of a Membrane Reservoir Buffering Membrane Tension. *Biophysical Journal*, *77*(4), 1992–2002. https://doi.org/10.1016/S0006-3495(99)77040-2

Raucher, D., Stauffer, T., Chen, W., Shen, K., Guo, S., York, J. D., Sheetz, M. P., & Meyer, T. (2000). Phosphatidylinositol 4,5-Bisphosphate Functions as a Second Messenger that Regulates Cytoskeleton–Plasma Membrane Adhesion. *Cell*, *100*(2), 221–228. https://doi.org/10.1016/S0092-8674(00)81560-3

Renault, A., Lenne, P.-F., Zakri, C., Aradian, A., Vénien-Bryan, C., & Amblard, F. (1999). Surface-Induced Polymerization of Actin. *Biophysical Journal*, *76*(3), 1580–1590. https://doi.org/10.1016/S0006-3495(99)77317-0

Reymann, A.-C., Staniscia, F., Erzberger, A., Salbreux, G., & Grill, S. W. (2016). Cortical flow aligns actin filaments to form a furrow. *ELife*, *5*(OCTOBER2016), 1–25. https://doi.org/10.7554/eLife.17807

Ribatti, D. (2018). An historical note on the cell theory. *Experimental Cell Research*, *364*(1), 1–4. https://doi.org/10.1016/j.yexcr.2018.01.038

Riedl, J., Crevenna, A. H., Kessenbrock, K., Yu, J. H., Neukirchen, D., Bista, M., Bradke, F., Jenne, D., Holak, T. A., Werb, Z., Sixt, M., & Wedlich-Soldner, R. (2008). Lifeact: a versatile marker to visualize F-actin. *Nature Methods*, *5*(7), 605–607. https://doi.org/10.1038/nmeth.1220

Rogovina, L. Z., Vasil'ev, V. G., & Braudo, E. E. (2008). Definition of the concept of polymer gel. *Polymer Science Series C*, *50*(1), 85–92. https://doi.org/10.1134/S1811238208010050

Rosenbluth, M. J., Lam, W. A., & Fletcher, D. A. (2006). Force Microscopy of Nonadherent Cells: A Comparison of Leukemia Cell Deformability. *Biophysical Journal*, *90*(8), 2994–3003. https://doi.org/10.1529/biophysj.105.067496

Rotsch, C., & Radmacher, M. (2000). Drug-Induced Changes of Cytoskeletal Structure and Mechanics in Fibroblasts: An Atomic Force Microscopy Study. *Biophysical Journal*, *78*(1), 520–535. https://doi.org/10.1016/S0006-3495(00)76614-8

Rouiller, I., Xu, X.-P., Amann, K. J., Egile, C., Nickell, S., Nicastro, D., Li, R., Pollard, T. D., Volkmann, N., & Hanein, D. (2008). The structural basis of actin filament branching by the Arp2/3 complex. *Journal of Cell Biology*, *180*(5), 887–895. https://doi.org/10.1083/jcb.200709092

Rouven Brückner, B., Pietuch, A., Nehls, S., Rother, J., & Janshoff, A. (2015). Ezrin is a Major Regulator of Membrane Tension in Epithelial Cells. *Scientific Reports*, *5*(1), 14700. https://doi.org/10.1038/srep14700

Ruskamo, S., & Ylänne, J. (2009). Structure of the human filamin A actin-binding domain. *Acta Crystallographica Section D Biological Crystallography*, *65*(11), 1217–1221. https://doi.org/10.1107/S0907444909037330

Russell, W. C., Graham, F. L., Smiley, J., & Nairn, R. (1977). Characteristics of a Human Cell Line Transformed by DNA from Human Adenovirus Type 5. *Journal of General Virology*, *36*(1), 59–72. https://doi.org/10.1099/0022-1317-36-1-59

Safran, S. A. (2018). *Statistical Thermodynamics of Surfaces, Interfaces, and Membranes* (pp. 55–74). CRC Press. https://doi.org/10.1201/9780429497131

Salbreux, G., Charras, G., & Paluch, E. (2012). Actin cortex mechanics and cellular morphogenesis. *Trends in Cell Biology*, *22*(10), 536–545. https://doi.org/10.1016/j.tcb.2012.07.001

Salbreux, G., Prost, J., & Joanny, J. F. (2009). Hydrodynamics of Cellular Cortical Flows and the Formation of Contractile Rings. *Physical Review Letters*, *103*(5), 058102. https://doi.org/10.1103/PhysRevLett.103.058102

Sato, N., Funayama, N., Nagafuchi, A., Yonemura, S., Tsukita, S., & Tsukita, S. (1992). A gene family consisting of ezrin, radixin and moesin. Its specific localization at actin filament/plasma membrane association sites. *Journal of Cell Science*, *103 (Pt 1*(1), 131–143. http://www.ncbi.nlm.nih.gov/pubmed/1429901

Satterwhite, L. L., & Pollard, T. D. (1992). Cytokinesis. *Current Opinion in Cell Biology*, *4*(1), 43–52. https://doi.org/10.1016/0955-0674(92)90057-J

Scarpa, E., Finet, C., Blanchard, G. B., & Sanson, B. (2018). Actomyosin-Driven Tension at Compartmental Boundaries Orients Cell Division Independently of Cell Geometry In Vivo. *Developmental Cell*, *47*(6), 727-740.e6. https://doi.org/10.1016/j.devcel.2018.10.029

Schroer, C. F. E., Baldauf, L., van Buren, L., Wassenaar, T. A., Melo, M. N., Koenderink, G. H., & Marrink, S. J. (2020). Charge-dependent interactions of monomeric and filamentous actin with lipid bilayers. *Proceedings of the National Academy of Sciences*, *117*(11), 5861–5872. https://doi.org/10.1073/pnas.1914884117

Severson, A. F., Baillie, D. L., & Bowerman, B. (2002). A Formin Homology Protein and a Profilin Are Required for Cytokinesis and Arp2/3-Independent Assembly of Cortical Microfilaments in C. elegans. *Current Biology*, *12*(24), 2066–2075. https://doi.org/10.1016/S0960-9822(02)01355-6

Shaner, N. C., Campbell, R. E., Steinbach, P. A., Giepmans, B. N. G., Palmer, A. E., & Tsien, R. Y. (2004). Improved monomeric red, orange and yellow fluorescent proteins derived from Discosoma sp. red fluorescent protein. *Nature Biotechnology*, *22*(12), 1567–1572. https://doi.org/10.1038/nbt1037

Sharma, C. P., Ezzell, R. M., & Arnaout, M. A. (1995). Direct interaction of filamin (ABP-280) with the beta 2-integrin subunit CD18. *Journal of Immunology (Baltimore, Md. : 1950)*, *154*(7), 3461–3470. http://www.ncbi.nlm.nih.gov/pubmed/7534799

Sheetz, M. P. (2001). Cell control by membrane–cytoskeleton adhesion. *Nature Reviews Molecular Cell Biology*, *2*(5), 392–396. https://doi.org/10.1038/35073095

Sheetz, M. P., Sable, J. E., & Döbereiner, H. G. (2006). Continuous membrane-cytoskeleton adhesion requires continuous accommodation to lipid and cytoskeleton dynamics. *Annual Review of Biophysics and Biomolecular Structure*, *35*, 417–434. https://doi.org/10.1146/annurev.biophys.35.040405.102017

Sheetz, M. P., Turney, S., Qian, H., & Elson, E. L. (1989). Nanometre-level analysis demonstrates that lipid flow does not drive membrane glycoprotein movements. *Nature*, *340*(6231), 284–288. https://doi.org/10.1038/340284a0

Shi, Z., Graber, Z. T., Baumgart, T., Stone, H. A., & Cohen, A. E. (2018). Cell Membranes Resist Flow. *Cell*, *175*(7), 1769-1779.e13. https://doi.org/10.1016/j.cell.2018.09.054

Singer, S. J., & Nicolson, G. L. (1972). The Fluid Mosaic Model of the Structure of Cell Membranes. *Science*, *175*(4023), 720–731. https://doi.org/10.1126/science.175.4023.720

Sitarska, E., & Diz-Muñoz, A. (2020). Pay attention to membrane tension: Mechanobiology of the cell surface. *Current Opinion in Cell Biology*, *66*, 11–18. https://doi.org/10.1016/j.ceb.2020.04.001

Smith, B. A., Daugherty-Clarke, K., Goode, B. L., & Gelles, J. (2013). Pathway of actin filament branch formation by Arp2/3 complex revealed by single-molecule imaging. *Proceedings of the National Academy of Sciences*, *110*(4), 1285–1290. https://doi.org/10.1073/pnas.1211164110

Smith, P. R., Morrison, I. E. G., Wilson, K. M., Fernández, N., & Cherry, R. J. (1999). Anomalous Diffusion of Major Histocompatibility Complex Class I Molecules on HeLa Cells Determined by Single Particle Tracking. *Biophysical Journal*, *76*(6), 3331–3344. https://doi.org/10.1016/S0006-3495(99)77486-2

St-Onge, D., & Gicquaud, C. (1989). Evidence of direct interaction between actin and membrane lipids. *Biochemistry and Cell Biology*, *67*(6), 297–300. https://doi.org/10.1139/o89-045

Stahlhut, M., & van Deurs, B. (2000). Identification of Filamin as a Novel Ligand for Caveolin-1: Evidence for the Organization of Caveolin-1–associated Membrane Domains by the Actin Cytoskeleton. *Molecular Biology of the Cell*, *11*(1), 325–337. https://doi.org/10.1091/mbc.11.1.325

Stefani, C., Gonzalez-Rodriguez, D., Senju, Y., Doye, A., Efimova, N., Janel, S., Lipuma, J., Tsai, M. C., Hamaoui, D., Maddugoda, M. P., Cochet-Escartin, O., Prévost, C., Lafont, F., Svitkina, T., Lappalainen, P., Bassereau, P., & Lemichez, E. (2017). Ezrin enhances line tension along transcellular tunnel edges via NMIIa driven actomyosin cable formation. *Nature Communications*, *8*(1), 15839. https://doi.org/10.1038/ncomms15839

Sumner, J. B. (1919). The globulins of the jack bean, Canavalia Ensiformis. *Journal of Biological Chemistry*, *37*(1), 137–142.

Sun, M., Northup, N., Marga, F., Huber, T., Byfield, F. J., Levitan, I., & Forgacs, G. (2007). The effect of cellular cholesterol on membrane-cytoskeleton adhesion. *Journal of Cell*

Science, *120*(13), 2223–2231. https://doi.org/10.1242/jcs.001370

Svitkina, T. M. (1989). Cytoskeleton organization in cultured epithelial cells. *Tsitologiya*, *31*, 1435–1440.

Svitkina, Tatyana M. (2020). Actin Cell Cortex: Structure and Molecular Organization. *Trends in Cell Biology*, *30*(7), 556–565. https://doi.org/10.1016/j.tcb.2020.03.005

Tait, L., Soule, H. D., & Russo, J. (1990). Ultrastructural and immunocytochemical characterization of an immortalized human breast epithelial cell line, MCF-10. *Cancer Research*, *50*(18), 6087–6094. http://www.ncbi.nlm.nih.gov/pubmed/1697506

Takahashi, S., Kobayashi, S., & Hiratani, I. (2018). Epigenetic differences between naïve and primed pluripotent stem cells. *Cellular and Molecular Life Sciences*, *75*(7), 1191–1203. https://doi.org/10.1007/s00018-017-2703-x

Tamma, G., Procino, G., Svelto, M., & Valenti, G. (2007). Hypotonicity causes actin reorganization and recruitment of the actin-binding ERM protein moesin in membrane protrusions in collecting duct principal cells. *American Journal of Physiology-Cell Physiology*, *292*(4), C1476–C1484. https://doi.org/10.1152/ajpcell.00375.2006

Taubenberger, A. V., Baum, B., & Matthews, H. K. (2020). The Mechanics of Mitotic Cell Rounding. *Frontiers in Cell and Developmental Biology*, *8*, 687. https://doi.org/10.3389/fcell.2020.00687

Thompson, D. (1917). On growth and form (Edition 1). In *On growth and form.* (1st ed.). Cambridge University Press.

Toyooka, Y., Shimosato, D., Murakami, K., Takahashi, K., & Niwa, H. (2008). Identification and characterization of subpopulations in undifferentiated ES cell culture. *Development*, *135*(5), 909–918. https://doi.org/10.1242/dev.017400

Tristram-Nagle, S., & Nagle, J. F. (2004). Lipid bilayers: thermodynamics, structure, fluctuations, and interactions. *Chemistry and Physics of Lipids*, *127*(1), 3–14. https://doi.org/10.1016/j.chemphyslip.2003.09.002

Turlier, H., Audoly, B., Prost, J., & Joanny, J.-F. (2014). Furrow Constriction in Animal Cell Cytokinesis. *Biophysical Journal*, *106*(1), 114–123. https://doi.org/10.1016/j.bpj.2013.11.014

Turunen, O., Wahlström, T., & Vaheri, A. (1994). Ezrin has a COOH-terminal actin-binding

site that is conserved in the ezrin protein family. *Journal of Cell Biology*, *126*(6), 1445–1453. https://doi.org/10.1083/jcb.126.6.1445

Van Etten, R. A. (1994). The COOH terminus of the c-Abl tyrosine kinase contains distinct F- and G-actin binding domains with bundling activity [published erratum appears in J Cell Biol 1994 Mar;124(5):865]. *The Journal of Cell Biology*, *124*(3), 325–340. https://doi.org/10.1083/jcb.124.3.325

van Leen, E. V., di Pietro, F., & Bellaïche, Y. (2020). Oriented cell divisions in epithelia: from force generation to force anisotropy by tension, shape and vertices. *Current Opinion in Cell Biology*, *62*, 9–16. https://doi.org/10.1016/j.ceb.2019.07.013

Vardar, D., Chishti, A. H., Frank, B. S., Luna, E. J., Noegel, A. A., Oh, S. W., Schleicher, M., & McKnight, C. J. (2002). Villin-type headpiece domains show a wide range of F-actin-binding affinities. *Cell Motility and the Cytoskeleton*, *52*(1), 9–21. https://doi.org/10.1002/cm.10027

Vincent, J. (2012). Basic Elasticity and Viscoelasticity. In *Structural Biomaterials* (2nd ed., pp. 1–28). Princeton University Press. https://doi.org/10.2307/j.ctt7tbgv.4

Wagner, E., & Glotzer, M. (2016). Local RhoA activation induces cytokinetic furrows independent of spindle position and cell cycle stage. *Journal of Cell Biology*, *213*(6), 641–649. https://doi.org/10.1083/jcb.201603025

Welf, E. S., Miles, C. E., Huh, J., Driscoll, M. K., Isogai, T., Noh, J., Weems, A. D., Chi, J., Pohlkamp, T., Dean, K., Fiolka, R., Mogilner, A., & Danuser, G. (2019). A unified role for membrane-cortex detachment during cell protrusion initiation. *BioRxiv*, 696211. https://doi.org/10.1101/696211

Winder, S. J. (2005). Actin-binding proteins. *Journal of Cell Science*, *118*(4), 651–654. https://doi.org/10.1242/jcs.01670

Wray, J., Kalkan, T., Gomez-Lopez, S., Eckardt, D., Cook, A., Kemler, R., & Smith, A. (2011). Inhibition of glycogen synthase kinase-3 alleviates Tcf3 repression of the pluripotency network and increases embryonic stem cell resistance to differentiation. *Nature Cell Biology*, *13*(7), 838–845. https://doi.org/10.1038/ncb2267

Wu, H.-M., Lin, Y.-H., Yen, T.-C., & Hsieh, C.-L. (2016). Nanoscopic substructures of raft-mimetic liquid-ordered membrane domains revealed by high-speed single-particle

tracking. *Scientific Reports*, *6*(1), 20542. https://doi.org/10.1038/srep20542

Xia, S., Lim, Y. B., Zhang, Z., Wang, Y., Zhang, S., Lim, C. T., Yim, E. K. F., & Kanchanawong, P. (2019). Nanoscale Architecture of the Cortical Actin Cytoskeleton in Embryonic Stem Cells. *Cell Reports*, *28*(5), 1251-1267.e7. https://doi.org/10.1016/j.celrep.2019.06.089

Yasuda, S., Oceguera-Yanez, F., Kato, T., Okamoto, M., Yonemura, S., Terada, Y., Ishizaki, T., & Narumiya, S. (2004). Cdc42 and mDia3 regulate microtubule attachment to kinetochores. *Nature*, *428*(6984), 767–771. https://doi.org/10.1038/nature02452

Yeung, A., & Evans, E. (1989). Cortical shell-liquid core model for passive flow of liquid-like spherical cells into micropipets. *Biophysical Journal*, *56*(1), 139–149. https://doi.org/10.1016/S0006-3495(89)82659-1

Yeung, T., Gilbert, G. E., Shi, J., Silvius, J., Kapus, A., & Grinstein, S. (2008). Membrane Phosphatidylserine Regulates Surface Charge and Protein Localization. *Science*, *319*(5860), 210–213. https://doi.org/10.1126/science.1152066

Yonemura, S., Tsukita, S., & Tsukita, S. (1999). Direct Involvement of Ezrin/Radixin/Moesin (ERM)-binding Membrane Proteins in the Organization of Microvilli in Collaboration with Activated ERM Proteins. *Journal of Cell Biology*, *145*(7), 1497–1509. https://doi.org/10.1083/jcb.145.7.1497

Zhang, X., Flores, L. R., Keeling, M. C., Sliogeryte, K., & Gavara, N. (2020). Ezrin Phosphorylation at T567 Modulates Cell Migration, Mechanical Properties, and Cytoskeletal Organization. *International Journal of Molecular Sciences*, *21*(2), 435. https://doi.org/10.3390/ijms21020435

Zhu, L., Liu, Y., & Forte, J. G. (2005). Ezrin oligomers are the membrane-bound dormant form in gastric parietal cells. *American Journal of Physiology-Cell Physiology*, *288*(6), C1242–C1254. https://doi.org/10.1152/ajpcell.00521.2004

Zhu, M., & Zernicka-Goetz, M. (2020). Building an apical domain in the early mouse embryo: Lessons, challenges and perspectives. *Current Opinion in Cell Biology*, *62*, 144–149. https://doi.org/10.1016/j.ceb.2019.11.005

Zidovetzki, R., & Levitan, I. (2007). Use of cyclodextrins to manipulate plasma membrane cholesterol content: Evidence, misconceptions and control strategies. *Biochimica et Biophysica Acta (BBA) - Biomembranes*, *1768*(6), 1311–1324.

https://doi.org/10.1016/j.bbamem.2007.03.026